Practical dissolution dynamic nuclear polarization

Stuart Elliott, Quentin Stern, Morgan Ceillier, Théo El Daraï, Samuel Cousin, Olivier Cala, Sami Jannin

Practical Dissolution Dynamic Nuclear Polarization

Stuart J. Elliott[a], Quentin Stern[a], Morgan Ceillier[a], Théo El Daraï[a], Samuel F. Cousin[a], Olivier Cala[a] and Sami Jannin[a†]

Edited by Geoffrey Bodenhausen and Dominique Massiot

[a] Centre de Résonance Magnétique Nucléaire à Très Hauts Champs - FRE 2034 Université de Lyon / CNRS / Université Claude Bernard Lyon 1 / ENS de Lyon, 5 Rue de la Doua, 69100 Villeurbanne, France
[†] sami.jannin@univ-lyon1.fr

Glossary

NMR nuclear magnetic resonance
MRI magnetic resonance imaging
MAS magic angle spinning
OE Overhauser effect
CIDNP chemically induced dynamic nuclear polarization
*d*DNP dissolution dynamic nuclear polarization
*b*DNP bullet dynamic nuclear polarization
EPR electron paramagnetic resonance
ESR electron spin resonance
LODESR longitudinally detected electron spin resonance
FID free induction decay
SNR signal-to-noise ratio
CP cross-polarization
RF radiofrequency
AHP adiabatic half-passage
VNA vector network analyzer
P2P peak-to-peak
PA polarizing agent
BG background
TE thermal equilibrium
PTFE polytetrafluoroethylene
PEEK polyether ether ketone
HYPSO hybrid polarizing solids
HYPOP hyperpolarizing polymers
FLAP filterable labelled agents for polarization
CSA chemical shift anisotropy
SR2K scalar relaxation of the second kind
SPY spin polarimetry
ZULF zero- to ultra-low field
LAC level anti-crossing
UF ultrafast
HSQC heteronuclear single quantum coherence
HMQC heteronuclear multiple quantum coherence
HMBC heteronuclear multiple bond correlation
DOSY diffusion order spectroscopy
COSY correlation spectroscopy
SO-FAST-HMQC selective optimized flip-angle short-transient heteronuclear multiple quantum coherence

Abstract

This review article intends to provide insightful advice for dissolution-dynamic nuclear polarization in the form of a practical handbook. The goal is to aid research groups to effectively perform such experiments in their own laboratories. Previous review articles on this subject have covered a large number of useful topics including instrumentation, experimentation, theory, etc. The topics to be addressed here will include tips for sample preparation and for checking sample health; a checklist to correctly diagnose system faults and perform general maintenance; the necessary mechanical requirements regarding sample dissolution; and aids for accurate, fast and reliable polarization quantification. Herein, the challenges and limitations of each stage of a typical dissolution-dynamic nuclear polarization experiment are presented, with the focus being on how to quickly and simply overcome some of the limitations often encountered in the laboratory.

Keywords: NMR, Hyperpolarization, DNP, *d*DNP, CP, Sample Preparation, Systems Maintenance, Transport Dynamics, Polarization Quantification, SPY-NMR

1. Introduction

Ordinary signals in conventional nuclear magnetic resonance (NMR) and imaging (MRI) experiments are intrinsically weak. For a state-of-the-art radiofrequency (*rf*) NMR probe, the signal-to-noise ratios (SNRs) achievable are subject to factors such as *rf*-coil and preamplifier design, choice of pulse sequence, probe circuit, sample temperature and static magnetic field strength [1]. This is due to the relatively small Zeeman splitting between nuclear spin states (~2.7 $mJ.T^{-1}$ for a ^1H spin), even if the sample of interest is placed within the highest fields of today's superconducting NMR magnets, compared with the thermal energy available at room temperature (~2.4 $kJ.mol^{-1}$). This leads to a relatively flat Boltzmann distribution of nuclear spin populations, and consequently to a very low nuclear spin polarization. The polarization P_i of a nuclear spin-½ ensemble is defined as follows:

$$P_i = tanh\left(\frac{\hbar\gamma_i B_0}{2\kappa T}\right) \quad (1)$$

where γ_i is the magnetogyric ratio of spin *i*, B_0 is the static magnetic field and *T* is the spin temperature that is normally determined by the sample temperature. A typical polarization for a ^1H nucleus at 298 K and 6.7 T is on the order of $\sim 5.6 \cdot 10^{-5}$. This amounts to ~100'001 ^1H spins aligned with B_0 for every ~100'000 ^1H spins aligned against B_0. The inherent insensitivity is worse for NMR active nuclei with lower magnetogyric ratios. For many potential applications [2], nuclear spin polarizations close to unity are desirable.

From examining Equation 1, there are two key factors which control the level of nuclear polarization: (*i*) the magnetic field B_0; and (*ii*) the spin temperature *T*. Unfortunately, there are no commercial NMR magnets currently available with a sufficiently high magnetic field that would naturally hyperpolarize a nuclear spin ensemble. So-called "brute force" hyperpolarization techniques are available to significantly reduce the temperature of a sample inside an NMR magnet to the milliKelvin range by using a dilution refrigerator [3]–[6]. However, the method has many drawbacks: (*i*) cooling power limitations place constraints on usable sample volumes ($\lesssim$40 μL); (*ii*) the timescales of sample cooling are typically long (hours or days); and (*iii*) relaxation of nuclear spins at millikelvin temperatures is inherently slow due to a lack of molecular motions and, as a result, samples for brute force experiments typically require doping with paramagnetic agents to drastically shorten nuclear relaxation times**.** Consequently, other methods are required to bring the polarization of a nuclear spin ensemble closer to unity.

Dynamic nuclear polarization (DNP) is a hyperpolarization technique which has been around since the early 1950s [7] and aims to substantially boost the polarization level of nuclear spins. Since its conception the approach has seen dramatic developments and now the method is widely employed in both solid-state experiments, either under magic angle spinning (MAS) conditions at ca. 100 K[8] or static conditions at ca. $\leq$4.2 K[9].

The dissolution variant of the approach has also gained significant traction within the last two decades. J.-H. Ardenkjær-Larsen and co-workers first presented their results on dissolution-dynamic nuclear polarization (*d*DNP) in 2003 [9], and since then there has been vibrant activity within the community. *d*DNP methods often lead to liquid-state NMR signal enhancements approaching 10^4 [10], [11], with the increased sensitivity resulting in experiment times reduced by large factors. Further details regarding DNP mechanisms [7], [12]–[18] and applications of *d*DNP [19]–[32] are available. A two-magnet *d*DNP approach [33] and bullet-DNP (*b*DNP) [34] have additionally been shown to generate impressive NMR signal enhancements but will not be discussed herein.

A number of key requirements are generally necessary in order to perform *d*DNP measurements:

(i) A homogeneous freezing of the sample of interest in a glassy DNP matrix [35];

(ii) An optimal concentration of paramagnetic radical species uniformly distributed throughout the sample [36];

(iii) Low temperatures -- often provided by a cryogenic reservoir of liquid helium with 1.2 K < *T* < 4.2 K;

(iv) A magnetic field -- the majority of *d*DNP experiments are conducted in the range 3.35 T < B_0 < 10.0 T [37]–[39];

(v) A source of microwaves with capabilities for frequency adjustment or modulation [40];

(vi) Dissolution and transfer to facilitate liquid-state NMR or MRI applications.

The sample of interest is typically dissolved in a mixture of protonated and deuterated aqueous solvents, commonly H_2O or D_2O combined with glycerol or DMSO, homogeneously mixed with paramagnetic radical agents, *e.g.,* TEMPOL, trityl etc. The sample is transferred to a holder and inserted into a *polarizer* at sufficiently high field, the sample space of which is flooded with liquid helium ensuring that the sample solution forms a glass upon freezing. The microwaves irradiate the sample at a specific frequency close to the electron spin resonance. This process transfers the near unity electron polarization directly to the nuclei of interest or indirectly via nearby nuclei of differing isotopic type. After sufficient nuclear spin polarization has been obtained, *e.g.* $P(^{13}C)$>30%, the frozen media is flushed out of the sample space using a jet of hot solvent, *e.g.,* D_2O, and transferred to separate NMR magnet for detection.

The field of *d*DNP has made a number of advances due to improved sample formulation [41]. The need for a glassy DNP solvent matrix comes from the desire to homogenously freeze the sample medium in the superfluid helium bath. However, the presence of electron-bearing species can also significantly attenuate the lifetime of nuclear polarization in the solid-state. To avoid this effect, a range of silica and polymer materials have been developed to ensure a distance between the paramagnetic centres and the nuclei to be polarized [41]–[44]. Such materials are compatible with a wide range of compounds [45], and allow for the removal of glass-forming materials within the sample.

The performance of NMR experiments conducted under *d*DNP conditions relies on the precise implementation of each of the key components listed above. An important question to answer is: What experimental conditions are required? *d*DNP experiments are typically performed between 3.35-7.05 T and 1.2-4.2 K. The reasons for this choice are motivated by the high polarization of electron spins at liquid helium temperatures.

Paramagnetic sources, *i.e.,* unpaired electrons, are fundamentally required for DNP [46]. The electrons form dipolar coupled spin systems with the nuclei of interest. At low temperature, the electron species are highly polarized, *i.e.,* P_e = 99.93% at 1.2 K and 7.05 T, whilst the nuclear spins lack a

significant degree of polarization. This is due to the large magnetogyric ratio γ_e of the electron compared with those of nuclei, *e.g.,* $\gamma_e/\gamma_H \simeq 660$ where γ_H is the proton magnetogyric ratio. The application of microwave irradiation at a frequency which is slightly off-resonance with respect to the electron transition frequency leads to a transfer of polarization to the nuclear spins via mutual flip-flop interactions.

At this point the spin system is no longer in equilibrium, and relaxation processes drive the population distribution back towards its initial state. This process mainly occurs via electron relaxation, which is a significantly faster phenomenon at low temperature than nuclear spin relaxation. The electron relaxation time T_{1e} is on the order of ~30-100 ms at liquid helium temperature for radical species such as TEMPOL [23], [47] but can be significantly longer in other cases, *e.g.,* for trityl radicals.[36] It is therefore important to saturate the electron spin transitions, the extent of which is controlled by whether the EPR line is homogeneously or heterogeneously broadened, spectral diffusion and radical concentration, to force the electron spins to find new dipolar coupling partners that can again participate in the DNP process. For *d*DNP systems, microwave powers on the order of 30-120 mW are required [48]. The ability to modulate both the frequency and bandwidth of the microwave source can significantly boost polarizations and build-up times whilst reducing the concentration of free radicals required [40].

The rate of the different DNP processes, *i.e.,* the build-up of the DNP signal, the electron relaxation, etc., are dependent on the concentration of electron centers embedded within the glassy matrix. A compromise of 10-50 mM radical concentration is often used in experiments. This quantity of radical sources ensures that DNP build-up times τ_{DNP} are reasonable, on the order of minutes, and that a satisfactory level of nuclear spin polarization can be achieved, *e.g., P*(^{1}H)≃30% at 3.8 K. in the case of nitroxide radicals. Moreover, after dissolution, the radical concentration can have a major influence on the nuclear T_1 in regions of low magnetic fields [49]–[51].

Dissolving frozen samples at liquid helium temperatures provides the greatest possible signal enhancements for solution-state NMR experiments. At these temperatures, it is possible to rapidly dissolve the frozen samples by directing a blast of superheated solvent into the sample space [2], [9]. Furthermore, the time taken to dissolve the sample of interest is typically much shorter than the longitudinal nuclear relaxation time T_1. More details regarding the energy transfer and the thermodynamics of sample dissolution can be found elsewhere. [2]

The capabilities of *polarizer*s to perform more traditional NMR experiments under *d*DNP conditions has been drastically improved by the implementation of cross-polarization (CP) [52], [53]–[56]. This method has allowed significant levels of ^{13}C (60%) and ^{15}N (25%) polarization to be achieved in a few tens of minutes [57]. The high levels of nuclear polarization allow for additional applications to be developed, such as structural elucidation at natural abundance [58].

Figure 1 depicts a flow diagram of a typical *d*DNP experiment. The flow diagram consists of three loops. These loops are related to the following experimental steps: (*i*) sample preparation and verification of sample properties; (*ii*) preparing the components of the *d*DNP system and performing standard experiments; and (*iii*) enacting a dissolution experiment with subsequent analysis of the NMR data. Each step should be successfully completed before moving onto the next, *e.g.,* the fact that without a glassy environment, the sample of interest will not polarize sufficiently for subsequent experiments clearly demonstrates this principle (see Section 2.3 for details). Furthermore, if unexpected levels of polarization are achieved later on in the experiment, this could be attributed to the fact that the sample properties, *e.g.,* its radical concentration, were not verified beforehand using EPR. The flow diagram is therefore designed to ensure that the experiment is completed to a high standard.

In this review, we aim to share our knowledge regarding how to best combat partial shortcomings of a complete *d*DNP experiment. We have targeted the following key subjects: sample preparation and health; *d*DNP and CP procedures; mechanical aspects and spin dynamics of sample dissolution and transfer; and quantification of the ^{1}H and ^{13}C polarization. The various aspects of this review are broken down further in Table 1. Herein, we present hands-on information with a focus on experimental formulas, recipes and hardware innovations that will help other *d*DNP groups around the world better perform their own experiments. We also present potential limitations of *d*DNP experiments and common reasons for failure. Photographs will be given in order to shine more light on the tips and tricks necessary to effectively perform optimal *d*DNP experiments. Theoretical underpinnings will also be provided where necessary.

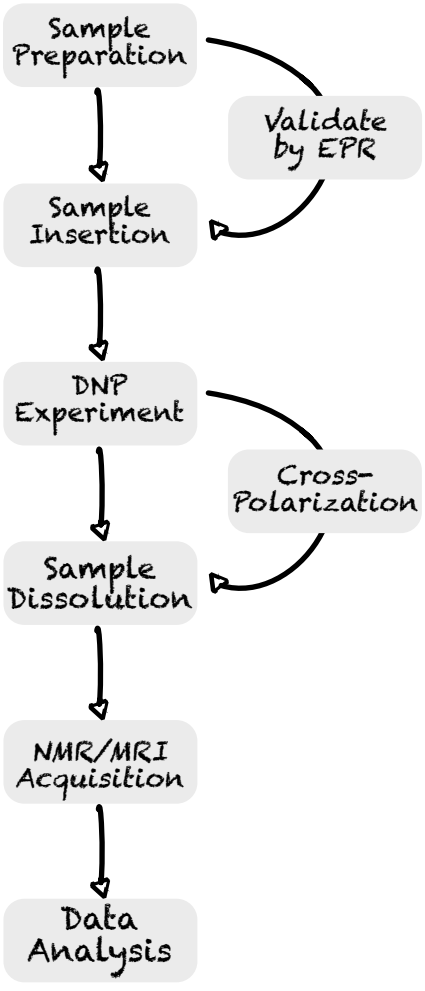

Figure 1: Complete flow diagram to be used during a typical *d*DNP experiment in our laboratory. "Validate by EPR" and "Cross-Polarization" are optional steps.

Table 1: Summary of topics discussed in this work.

Section	Topic	Sub-Topics
2.	Sample preparation	Concentration of PAs Glass formation Preparing a standard *d*DNP sample Alternative samples
3.	Sample health	PA choice Chemical conservation Nitroxide stability Nitroxide degradation EPR quantification
4.	Systems health	RF-probe construction Sensitivity estimates Tuning and matching Nutation curves Directional coupler usage Oscilloscope protection RF-probe arcing RF-pulse reflection RF-coil maintenance
5.	*d*DNP experiments	DNP build-up experiments Microwave optimization Effect of PA concentration Effect of temperature Effect of magnetic field ^{13}C Optimization Multiple-CP Thermal equilibrium
6.	Dissolution mechanics	Dissolution strategy Dissolution preparation Shimming procedure Dissolution stick Fluid path Energy required for dissolution Optimizing dissolution efficiency Transfer and injection Gas-driven systems Liquid-driven systems Bubble contamination Sample contamination Avoiding low-field
7.	Dissolution physics	Relaxation theory generalities Solid-state relaxation Liquid-state relaxation Coherent polarization loss
8.	Hyperpolarized liquid-state NMR	Detection parameters Polarization quantification

2. Sample preparation for *d*DNP

2.1. Introduction

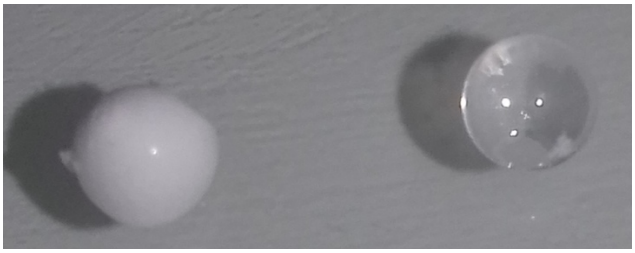

Figure 2: Picture of 10 uL drops of a sample frozen in liquid nitrogen, forming a homogeneous transparent glassy bead with 60% glycerol - 40% H_2O (right) or a milky microcrystalline bead with 40% glycerol – 60 % H_2O (left).

The motivation for this section is to give the basic requirements and suitable protocols for conventional sample preparation in *d*DNP experiments. We will explain the main requirements for *d*DNP samples to be optimally polarizable and give a step-by-step procedure to properly prepare, store and freeze the samples.

The main desired goal of *d*DNP sample preparation is to allow maximum polarizability of the molecule(s) of interest. The two most important features that enable a good sample polarizability are: (*i*) an adequate polarizing agent concentration (typically 10-50 mM); and (*ii*) an intimate mixing of the molecules of interest and the polarizing agents. This intimate mixing needs to be established at the sample preparation stage and should remain upon freezing, *i.e.,* one should favour glassy state and avoid aggregates or microcrystals (see Figure 2). For this reason, in addition to water, co-solvents are often used which improve the probability of freezing the sample into a glassy state. The sample preparation protocol needs to be reproducible across laboratories, and we therefore provide a protocol that has proven to be reproducible in our laboratory. Finally, sample storage requires special attention as the paramagnetism of the polarizing agent may decrease with time.

2.2. Polarizing agents at the right concentration

Doping the *d*DNP sample with an adequate radical concentration is of utmost importance. However, very few studies report a thorough optimization of this parameter. The concentration usually lies between 10 and 50 mM, and the data available in the literature suggest that DNP performance is rather flat and robust within a certain range. For example, the radical 4-hydroxy-2,2,6,6-tetramethylpiperidin-1-oxyl, also known as TEMPOL, can be used for DNP at 9.4 T and 1.5 K, as presented in Figure 2.2 [59]. The DNP enhancements were measured for concentrations ranging from 25 to 100 mM. In all cases, the same mixture of H_2O/D_2O/glycerol-d_8 (1/3/6 *v*/*v*/*v*) was used. The optimal TEMPOL concentration is around 80 mM, somehow higher than the optima usually found at 6.7 T (50 mM) and 3.35 T (30 mM). Other concentration optimization studies are reported at other magnetic fields and in other sample formulations [42] [60].

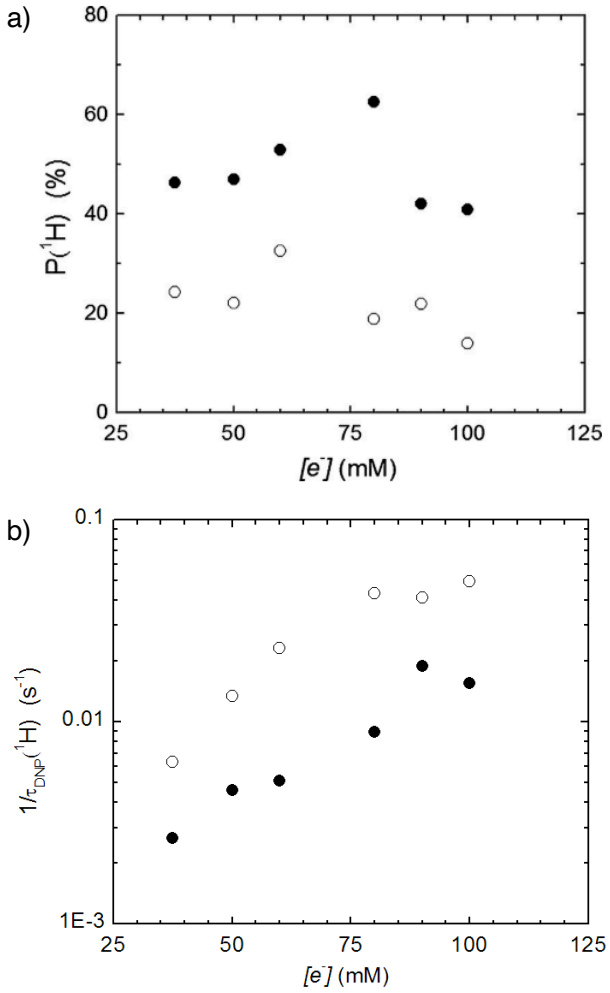

Figure 3: a) Proton polarization $P(^1H)$ and b) DNP build-up rates $1/\tau_{DNP}$ as a function of TEMPOL concentration in H_2O/D_2O/glycerol-d_8 (1/3/6 *v*/*v*/*v*) at 9.4T and 4.2 K (open circles) or 1.5 K (filled circles). Adapted with permission from [59]**.**

2.3. The requirement to form a glass

The second criteria is that a glass should be formed upon freezing [35], [61]–[67]. Vitrification is necessary for a homogeneous distribution of radicals and substrates which enables efficient DNP and nuclear spin diffusion resulting in a spatially uniform nuclear spin polarization across the sample.

For frozen solutions, two solid forms can be found: glassy and crystalline (and also mixtures thereof) [68]. Crystal formation will introduce heterogeneity into the system by rejecting other molecules (radicals) at the crystal interface [69]. Such heterogeneity often leads to low DNP performance with some areas saturated with radicals and other areas free from radicals. This leads to stretched exponential build-up curves, rather that mono-exponential build-up curves, that have longer build-up time constants τ_{DNP} and with lower levels of final polarization (see Figure 4).

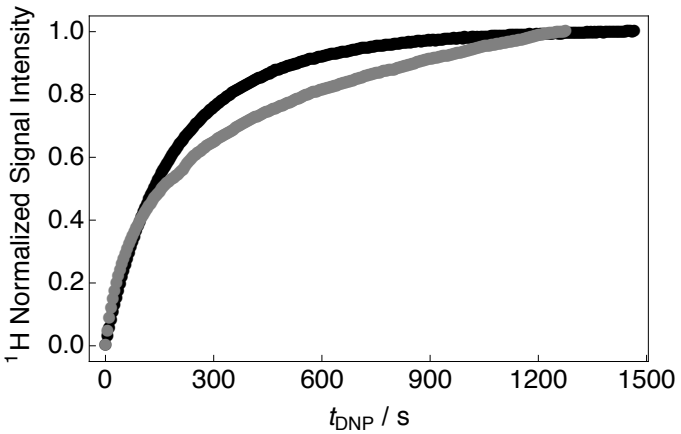

Figure 4: Example of ^{1}H DNP build-up curves measured at 7.05 T and 1.2 K for a glassy (black) and non-glassy (grey) sample.

To avoid water crystallization, glass-forming agents are usually employed, such as glycerol (50-60%$_w$) or DMSO (<77%$_w$) [35]. Transitions from glassy states to crystalline states can occur even below the freezing temperature of the solution, by a mechanism called "cold crystallization" [70]. It is therefore important to store samples at sufficiently low temperatures before using them in order to avoid unexpected phenomena such as radical quenching or sample degradation. It was recently observed that spontaneous nanoscopic phase separation can occur in water/glycerol solutions although they appear macroscopically homogeneous [71], leading to reductions in polarization efficiency by up to 20%.

In order to check the sample health visually, 10 µl droplets of the solution can be dropped into liquid nitrogen. The resulting frozen beads should remain translucent, which is evidence of their glassy state, while partial crystallization leads to opaque beads (see Figure 2). The sample can then be transferred as is to the DNP polarizer at 4.2 K. During this process, if the water/glycerol ratio is not well respected, or if other glass-forming agents are used, the beads can become opaque. Figure 2 presents two frozen beads with the transparent one (right) considered as glassy and a milky opaque one (left) as micro-crystalline. Transparency in its own is not a strict warranty of non-crystallisation but rather an indication that the maximum size of the crystallites or domains are small compared to wavelength of visible light.

2.4. Preparation of a standard dDNP sample

2.4.1. General information

Here we describe the procedure for preparing a "standard" sample for DNP. Having a standard DNP sample is important in the context of *d*DNP in order to make sure that the DNP polarizer is performing well before switching to new sample formulations. We consider the example of a sample composed of 3 M [1-^{13}C] sodium acetate dissolved in H_2O/D_2O/glycerol-d_8 (1/3/6 *v*/*v*/*v*) containing 50 mM TEMPOL. This is used by several groups as a reference sample. The storage of each compound and the preparation of the sample is important to get the best and most reproducible DNP performance. For example, when radicals are stored at room temperature, the concentration of the paramagnetic radical species can decrease over time; or if the glass-forming agent, glycerol in our case, is not meticulously mixed, the process of vitrification does not take place as expected, reducing overall DNP performances. Taking that into account, we now present two ways of preparing a standard sample for *d*DNP. The first one allows one to prepare 10 aliquots of 100 µL to be then frozen and stored at -80°C for later or immediate use. The second for preparing each compound separately in advance and storing at -80°C to be in a position to rapidly prepare fresh new samples when required.

2.4.2. Preparation of a standard sample for frozen storage

Preparation of a 1 mL sample aliquoted into 100 µL batches and frozen. In a **graduated glass cylinder** weight precisely 249 mg of [1-^{13}C] sodium acetate, for a 3 M final concentration. Note that after adding 1 mL of solvent, the total volume occupied by the solvent and the 249 mg of [1-^{13}C] sodium acetate is approximately 1.2 mL. This has to be taken into account for calculating the final concentrations. Separately, weight in a microtube (**microtube A**) 8.6 mg of TEMPOL, to have a 50 mM final concentration. In a second microtube (**microtube B**), mix H_2O/D_2O/glycerol-d_8 (1/3/6 *v*/*v*/*w*), 100 µL of milli-Q water, 300 µL of D_2O (99.9%) and 822.6 mg of glycerol-d_8 (density: 1.371 gmL^{-1}). Dissolve the TEMPOL of **microtube A with 6 µL of D_2O** (the limit of the solubility in D_2O is 1670 gL^{-1}). Add 800 µL of **tube A** to the **graduated glass cylinder**. Sufficiently vortex and then sonicate for ~10 mins in a sonicator bath at 30°C. Repeat the last step until all is dissolved. Add the content of **microtube A** to the graduated glass cylinder. Adjust the volume with **microtube B** to 1 mL. Split the sample into 100 µl aliquots in separately labelled tubes. Store in a freezer at - 80 °C.

2.4.3. Preparation of the constituents of the standard sample for later rapid preparation

In 10 microtubes, weigh 25 mg of sodium acetate. Prepare 100 µL of 400 mM TEMPOL in D_2O (68.8 mg) and split into 8 microtubes (12.5 µL volume). Prepare 10 tubes with 68 mg glycerol-d_8 (~54 µL). Freeze all the microtubes (with clear labels!) in a -80°C freezer. To prepare a fresh sample: take 1 microtube of sodium acetate (a), 1 tube of TEMPOL (b), 1 microtube of glycerol-d_8 (c) and let them melt at room temperature. Mix (a) and (b) with 10 µL of milli-Q water, 12 µL D_2O and (c). Sufficiently vortex and then sonicate for ~10 mins in a sonicator bath at 30°C. Once the sample is ready to analyze, pipette 100 µL into a home-built sample holder and centrifuge for 4 seconds at 1000 rev/min on a benchtop centrifuge. Insert the sample carefully into the polarizer to avoid the formation of bubbles.

2.5. Alternative samples

Samples of interest can be loaded directly in porous DNP matrices with free radicals located on the surface of the pores or in the bulk of the matrix. In this case, there is a balance between advantages: no glass-forming agent is necessary, samples can be extracted from matrices reducing paramagnetic relaxation and molecules of interest can thus be separated from free radicals which could generally interact together in a conventional sample formulation [31]. There are also disadvantages: chemical synthesis could alter radicals, an optimal filtration system is needed, and overall performances are intimately related to the material properties: pore size, radical distribution and concentration. Some examples of such polarizing matrices are reported in the literature and are based on polymers or silica materials [42], [44], [72]–[77]. Nitroxides

can also be covalently attached to sepharose beads or on thermoresponsive gels. The porous thermoresponsive thermoplastic hydrogel, which can be dispersed as a powder in the sample, precipitates during the dissolution process [41], [43]. In these cases, the sample under investigation is dissolved in the appropriate solvent without cryo-protectant and the matrix powder is impregnated directly before loading into the polarizer. These polarizing media can be synthetized through published protocols, or provided upon reasonable request by our group concerning HYPSO or HYPOP materials.

As mentioned above, the choice of solvent and freezing technique is crucial in order to form a glass and have a homogeneous distribution of radicals and substrates to enable efficient spin diffusion and homogeneous polarization throughout the sample. However, it is sometimes difficult to freeze an aqueous solution quickly enough to form a glass using liquid nitrogen. An alternative method of sample preparation which removes the need for glass-forming agent is possible by increasing the freezing speed. It is well known that liquid alkanes have appreciably better heat transfer efficiencies than liquid nitrogen [78]–[80]. For instance, liquid ethane, propane and 2-methyl butane (isopentane) are all superior freezing agents for the vitrification of aqueous solutions.

3. *d*DNP sample health

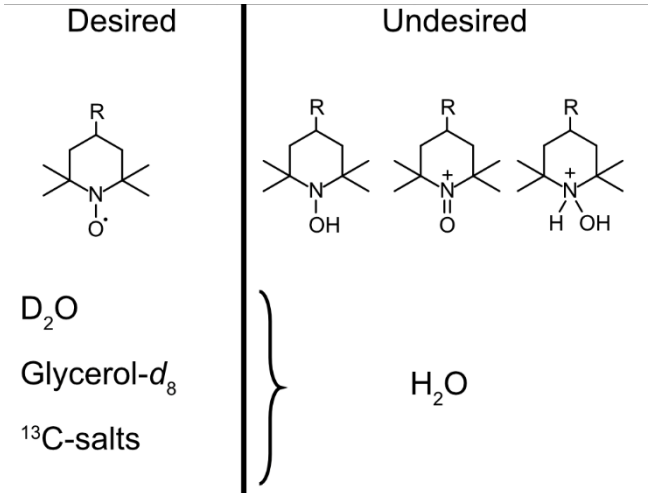

Figure 5: Different derivatives of nitroxide derivatives that may co-exist in a DNP sample.

3.1. Introduction

The motivation for this section is to draw attention to important issues related to *d*DNP sample health that can be encountered, and to detail clear procedures to allow the user to assess the health of a *d*DNP sample.

Evaluating the *d*DNP sample health before performing dissolution experiments is highly desired in order to avoid unnecessary loss of time and resources working on unhealthy samples that may not give rise to expected DNP performances. Poor sample health systematically leads to slower polarization build-up times and lower overall polarizations. The two most common health issues for a *d*DNP sample are: (*i*) a PA concentration below its expected value; and (*ii*) an inadequate PA distribution (see Figure 4). Problems concerning these two sample requirements can arise even though great care has been given to the sample preparation. The next sections regarding the *d*DNP sample health will discuss the following important aspects in detail:

PA stability. The stability of the PA is a critical parameter, which depends on its chemical state and environment. The first goal of this section is not to review the stability properties of all PAs used in *d*DNP, but only for the nitroxide class of radicals. Their stability depends on different environments that are typically encountered. Indeed, the PA is usually provided in the form of a pure powder, and then dissolved in water, possibly together with a glass-forming agent such as glycerol, and finally together with the molecules of interest. The second goal of this section is to provide guidelines for PA and *d*DNP sample storage that guarantees the best PA stability and therefore most efficient and reproducible *d*DNP experiments.

PA concentration and relaxation. Poor handling of PAs often leads to a lower electron spin concentration in the final *d*DNP sample, which ultimately leads to reduced DNP performances (for short build-up times). Given the relatively long build-up times of typical DNP-compatible sample formulations, it is of interest to assess the sample health before polarizing the sample. This can in principle be done in a qualitative manner by simply measuring the nuclear spin-lattice relaxation towards thermal equilibrium right after insertion into the *polarizer*, *i.e.,* without microwave irradiation and therefore without DNP, at 4.2 K (even before cooling the cryostat to its lowest temperature). As shown in Figure 3, a lower active PA concentration tends to slow down the nuclear spin-lattice relaxation. Estimating this relaxation rate in about 5 minutes provides a way of qualitatively estimating the active PA concentration.

Radical quantification. Several methods exists to quantify radicals: gas and liquid chromatography [81][82], potentiometric analyses [83] and electron paramagnetic resonance (EPR) [84]. This last technique has the advantage, in our field, of also providing information about the EPR line, which can have a tremendous impact on DNP performance, mechanisms, etc. We will describe here a basic protocol for PA quantification in both liquid- and solid-state at room temperature using a benchtop X-band continuous wave EPR spectrometer. We will describe the calibration and data analysis in order to avoid as much as possible the classical pitfalls of quantitative EPR.

3.2. PA choice

Several different radicals have been used in *d*DNP, such as trityl [79] and BDPA [80], which are both aromatic radicals, nitroxides [85] and Galvinoxyl [86]. The choice of the radical depends on the target nuclear spin and the polarization strategy. For instance, trityl and BDPA have sharp EPR lines and achieve good performances for direct ^{13}C polarization while nitroxides have much broader EPR spectra and have better performances for proton and fluorine polarization. For our *d*DNP experiments, we use mainly nitroxide-based samples, and we therefore describe here how to avoid their degradation and how to handle them properly.

3.3. Conservation of chemicals

As mentioned previously, standard samples are made of four classes of molecules: (*i*) radicals (polarizing agents); (*ii*) H_2O (or D_2O); (*iii*) glass-forming agents (glycerol, DMSO); and (*iv*) a target molecule (often ^{13}C enriched) [9], [87], [88]. To perfectly control the composition of the sample which will be used in DNP experiments, good sample component storage is often the first requirement. D_2O, glycerol, nitroxides and ^{13}C enriched target molecules should be stored at low temperature (~5°C) but should be carefully warmed up before use in order to avoid moisture which may contaminate these samples. The storage conditions can be more or less strict depending on the molecule: pyruvic acid which can degrade easily over time should be stored at -20°C whereas acetate can be stored at ~5°C for instance. However, under such conditions, it is perfectly possible to observe a decrease in the radical purity over a few months, which can be a major threat in the case that one does not have a means to quantify it. Both DNP performance and reproducibility may be greatly impacted.

3.4. Nitroxide stability

"Stable" radicals are subjected to various threats depending on their chemistry (see Figure 5). For example, dimerization may be a non-negligible quenching mechanism of triarylmethyl (trityl) radicals while alpha-saturated nitroxides are not impacted by this mechanism under normal conditions [89], [90]. We will focus, in our case, on nitroxide stability by highlighting decomposition mechanisms that should be avoided. Based on a previous review of the subject [91], we show the Pourbaix

diagram of the most common nitroxides, *e.g.*, TEMPO, including the redox equation of oxygen/water (see Figure 6).

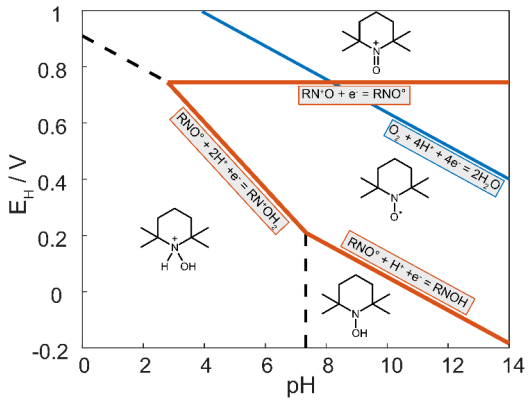

Figure 6: Pourbaix diagram of TEMPO. Adapted with permission from [91].

The greatest threat of nitroxide stability, under standard conditions of temperature and pressure, are acids (see Figure 7). Indeed, nitroxides are always in equilibrium with the associated nitrosonium ion (RN^+O) and the hydroxylamine (RNOH or RN^+OH^2).

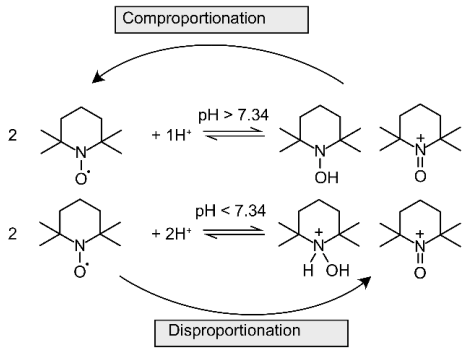

Figure 7: Disproportionation and comproportionation of TEMPO.

This equilibrium between the radical and two other compounds is mainly ruled by the ability of the media to provide Brønsted acidity. A major advantage of this radical is its stability under basic conditions, which can also be a method to regenerate the radical. A simple way to see this clearly consists of plotting the Frost diagram of TEMPO (see Figure 8) as a function of pH. This diagram shows the free energy of each molecule as a function of their degree of oxidation, and as such lower free energies correspond to more stable states. At pH 10 and higher, nitroxide redox potentials are below those of the other two compounds. Such patterns indicate that the comproportionation mechanism is the leading reaction and the disproportionation can be considered as inactive.

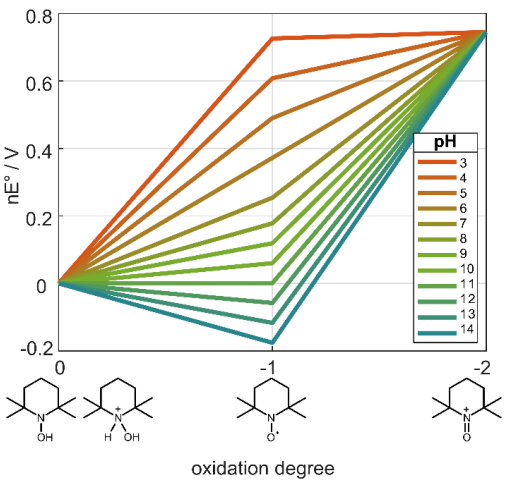

Figure 8: Frost diagram of TEMPO. Hydroxylamine is considered as the reference with a neutral degree of oxidation.

Furthermore, we can anticipate the opposite phenomenon for pH < 3, where the potential of nitroxides should become sufficiently high so that comproportionation need not be considered further. But in the pH interval ~3-11 both mechanisms co-exist and we need to consider kinetics to estimate the equilibrium of the system [91].

Another aspect that can be mentioned is the role of oxygen. It is a potential oxidant of radicals and may react differently depending on the type of radical. In our case, we will consider its role on the redox equilibrium of TEMPO. In Figure 9a, we plotted the apparent voltage potential of each reducer/oxidizer couple in two pH intervals (between 8.2 and 14 as well as between 4 and 8.1). We also consider the main reactions that should occur (see Figure 9b and 9c). For pH > 8.2, we can see that oxygen has a protective role as a weak oxidizer and so can only react with the RNOH form, which is favorable to the formation of nitroxides, already in good shape due to the comproportionation. However, for pH < 8.1, oxygen starts being the strongest oxidizer and can start reacting with TEMPO to form nitrosonium ions. Still, these reactions are not a major threat as long as pH > 8 but needs to be considered for lower pH.

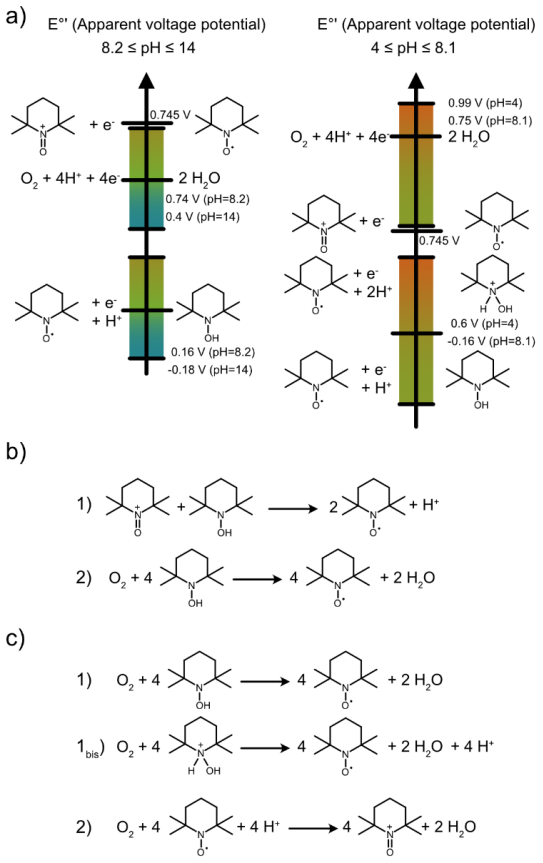

Figure 9: Redox half-equations involved in the degradation of TEMPOL, including oxygen. a) Evolution of apparent voltage potentials for pH ϵ [8.2 14] and pH ϵ [4 8.1]. b) Main reactions involved for 8.2 < pH < 14. c) Main reactions involved for 4 < pH < 8.1.

3.5. Degradation of nitroxides during storage

As discussed previously, nitroxide stability can be impacted by two major mechanisms during storage. Disproportionation generates both nitrosonium ion and hydroxylamine in the same amount. This phenomenon is mainly impacted by water, moisture or more generally the presence of protic solvents. Temperature and pH impact the thermodynamic equilibrium. Oxygen oxidation can also occur in solution, mainly by avoiding the formation of the hydroxylamine at high pH but can also impact nitroxides at pH < 8. Unlike the disproportionation, this reaction is asymmetric. Note that ascorbic acid, if used as a reducing agent, will have an effect opposite to oxygen. To illustrate the main phenomena involved we performed several tests on a 1.5-year-old batch of TEMPOL stored in our fridge (4°C). We weighted 3 samples for different purposes (see Figure 10a):

- The first sample (17.4 mg) was dissolved in 1 mL of THF, and then 100 µL of the mixture was analyzed by quantitative EPR to determine the concentration of radicals, and ultimately the "survival rate" of TEMPOL in the powder.
- The second sample (22.2 mg) was dissolved in 500 µL of a 10:1$_v$ THF/water solution. The mixture was diluted by a factor 5 in THF before EPR quantification on a 100 µL volume of the final solution. A nano-drop UV-vis analysis was performed on a droplet of this solution.
- The third sample (22.6 mg) was dissolved in 500 µL of a 10:1$_v$ THF/water solution previously saturated with NaOH. The mixture was diluted by a factor 5 in THF before EPR quantification on a 100 µL volume of the final solution. A nano-drop UV-vis analysis was performed on a droplet of this solution.

EPR experiments were performed on a continuous-wave X band EMXnano apparatus from *Bruker Biospin* using 3 mm outer (OD) diameter quartz tubes provided by *Wilmad*. Data processing, including baseline corrections, were performed with the software of the spectrometer (*Xenon*). For experimental details, see next section. UV visible experiments were performed on a NanoDrop 1000 from Thermoscientific.

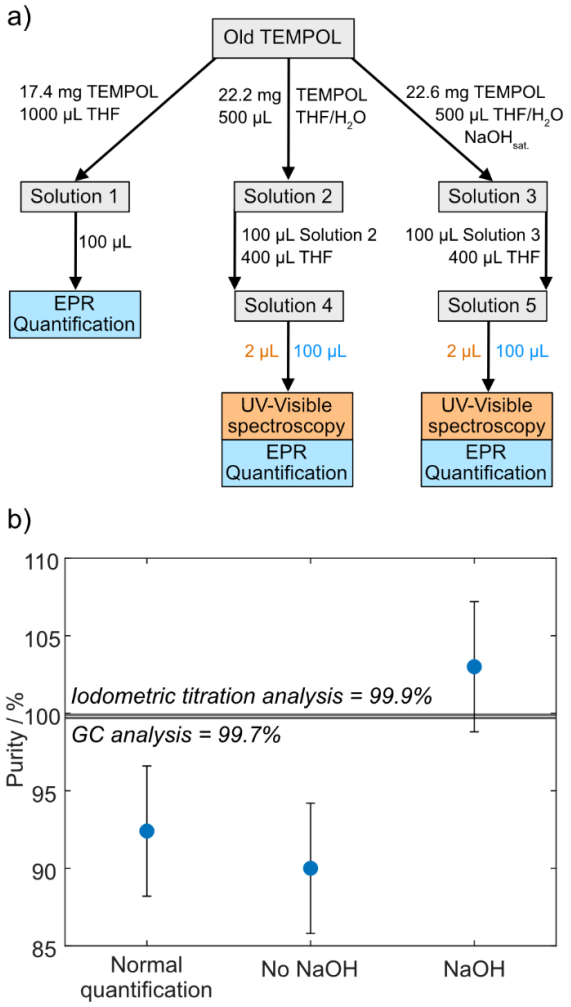

Figure 10: a) Sample preparation procedure. b) Percentage or "survival fraction" of TEMPOL radical used for each sample. Results from the original certificate of analysis are indicated as horizontal lines.

EPR spectra show a significant degradation of this batch of TEMPOL (see Figure 6.b). However, we can observe a fast restoration of the TEMPOL radical in basic media. Such a fast mechanism, without bubbling oxygen, suggests that disproportionation occurred during the storage, meaning that the comproportionation can occur quickly under basic conditions without any stoichiometric issue. Such degradation could be explained by the presence of moisture due to the hygroscopicity of TEMPOL, which can be further increased by a bad handling, *e.g.,* the product may still have been cold when opened. This degradation over time can become very important depending on how often the batch is handled and how. We already observed in our laboratory some TEMPOL survival fractions dropping below 70% over a few months, which can lead to significant detrimental effects on DNP performances.

To avoid such issues several simple rules can be applied:

- Buy small batches.
- Warm up carefully before each use.
- The hygroscopy of nitroxides being quite different (TEMPO < TEMPOL < amino TEMPO), use preferentially the less hygroscopic one.
- In solution, keep the media as basic as possible to be safe (pH > 10 being a very safe zone).
- Quantify radical purity by EPR if possible.

3.6. EPR quantification

Quantitative CW-EPR provides a way (not necessarily the easiest) to quantify radical concentrations [84]. For example, GC and iodometric titration are preferred by *TCI* to determine the purity of TEMPOL, whereas *Sigma Aldrich* uses infrared coupled to elementary analysis for TEMPOL or Thin layer chromatography for amino TEMPO. Furthermore, EPR spectrometers less frequently available compared to chromatography devices for example. EPR quantification is difficult and suffers from high uncertainties (*ca*. 5%). Despite this, EPR is a unique method which focuses on electronic spins and can provide a lot of relevant information in addition to the concentration of the radicals (EPR lineshape, radical dispersion, and presence of paramagnetic impurities, to name a few). Radical powders, *e.g.* TEMPO, are bought from *Sigma Aldrich* and used immediately when a calibration is required in our laboratory.

Liquid calibration. Standard solutions are prepared by mixing known amounts of TEMPO powder in a given volume of THF. Analyses can be performed in a 3 mm OD quartz tube from *Wilmad* with a 100 µL sample volume of the described solutions (2 cm sample height in each tube).

Solid calibration. Standards are prepared by mixing known amounts of TEMPO powder with KBr. Analyses are performed in a 4 mm OD quartz tube from *Wilmad* (2 cm sample height in each tube).

The EPR spectra are integrated before a baseline correction is performed (see Figure 11). Baseline corrections are performed using polynomials. EPR spectra are then integrated a second time. The resulting integrals are normalized using the following formula [84]:

$$I_{corrected} = \frac{\iint_{325}^{355} S(B_0)\mathrm{d}B_0}{Q_{factor} \times B \times \sqrt{P} \times NS \times 10^{\frac{20}{RG}} \times T_c} \quad (2)$$

with:

- Q_{factor} Quality factor of the cavity used under our experimental conditions;
- B_0 Magnetic field (mT);
- B Field modulation (Gauss);
- P Microwave power (mW);
- T_c Conversion time (ms);
- NS Number of scans;
- RG Receiver gain (dB).

NS and *RG* are both taken directly into account by the software. All spectra were obtained at room temperature.

$I_{corrected}$ values can be plotted as a function of the radical concentration within the sample to obtain a calibration curve. However, such a calibration curve obtained with a benchtop X-band EPR spectrometer Bruker EMX nano (see Figure 11) will only be reliable if the samples are analyzed at the same temperature and with identical sample volumes.

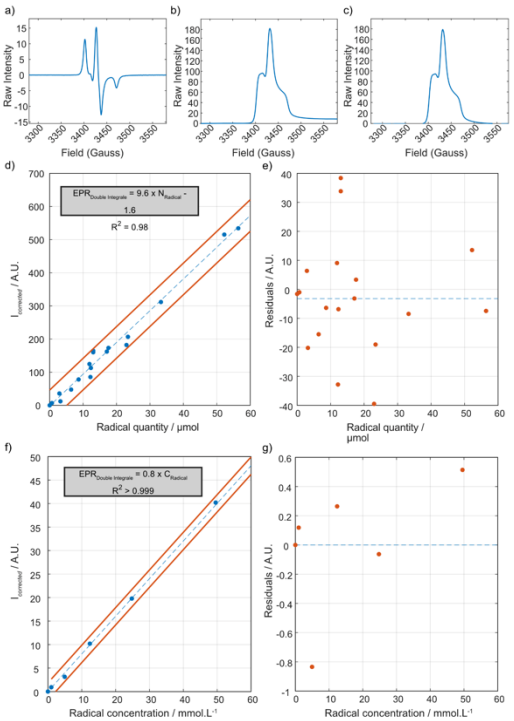

Figure 11: a) Raw CW-EPR spectrum. b) Integrated EPR spectrum. c) Baseline corrected EPR spectrum. d) Solid-state calibration curve. e) Residuals of the solid-state calibration. f) Liquid-state calibration curve. g) Residuals of the liquid-state calibration.

4. Characterization of microwave and radiofrequency systems

4.1. Introduction

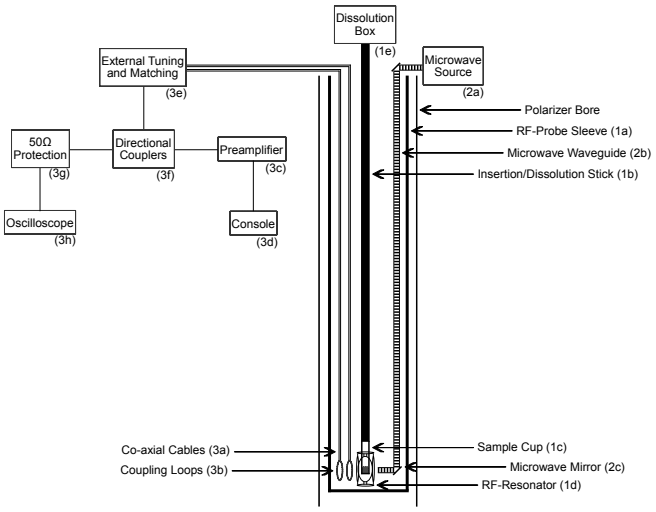

Figure 12: Schematic overview of a *d*DNP *rf*-probe in the bore of a *polarizer*, including connections to essential apparatus: dissolution box (1e), microwave source (2a), oscilloscope (3d) and various *rf*-elements (3a-h). The sleeve of the *rf*-probe (1a) can accommodate the dissolution stick (1b), the microwave waveguide (2b) and co-axial cables (3a). The cavity contains the sample cup (1c), *rf*-resonator structure (1d) and coupling loops (3b).

The motivation for this section is to describe the major components of a *d*DNP *rf*-probe and its accessories. We will explain the main characteristics of each element and provide a step-by-step procedure to correctly configure a *d*DNP *rf*-probe for optimal usage. These checks ensure that the *d*DNP *rf*-probe is in good condition before, during and after experiments.

The main function of a *d*DNP *rf*-probe is to provide an optimal environment to polarize a *d*DNP-compatible sample via a beam of microwave irradiation. The ability to measure NMR signals during the course of a *d*DNP experiment, with the objective of assessing the rate at which the polarization of the sample builds up, is greatly desired. Such a detection is possible with the *HyperSense* or *SPINLab polarizer*s [92]. However, to be able to accurately quantify nuclear spin polarization and observe thermal equilibrium NMR signals without DNP in a sensitive, stable and quantitative manner requires more sophisticated instrumentation, such as the polarizer developed by *Bruker Biospin*. In a more advanced version presented here, the *d*DNP *rf*-probe can additionally feature cross-polarization (CP) capabilities, typically from sensitive ^{1}H spins to rare ^{13}C spins, to boost both ^{13}C polarization levels and build-up rates [23]. After sufficient levels of nuclear polarization have been achieved, the *d*DNP *rf*-probe must also provide a pathway to rapidly eject the sample from a frozen state with a jet of superheated solvent. The *d*DNP *rf*-probe also houses other elements essential to the successful usage of *d*DNP instrumentation (see Figure 12).

The next sections regarding the *d*DNP *rf*-probe will discuss the following important aspects in detail (Figure 12 components given in brackets):

Probe construction. The components of the *rf*-probehead are housed inside a non-magnetic sleeve (1a) usually made of brass or copper to ensure good thermal contact with the liquid helium cryogen. The *rf*-probe positions the *rf*-coil structure inside the bore of the *polarizer* at the magnetic sweet spot. Through the centre of the *rf*-probe is a tube which acts as a guide for an insertion stick (1b) to position the sample cup (1c) at the location of the *rf*-resonator (1d). The geometry of the sample cup has to be optimized to maximize the *rf*-coil filling factor. The sample cavity needs to be used as a fluid path when the hyperpolarized sample is rapidly melted with a high temperature solvent and flushed out of the *polarizer* using pressurized helium gas. A dissolution stick (1b) and box (1e) are generally used for this process [9]. The brass material of the *rf*-probe framework, including cavity and microwave mirrors (2c), is suitable for use in cryogenic fluids, since it has good thermal conductivity, an extremely low thermal coefficient of expansion and is non-magnetic even upon machining [8], [93]. Stainless steel is used for parts that connect low and high temperature environments, since this material does not transport heat efficiently. The design permits a good flow of liquid helium towards the sample for efficient cooling, ultimately allowing an improved *d*DNP performance. Rubber o-rings are additionally used to make sure the *rf*-probe is secured tightly to both the bore of the polarizer and the sample insertion stick, which prevents the suction of air into the *rf*-probe and the consequential build-up of ice inside the cryostat when the *d*DNP system is being pumped.

Microwave source. A stringent requirement of all *d*DNP mechanisms is that the microwaves (2a) must irradiate the sample off-resonance, *i.e.,* there must be a slight mismatch between the frequency of the microwave field and the electron transition frequencies. Coherent microwave irradiation is not strictly necessary, and as such oversized waveguides (2b) can be employed to minimize power losses during microwave delivery. Furthermore, the microwave waveguide material, commonly stainless steel, should possess suitable thermal properties to reduce heat losses from the superfluid liquid helium bath. The microwave waveguide will also typically contain a set of carefully positioned mirrors (2c), which directs the microwave beam down the *rf*-probe and allows it to shine onto the sample. If the microwave source can deliver a power in the order of a few tens of milliwatts by the time the beam reaches the sample, then a portion of the EPR line will become sufficiently saturated. For the best possible experimental results, it is imperative that the following steps are ensured: (*i*) the microwaves can be activated/deactivated/gated; and (*ii*) the positive and negative microwave irradiation frequencies, including associated frequency and bandwidth modulations, can be optimized.

NMR system. The *rf*-probe is comprised of a stainless-steel frame which securely holds co-axial cables (3a) in place, allowing *rf*-waves to travel to and from a number of coupling loops (3b) *via* a preamplifier (3c) to the NMR console (3d). The choice of a poor thermally conductive stainless-steel material limits heat transfer from the room temperature *rf*-connections to the cryogenically cooled *rf*-probehead. Most *d*DNP *rf*-probes are only capable of single *rf*-channel irradiation, and as such the *rf*-probe is usually implemented to monitor only the build-up of ^{13}C polarization as a function of the microwave irradiation time [94]–[97]. The *rf*-probe requires tuning to the correct *rf*-frequencies and signal matching can be improved by sensible coupling coil design; particularly in the case of low-γ nuclei. Tuning the *rf*-channel frequency can be performed when the *rf*-probe is inside (using external tuning and matching devices (3e)) or outside (replacing circuit capacitors) of the *polarizer* [98], [99]. The *rf*-coil must produce a suitably homogeneous and stable B_1-field at high *rf*-pulse powers. Materials such as copper, silver and gold exhibit good cryogenic properties under

*d*DNP conditions [100] and are used in the coupling loops (3b) of the *d*DNP *rf*-probe. The favourable electrical conductivity is required to produce a strong B_1-field to excite nuclear spins, and subsequently amplify and detect the signal response with sufficient SNR. This further improves the tuning and matching capabilities of the *rf*-coil insert.

More functional *d*DNP *rf*-probes may contain 2 (or more) *rf*-channels, which allow for $^{1}H \rightarrow ^{13}C/^{15}N$ nuclear polarization transfer *rf*-pulse schemes, such as CP. The quality and filling factors of the *rf*-probe will substantially impact the ability to perform 90° *rf*-pulses at desired powers, which can be characterized by nutation experiments. Implementation of the CP approach requires excitation of the entire NMR lineshape for each *rf*-frequency (which can be challenging for high frequency spins) and the application of high-power double *rf*-irradiation. At high *rf*-powers, arcing can be frequently engendered in the superfluid helium bath which is deleterious to the transfer of nuclear polarization. Furthermore, cross-talk between *rf*-channels and *rf*-pulse reflections are also common in home-built *d*DNP *rf*-probes. It is possible to use a directional coupler (3f) to syphon a small quantity of power away from the transmitted and reflected *rf*-waves and send these signals to an oscilloscope (3h) protected by a 50 Ω resistance (3g). With such an architecture in place the above topics can be experimentally investigated, identified and characterized in the context of the *rf*-probe.

In the following sections, we will discuss the main points that ensure microwave source and *rf*-probe condition.

4.2. Probe construction

Figure 13: Photograph of the perpendicular coupling coils used for inductive detection attached to co-axial transmission cables. The ^{1}H channel uses a single loop, whilst the ^{13}C channel employs three tightly wound loops of smaller diameter. This structure is housed within a brass "cap" whilst in liquid helium. The choice of a cylindrical *rf*-coil support is necessary to accommodate the sample dissolution stick and to fit into the bore of the polarizer. The two *rf*-coil loops are elliptical loops of 12×16 mm in diameter.

The design of a *d*DNP probehead has to fulfil a number of constraints: (*i*) present a suitable space in which to perform adequate *d*DNP on a sample of interest; (*ii*) allow a beam of microwave irradiation to shine upon the sample; and (*iii*) monitor NMR signals throughout a *d*DNP experiment. Such requirements are met by the design shown in Figure 13, which shows a common arrangement of the microwave delivery conduit and the coupling loops used for inductive detection (Figure 12, 3b). Several geometries have been proposed for CP-*d*DNP [9], [101] and herein we describe a probe setup with two geometrically decoupled channels [52].

The coupling loops are required to induce and detect the response of the nuclear spins within a *d*DNP sample. The design of the radiofrequency field coils depends on the information sought by the user. The design additionally allows detection of thermal equilibrium NMR signals without hyperpolarization, *i.e.,* in the case where the SNR is low, and as a result; accurately quantify levels of nuclear spin polarization in a repeatable manner.

When constructing the coupling loops, as a rule of thumb, more sensitive nuclei require fewer turns, and the diameter of the loop can be larger. The converse is true for less sensitive nuclei. This will ensure a capacity for improved matching of the low-γ nucleus. The two coupling loops are made from silver-coated copper wire (95% Ag/5% Cu, OD = 1 mm) and should be perpendicular to each other. The coupling loops are connected to co-axial cables (Figure 12, 3a), which are soldered to the (electrical) ground-plate of the probe for structural rigidity. The co-axial cables are chosen to have the following special properties: (*i*) A stainless-steel outside to ensure a low thermal conductivity; and (*ii*) A copper beryllium central wire to ensure good electrical conductivity with a low thermal conductivity. The co-axial cables provide a way of shielding *rf*-irradiation during its journey to and from the NMR console (Figure 12, 3d) via a circuit containing preamplifiers (Figure 12, 3c).

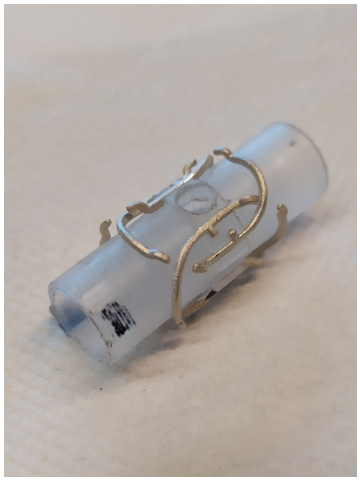

Figure 14: Photograph of an *rf*-coil structure used for *d*DNP experiments, including: a plastic (KelF) support, copper coils and spacings for ceramic capacitors (not shown).

A typical *rf*-coil assembly is depicted in Figure 14. There are two parallel *rf*-coils on the opposing faces of the *rf*-coil insert (^{1}H and ^{13}C in the case of Figure 14). The *rf*-coil insert has been designed such that: (*i*) the *d*DNP sample cup (Figure 12, 1c) can fit into the resonator structure (Figure 12, 1d) with a maximized filling factor; and (*ii*) a brass cap can fit onto the *rf*-probehead without disturbing the central components. One downside of such an insert is the use of plastic (KelF) material, which although chosen to minimize the background ^{1}H NMR signal, nevertheless contains a non-negligible quantity of ^{1}H spins. This can be avoided by using a "background-free" *rf*-coil structure [102].

The majority of commercial *d*DNP *rf*-probes are configured for single *rf*-channel irradiation, and the nucleus of study is often chosen to be ^{13}C. In this case, the *rf*-probe is designed to monitor the ^{13}C polarization build-up curve before dissolution.

The beneficial choice of a design with two coupling loops is the detection of NMR signals from different isotopes. Polarization transfer methodologies such CP allow low-γ nuclei to be polarized and detected in significantly shorter time periods by transferring polarization from sensitive nuclear spins, *e.g.,* ^{1}H. The freedom granted by this design allows for a number of opportunities for method development [103].

4.3. Sensitivity estimates

As discussed above, *d*DNP experiments are routinely conducted at temperatures of 1.2 K < T < 4.2 K and static magnetic field strengths in the range of 3.35 T < B_0 < 10.0 T. Under such conditions, we need to be able to provide an order of magnitude calculation regarding the sensitivity of a *d*DNP *rf*-probe per millimole. For a ^{1}H NMR spectrum acquired with 16 transients and a 0.1° *rf*-pulse angle, a typical proton SNR for a 100 μL sample of 3 M [1-^{13}C] sodium acetate in DNP juice™ at thermal equilibrium at 3.8 K and 7.05 T is ~155 (see Figure 15).

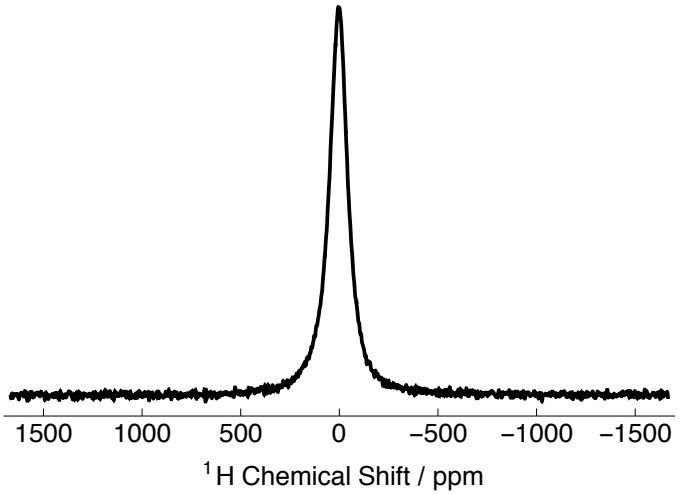

Figure 15: Relevant portion of the experimental ^{1}H NMR spectrum of a 100 μL sample volume of 3 M [1-^{13}C] sodium acetate dissolved in H_2O/D_2O/glycerol-d_8 (1/3/6 *v*/*v*/*v*) and doped with 50 mM TEMPOL without hyperpolarization at a temperature of 3.8 K. The spectrum was acquired at 7.05 T (^{1}H nuclear Larmor frequency = 300.13 MHz) and 3.8 K with 16 transients (*rf*-pulse angle = 0.1°).

The concentration of polarizing agents is neglected in subsequent calculations for the sake of simplicity. Corrections are required in order to appropriately normalize the SNR for the number of transients and *rf*-pulse angle implemented to acquire the desired NMR spectrum. The correction factor is ~143 for the number of scans and *rf*-pulse angle given above (compared with a single transient and a 90° *rf*-pulse angle). A *d*DNP sample of this type will have a ~18.6 M ^{1}H sample concentration, and consequently the sensitivity per millimole is ~$1.2\cdot10^{4}$ mmol^{-1}. A similar calculation for ^{13}C nuclei yields a sensitivity per millimole of ~$1.1\cdot10^{2}$ mmol^{-1}. The low temperature of the superfluid liquid helium bath is largely responsible for the relatively good sensitivity of a typical *d*DNP *rf*-probe, since this aspect alone increases the thermal polarization by a factor of ~78.5, and likely outweighs the influence of the poor *rf*-coil filling factor, the excitation bandwidth and other deleterious aspects. Other reasons for the increase in sensitivity at liquid helium temperatures are: (*i*) a reduction in thermal noise; and (*ii*) an increase in Q-factor. It is worth noting that good performances are obtained despite ^{1}H and ^{13}C linewidths on the order of *ca*. 10-30 kHz for typical *d*DNP-compatible sample formations.

15. NMR system

4.4.1. Tuning and matching

In order for the *rf*-coil structure (Figure 12, 1d) to resonate at the desired nuclear transition frequencies for the chosen nuclei and magnetic field, the *rf*-probe requires tuning to the correct frequency. This will maximize the NMR signal obtainable from an experiment. This is typically done by inserting capacitors into the circuitry. The value of the capacitances used for each *rf*-coil determines the frequency at which the *rf*-coils can absorb and re-emit *rf*-irradiation. The value of the capacitances should obey the laws of basic circuit theory:

$$\omega_0 = \frac{1}{\sqrt{LC}} \quad (3)$$

where ω_0 is the resonant frequency of the *rf*-coil, L is the inductance of the circuitry and C is the total capacitance of the *rf*-coil.

The *rf*-coil frequencies are measured by placing the ^{1}H-^{13}C *rf*-coil into the probehead of the dedicated *d*DNP probe. It is of paramount importance that the *rf*-coil structure is correctly aligned with the intended coupling loops, since the orientation of the *rf*-coils with respect to the coupling loops will alter the tuning and matching properties of the *rf*-probe. Alignment aids are suggested to help the reader to achieve this. Tuning the *rf*-coil to the correct coil frequency is an iterative process, which is impacted by the temperature of the *rf*-coil and of external tuning and matching devices (Figure 12, 3e), as shown in Table 2.

Table 2: Typical *rf*-coil frequencies and quality (Q) factors (at -3 dB) as a function of the *rf*-coil surrounding temperature and use of external tuning and matching devices. ℓN_2 = liquid nitrogen, ℓHe = liquid helium. T&M = external tuning and matching device used. * = Desired tuning frequency at B_0 = 7.05 T.

	^{1}H		^{13}C	
Conditions	ω_0 / MHz	Q-Factor at -3 dB	ω_0 / MHz	Q-Factor at -3 dB
No Cap	289.84	59	70.81	42
Cap	295.07	62	72.86	40
Cap + ℓN_2	298.21	155	73.69	73
Cap + ℓHe	299.20	201	73.90	97
Cap + ℓHe + T&M	300.14*	251	75.47*	113

It can clearly be seen, when stepwise adding the brass cap, cooling the *rf*-coils and using external tuning and matching devices (Figure 12, 3e), that the correct *rf*-probe frequency can be obtained for both *rf*-channels. It is worth noting, at least in the case of the ^{1}H *rf*-channel, that the initial *rf*-coil frequency is >10 MHz lower in frequency than the target *rf*-channel frequency. The case is less extreme for the ^{13}C *rf*-channel. This demonstrates the strong influence of temperature etc. on the *rf*-probe frequencies. Depending on the available capacitors, it may be the case that the value of each capacitor has a certain tolerance. This suggests that *rf*-probe tuning is in fact an art which cannot be predicted. It is therefore best practice to target the desired nuclear transition frequency once inside the superfluid liquid helium bath of the *polarizer*, *i.e.,* aim for the closest initial resonant frequencies in the absence of external

tuning and matching equipment, and subsequently use the external tuning and matching devices to finely optimize the desired frequency thereafter (Figure 12, 3e). Finally, the *Q*-factors for each *rf*-channel are not as high as for a typical liquid-state NMR probe. However, the lower *Q*-factors are sometimes useful for suppressing the effects of radiation damping [104], especially for protons.

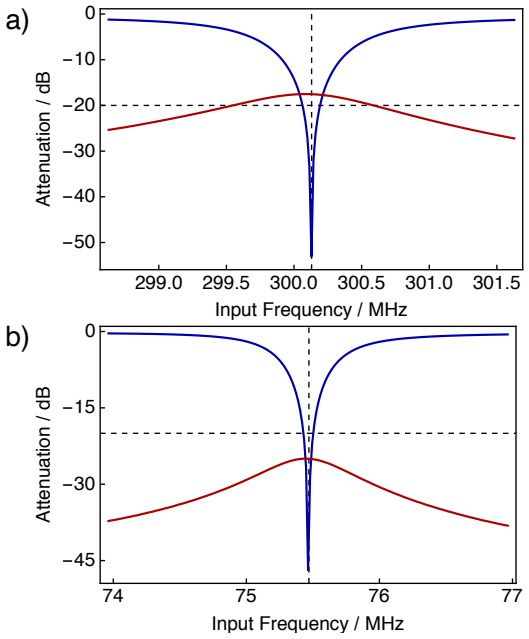

Figure 16: Vector network analyser (VNA) attenuation traces of reflectance (dark blue curves) and transmittance (dark red curves) in units of dB acquired for the a) ^{1}H and b) ^{13}C *rf*-channels of a *d*DNP *rf*-coil insert as a function of input frequency in units of MHz. The horizontal dashed lined marks -20 dB, and the vertical dashed line indicates the nuclear Larmor frequency for the nucleus of interest at cryogenic temperatures (~1.2 K) and 7.05 T (^{1}H nuclear Larmor frequency = 300.13 MHz, ^{13}C nuclear Larmor frequency = 75.47 MHz).

The use of external tuning and matching devices (Figure 12, 3e) at room temperature achieves both of the desired resonant frequencies, with good matching, as shown by the ^{1}H and ^{13}C vector network analyser (VNA) attenuation traces in Figures 16a and 16b, respectively. The dark blue curves show the reflectance of each *rf*-coil, whilst the dark red curves show the transmittance of the *rf*-coils. Greater signal matching can also be achieved by improved coupling coil design, which is particularly useful in the case of low-γ nuclei.

The *rf*-coil has its own self-resonance, as stated above. The addition of co-axial *rf*-cables to the *rf*-probe does not change the self-resonance of the *rf*-coil. However, these co-axial cables, which are used to connect the *rf*-probe to the preamplifier of the spectrometer, and also incorporate external tuning and matching devices into the *rf*-circuit, induce spurious self-resonances involving a combination of the co-axial *rf*-cable, *rf*-coupling loop and the external tuning and matching devices. These resonances contribute an insignificant B_1-field at the position of the sample. The lengths of the co-axial *rf*-cables must be chosen as to set the spurious cable resonances as far away as possible (in frequency) from the self-resonance of the *rf*-coil. However, moving the *rf*-cable resonances slightly closer to the *rf*-coil self-resonance can be used to shift the frequency of the true *rf*-coil resonance, which is coupled to the *rf*-coil loop, co-axial *rf*-cables and tuning and matching system.

An ideal *rf*-coil would have a transmittance, *i.e.,* the transmitted power from one *rf*-channel to the other, lower than -20 dB. In the case of the ^{1}H *rf*-channel, the transmittance is clearly above -20 dB, indicating that there is likely cross-talk from the ^{13}C *rf*-channel to the ^{1}H *rf*-channel, see Section 4.4.6. However, the fact that the transmittance is well below -20 dB for the ^{13}C VNA trace indicates that the ^{1}H *rf*-channel does not interact strongly with the ^{13}C *rf*-channel. Clearly, there are no visible effects of cable resonances in the vicinity of the desired *rf*-coil frequency.

4.4.2. Nutation frequency curves

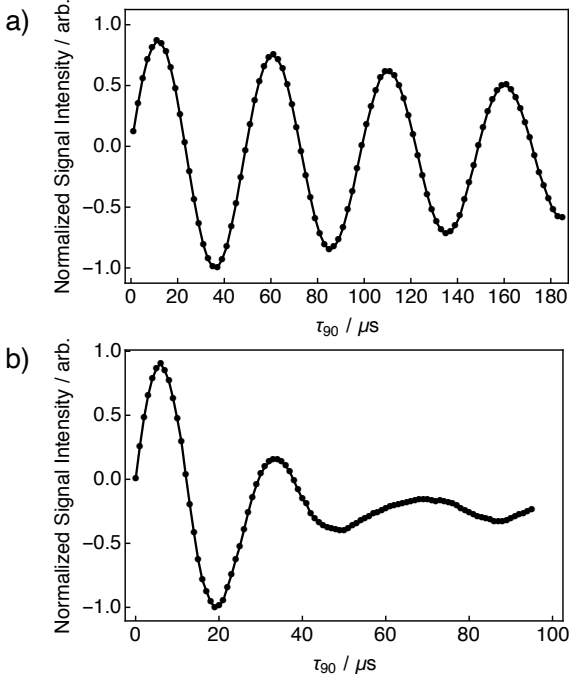

Figure 17: Nutation frequency curves for the a) ^{13}C and b) ^{1}H *rf*-channels of a *rf*-coil insert using a sample of 3 M [1-^{13}C] sodium acetate dissolved in H_2O/D_2O/glycerol-d_8 (1/3/6 *v*/*v*/*v*) and doped with 50 mM TEMPOL acquired at liquid helium temperatures (~1.2 K) and 7.05 T (^{1}H nuclear Larmor frequency = 300.13 MHz, ^{13}C nuclear Larmor frequency = 75.47 MHz).

The choice of materials such as copper, silver and gold for the coupling loops (Figure 12, 3f) of the *d*DNP *rf*-probe allows the production of a strong, stable and homogeneous B_1-field to maximize the SNR of a *d*DNP experiment. Furthermore, the filling- and *Q*-factors of the *rf*-probe significantly influence the 90° *rf*-pulse characteristics, *e.g.,* their duration for a given power. Such effects are investigated by nutation frequency curve experiments.

Figure 17a shows a ^{13}C nutation frequency curve for a sample of 3 M [1-^{13}C] sodium acetate dissolved in H_2O/D_2O/glycerol-d_8 (1/3/6 *v*/*v*/*v*) and doped with 50 mM TEMPOL acquired using the ^{13}C *rf*-channel of a *rf*-coil insert (Figure 12, 1d). The duration of the ^{13}C 90° *rf*-pulse was determined to be $\tau_{90}^{C} = 10.9$ μs at 150 W ^{13}C *rf*-pulse power and a liquid helium temperature of ~1.2 K, which implies a ^{13}C *rf*-pulse bandwidth of 22.94 kHz under the same conditions. This gives an *rf*-probe efficiency of $B_1/\sqrt{W} \simeq 1.87$ kHzW$^{-1/2}$, where B_1 is the *rf*-field amplitude and W is the power of the *rf*-pulse. This is sufficient to cover the frequency range of the ^{13}C NMR lineshape for this sample under *d*DNP conditions (ca. ~30 kHz linewidth at FWHM). The effects of auto-refocussing are clearly observable at 270°, the NMR signal being more intense than for 90°. The ratio of the NMR signal intensities at the 90°

and 810° data points is ~0.71, which indicates a good *rf*-homogeneity of the ^{13}C *rf*-channel of the *rf*-coil insert.

Implementation of CP methods requires sufficient excitation of the whole NMR line for both *rf*-frequencies. This is often difficult for high frequency spins, since high-power *rf*-irradiation is typically required, which can engender deleterious *rf*-probe arcing in the superfluid helium bath, see Section 4.4.5.

Figure 17b shows a ^{1}H nutation frequency curve for a sample of **I** acquired using the ^{1}H *rf*-channel of a *rf*-coil insert. The duration of the ^{1}H 90° *rf*-pulse was determined to be τ_{90}^{H} = 5.6 μs at 60 W ^{1}H *rf*-pulse power and a temperature of ~1.2 K, which implies a ^{1}H *rf*-pulse bandwidth of 44.64 kHz under the same conditions. This gives an *rf*-probe efficiency of $B_1/\sqrt{W} \simeq 5.76$. This may be insufficient to cover the very broad ^{1}H NMR resonance in the case of high proton concentrations (ca. ~100 kHz linewidth at FWHM), in which case more sophisticated techniques can be employed [105]. Given the profile of the ^{1}H nutation frequency curve in Figure 17b, measured on a frozen *d*DNP sample, it may be the case that the bandwidth of the ^{1}H *rf*-pulse is insufficient to homogeneously excite the entire ^{1}H NMR resonance for long *rf*-pulse durations (>10 μs), when this phenomenon becomes more prominent. The ^{1}H nutation frequency curve would likely look much better in a liquid-state NMR sample. The inhomogeneity of the *rf*-pulses produced may contribute to the signal decay shown in Figure 17b. The effects of auto-refocussing are again observable at 270°. In this case, however, the ratio of the NMR signal intensities at the 90° and 810° data points could not be obtained.

4.4.3. Directional coupler usage

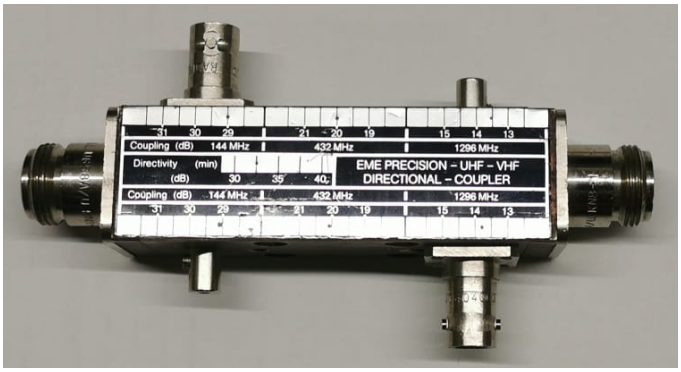

Figure 18: Directional couplers used to investigate *rf* transmission and reflection. Blue = connection to monitor ^{1}H *rf*-pulse reflection. Red = connection to monitor ^{1}H *rf*-pulse transmission.

Figure 18 shows a photograph of a commonly used directional coupler (Figure 12, 3f) attached to the ^{1}H *rf*-channel of the preamplifier in our laboratory (Figure 12, 3c). Underneath, a second directional coupler can be seen connected to the ^{13}C *rf*-channel of our preamplifier. The directional couplers are used to investigate the *rf* transmission and *rf*-pulse reflection. In the current configuration (blue shading), the directional coupler takes only a small fraction (-35.2 dB) of the *rf*-power and directs it to an oscilloscope (Figure 12, 3h). In this way, the reflection from both *rf*-channels can be observed. If the alternative configuration is used (red shading), the transmission of the *rf*-pulses of both *rf*-channels of the preamplifier can be investigated.

4.4.4. Oscilloscope protection

Figure 19: Photograph of 50 Ω resistors (grey shading) used to protect the oscilloscope whilst performing *rf*-coil cross-talk characterizations.

To avoid damage to the oscilloscope (Figure 12, 3h) whilst investigating *rf*-coil reflections and arcing, protection of the oscilloscope is required (Figure 12, 3g). 50 Ω resistors must be attached to the *rf*-channels of the oscilloscope at all times, as indicated by the grey shading in Figure 19. The additional resistance due to these connections must be corrected for in the calculations, see Section 3.5. The 50 Ω resistor allows the oscilloscope to handle a ~5 W maximum power. Furthermore, the impedance of the oscilloscope is set to 1 MΩ and the 50 Ω resistor is in parallel so that the *rf*-power is absorbed by the resistor rather than by the oscilloscope. Such a preventive measure substantially reduces the chance of potential damage to the oscilloscope in cases where the *rf*-power exceeds the oscilloscope specifications. In reality, what is actually measured is the voltage generated across the resistor.

4.4.5. RF-probe arcing

Figure 20a shows an oscilloscope plot of ^{1}H (blue curve) and ^{13}C (red curve) spin-locking *rf*-pulses implemented for a typical cross-polarization (CP) contact, see Section 5.6, using a ^{1}H-^{13}C *rf*-coil insert (Figure 12, 1d) displayed in units of V (voltage) as a function of the CP contact duration (ms). Throughout the entire 7 ms CP contact time, the amplitude of the *rf*-pulses remains stable. This provides a good indication that there is no *rf*-probe arcing during the *rf*-pulses.

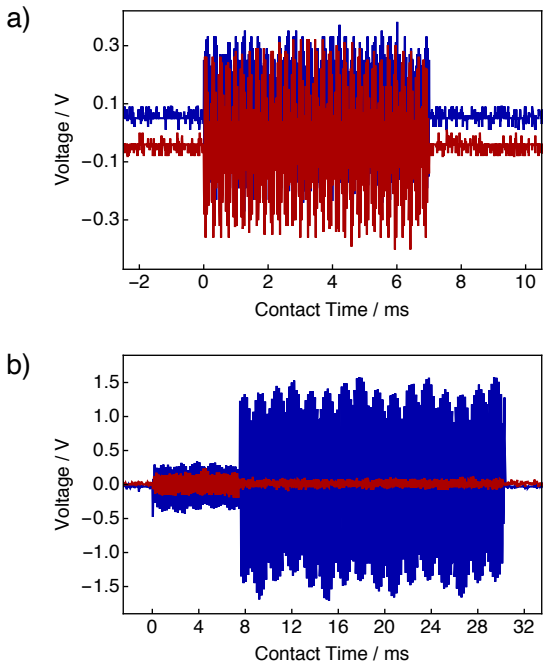

Figure 20: Oscilloscope voltage traces of square *rf*-pulses emitted by a *rf*-coil insert for a) 7 ms and b) 30 ms for ^{1}H (dark blue curve) and ^{13}C (dark red curve) cross-polarization (CP) contact after 3 s of ^{1}H DNP acquired at ~1.2 K and 7.05 T (^{1}H nuclear Larmor frequency = 300.13 MHz, ^{13}C nuclear Larmor frequency = 75.47 MHz). For details of the CP *rf*-pulse sequence, see Section 5.6.

The oscilloscope plot displayed in Figure 20b provides an example of *rf*-probe arcing during the simultaneously applied ^{1}H and ^{13}C *rf*-fields during the CP contact. The arcing limit was reached at ~1.2 K using *rf*-pulse powers of 120 W (^{1}H) and 300 W (^{13}C), and a CP contact duration of 30 ms. The arcing event commences ~8 ms into the CP contact, at which point there is a significant jump in the ^{1}H *rf*-pulse voltage (blue trace). The ^{13}C *rf*-pulse power (red trace) decreases slightly at the beginning of the arcing event. Arcing subsequently continues through the remaining duration of the CP contact *rf*-pulses. After arcing it is important to replenish liquid helium into the *rf*-probe space, since this will prevent further arcing in following experiments.

4.4.6. RF-coil reflection

Below we provide an example of how to quantify *rf*-pulse reflection between the *rf*-channels of the *d*DNP probe: Consider an *rf*-pulse of power P_{trans}, which is transmitted through a directional coupler (see Figure 12, 3f) with a given attenuation. The transmitted *rf*-pulse generates a reflection with a peak-to-peak (p2p) voltage of V_{ref}^{p2p}. The reflected p2p voltage can be readout directly using an oscilloscope (Figure 12, 3h). The power of the reflected *rf*-pulse P_{ref} is determined by employing the following equation:

$$P_{ref} = \left(\frac{V_{ref}^{p2p}}{2\sqrt{2}}\right)^2 \cdot \frac{1}{R} \quad (4)$$

where R is the circuit resistance. The attenuation factor A_{dB}, which is a result of transmitting the *rf*-pulse through a directional coupler, is given by the logarithm of the ratio of the square of the reflected V_{ref} and transmitted V_{trans} voltages, proportional to the power levels of the *rf*-pulses by the circuit current, according to the following equation:

$$A_{\mathrm{dB}} = 10\, Log\left\{\left(\frac{V_{ref}}{V_{trans}}\right)^2\right\} \quad (5)$$

By using Equation 4, and often assuming a resistance R = 50 Ω, see Section 4.4.4, we can estimate the power of the reflected *rf*-pulse P_{ref}. Typical *rf*-pulse reflections have powers which are on the order of ~5-10% of the value of P_{trans}. The same protocol can be used for any *rf*-pulse. Ideally, the best way to effectively tune and match an *rf*-probe would be to directly minimize the reflected power of the *rf*-pulses.

4.4.7. RF-probe maintenance

If a probe breaks, a sudden shift in the NMR tuning frequency for one of the *rf*-coil channels will be observed. This can also be detected by observing large *rf*-pulse reflections when pulsing. This usually implies one of three issues (listed in increasing order of severity):

(*i*) There has been a shear in the soldering. This is difficult to find, but will only require resoldering;

(*ii*) The metal contact of one of the capacitors has become detached from the central ceramic material. These are even more difficult to find, and can result in having to change all of the capacitors one by one in order to find the broken item;

(*iii*) A capacitor has "blown". Sometimes this is relatively easy to spot, since the capacitor will be covered by black marks.

Such *rf*-coil repairs are necessary since using an external tuning and matching architecture to overcompensate for a mis-tuned *rf*-circuit would jeopardize the performance of the *rf*-probe, and the user should rather take precautions and change the damaged capacitor(s).

5. *d*DNP experiments

5.1. Introduction

The main goal of this section is to give a detailed description of the experimental protocol for setting up and optimizing direct ^{1}H (or other nuclear spin) DNP and ^{1}H→X cross-polarization (CP) DNP, and for quantifying the achieved solid-state polarizations and potential errors at any time of the DNP process. The main function of the DNP experiments that are carried out in the context of *d*DNP is to provide the user with maximal polarization levels, often for low-gamma nuclear spins X such as ^{13}C, in a robust, repeatable, and quantified manner, and in a minimum amount of time.

The DNP experiments involve the measurement of the DNP build-up in a way that is precise, and free of all distortions or artefacts that can be present in a highly polarized and low temperature environment. Microwave irradiation needs to be carefully optimized in order to ensure the fastest and/or optimal DNP. Optionally, ^{1}H→X CP can be implemented along with a careful optimization of numerous parameters in order to further boost the polarization, here illustrated with ^{13}C. Finally, the DNP signal may sometimes be compared with the thermal equilibrium signal, that is considerably lower in intensity, in order to properly quantify the nuclear polarization attained. This requires special care to ensure that the nuclear spin system has reached thermal equilibrium and is minimally perturbed in a controlled and quantifiable manner by the NMR pulses used to measure it. Although not often performed in practice, this thermal equilibrium measurement allows one to know the actual polarization levels prior to dissolution, and therefore to quantify the polarization losses that are brought about by the dissolution and transfer steps.

5.2. DNP build-up measurements

Measuring the direct DNP build-up of any particular nuclear spin, often ^{1}H or ^{13}C, generally consists in the following steps:

(i) **Saturating** the initial polarization, either the thermal polarization or the polarization remaining from previous experiments, typically with a train of 90° pulses;

(ii) **Acquiring** NMR signals during the polarization build-up, with small angle pulses, at regular intervals;

(iii) **Estimating** the measured absolute polarization by comparing the polarized signal with a thermal equilibrium signal (measured without DNP, see Section 5.7), and;

(iv) **Analyzing** and possibly correcting for potential artefacts that may affect the estimation of the polarization, such as: (*i*) heteronuclear polarization transfer; (*ii*) polarization depletion, (*iii*) saturation of the receiver; (*iv*) lineshape effects; and (*v*) radiation damping.

Saturating the initial polarization sufficiently may appear trivial at first (with a simple 90° *rf*-pulse for example) but often turns out to be very challenging. Unfamiliar nuclear spin polarization transfer effects can come into play under *d*DNP conditions and interfere with efficient saturation. More precisely, the nuclear spin polarization of invisible spins (the so-called "hidden reservoir") that are physically located near the electron spins (within the so-called "spin diffusion barrier") and therefore strongly coupled to it, may have NMR frequencies far from the carrier frequency and therefore not be affected by the saturating *rf*-pulses [106]. This "hidden" polarization can replenish the polarization of the observed visible spins very rapidly (on a millisecond timescale) during the saturation process, ultimately making the saturation appear incomplete. For that reason, proper saturation sometimes requires a series of 90° *rf*-pulses recycled a number of times with suitable delays so as to entirely deplete the polarization of the "hidden reservoir" (typically 10-30 pulses at 1 ms intervals, repeated 5-10 times at 100 ms intervals).

Acquiring the NMR signal during DNP (after switching on the microwaves) at regular intervals has to be done in a careful manner, but without significantly eroding the polarization nor saturating the receiver (low receiver gains are usually to be preferred especially for high nuclear spin polarizations). This is therefore usually carried out with small nutation angle *rf*-pulses (for example with 0.1 to 5° nutation angles applied every 1 to 5 seconds). The signal, and therefore the polarization, observed with an *rf*-pulse of nutation angle θ are proportional to $S \propto P_0 \sin\theta$, while the remaining polarization after the pulse is $P = P_0 \cos\theta$, where P_0 is the initial nuclear spin polarization before pulsing. Often, the NMR signal can be acquired by an averaged series of n pulse-acquire blocks on a short timescale with respect to the DNP build-up time constant (typically 1 to 64 pulse-acquire events lasting less than a millisecond each, while DNP build-up times are on the order of several minutes). This strategy provides a way to combine high sensitivity without saturation of the receiver and minimal depletion of the building-up polarization. Under such circumstances, the measured summed signal is:

$$S_n \propto P_0 \sin\theta \sum_{i=0}^{n-1} \cos^i \theta \quad (6)$$

While the SNR is:

$$SNR_n \propto n^{-1/2}\, P_0 \sin\theta \sum_{i=0}^{n-1} \cos^i \theta \quad (7)$$

On the other hand, the remaining polarization at the end of the train of pulse-acquire events is simply:

$$P_n \propto P_0 \cos^n \theta \quad (8)$$

As an example, if one measures the DNP signal with a single 5° *rf*-pulse, the observed signal amounts to ~8.7% of the one measured with a 90° pulse-acquire scheme while preserving as much as ~99.64% of the polarization (only ~0.4% is taken away). Typical values used for ^{1}H and ^{13}C at different temperatures are given in Table 3. Figure 21 shows the NMR *rf*-pulse sequence used for pre-saturating and measuring a thermal or DNP build-up curve.

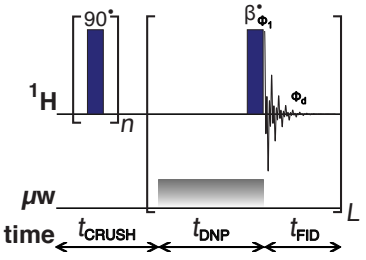

Figure 21: Sequence of *rf*-pulses used for pre-saturating and measuring a thermal equilibrium or DNP build-up curve. Experiments typically use the following parameters: n = 50; t_{DNP} = 5 s; β_{Φ_1} = 0.1°; L = 128. RF-pulse and

receiver phases: $\{\phi_1, \phi_d\}$ = {x, x}. The resonance offset is placed at the centre of the ^{1}H NMR peak.

Table 3: Typical parameters used for measuring NMR signals under DNP conditions for ^{1}H and ^{13}C nuclei in a 7.05 T Bruker Biospin prototype polarizer.

Property	^{1}H		^{13}C	
Temperature	3.8 K	1.2 K	3.8 K	1.2 K
τ_{DNP}	1-2 mins	3-5 mins	20-40 mins	1-2 hrs.
d_1	1-5 s		20-30 s	
RG	0.25-1		1-8	
θ	0.01-1°		1-5°	
n	1-64		1-8	

Estimating the absolute polarization is usually performed by comparing the polarized signal with a thermal equilibrium signal acquired ideally on the same sample, but sometimes on another reference sample (such as line shape polarimetry), see Section 5.8. The measured polarization is:

$$P = P^{TE}\,\frac{S^{DNP}}{S^{TE}}\,\epsilon^{RG}\,\epsilon^{n,\theta} \quad (9)$$

where P^{TE} is the thermal equilibrium polarization, and S^{DNP} and S^{TE} are the DNP and TE signal integrals, respectively. The correction factor for the receiver gain is:

$$\epsilon^{RG} = \frac{RG^{TE}}{RG^{DNP}} \quad (10)$$

with a small receiver gain RG^{DNP} (with an assumed linear scale) often used for polarized signals (so as to prevent receiver saturation) while a higher receiver gain RG^{TE} (typically > 4) is used for the thermal equilibrium signal so as to maximise the SNR (often plateauing for gains larger than 8 depending on spectrometer specifications). The correction ratio for the pulse angles used is:

$$\epsilon^{n,\theta} = \frac{\sin\theta^{TE}}{\sin\theta^{DNP}}\,\frac{\sum_{i=1}^{n^{TE}}\cos^{i-1}\theta^{TE}}{\sum_{i=1}^{n^{DNP}}\cos^{i-1}\theta^{DNP}} \quad (11)$$

With θ^{TE}, n^{TE}, θ^{DNP} and n^{DNP} being the *rf*-pulse nutation angles and numbers of scans used for thermal and polarized signals measurements, respectively. This correction ratio greatly simplifies when the nutation angles used for DNP and thermal equilibrium are the same $\theta^{DNP} = \theta^{TE} = \theta$:

$$\epsilon^{n,\theta} = \frac{(\cos\theta)^{n^{TE}}-1}{(\cos\theta)^{n^{DNP}}-1} \quad (12)$$

For a detailed explanation on the choice of these parameters for the thermal equilibrium signal measurement, see Section 5.8.

Analyzing and possibly correcting for potential artefacts is fundamental for properly estimating the polarization build-up rates or final polarization attained, or at least for being aware of existing sources of error. Here is a list of possible artefacts that might arise in the course of these measurements:

i) **Heteronuclear polarization transfers.** The nuclear spin polarization of other nuclear spins may be relatively high at the very start of build-up measurements, especially if not saturated. Therefore, depending on the DNP history of the sample, high polarizations of other nuclear spins may get transferred to the measured nuclear spins either by direct nuclear→nuclear cross-relaxation (for example from abundant ^{2}H spins in the case of partially deuterated DNP samples) or by more complex electron spin mediated polarization transfers such as the four-spin cross-effect [15] or thermal mixing [107]–[109][108]. Such effects may significantly affect the build-up curves, but in principle not the final polarized steady state (if one waits long enough). Such heteronuclear polarization transfer effects become more intense and problematic when measuring signals with weak DNP enhancements, especially when other nuclear spin species are highly polarized.

ii) **Polarization depletion**. Measuring the NMR signal necessarily implies eroding the nuclear spin polarization. An acquisition performed with a series of n pulses of nutation angle θ will result in an attenuation of the resulting averaged signal measured by a factor $\frac{1}{n}\sum_{i=1}^{n}\cos^{i-1}\theta$ accounting for the nuclear spin polarization remaining for each successive scan. In many cases, for example when the polarized signal needs to be compared with the thermal equilibrium signal for evaluation of the nuclear spin polarization, this needs to be carefully evaluated. This is far from being trivial as it requires a very precise knowledge of the nutation angle used. An error of a few percent on θ can have tremendous impact on the estimation of the polarization, further worsened when using large numbers of pulses n. The following experiment allows one to very precisely evaluate θ directly on the DNP sample during the course of the experiment. We call it the *angle-tune* experiment.

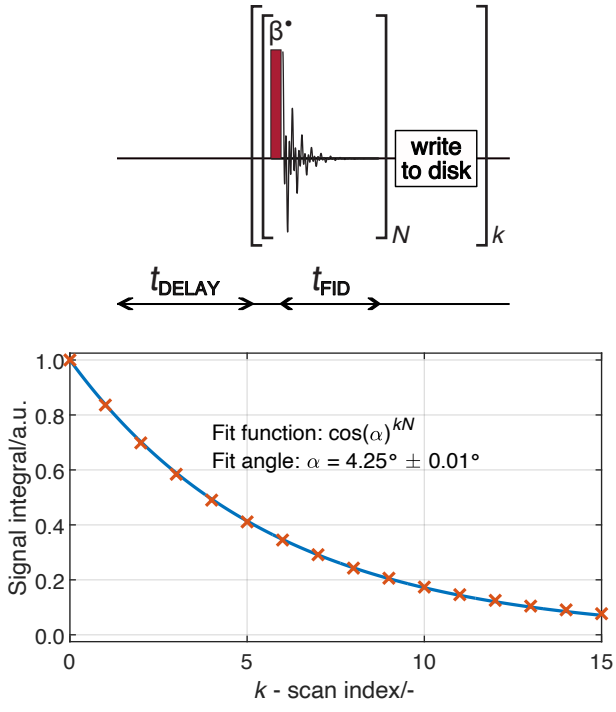

Figure 22: *Angle-tune* approach, where k trains of N pulse-acquire experiments are performed on a timescale which is very short compared to nuclear-spin lattice relaxation. Each of the N pulse-acquire signals is Fourier transformed, integrated and plotted here as a function of the number k of N pulse-acquire events. The decay of the acquired signals, solely due to the depletion of polarization by the applied pulses, can be fitted with equation $S_k = S_0\cos^{kN}\theta$ to precisely determine the nutation angle.

It simply consists of repeating the series of n pulse-acquire segments a small number of times with a short delay, compared to the build-up time constant, and then evaluating precisely the

polarization losses induced by this series of n pulses. One can fit the decay of signal intensities from successive experiments, and determine θ with very high precision, with the following function:

$$S_k = S_0 \cos^{kN}\theta \quad (13)$$

where S_0 is the signal integral after the application of the first *rf*-pulse, N is the number of scans per acquisition block and k is the number the pulse-acquire blocks.

iii) **Saturation of the receiver**. Measuring highly polarized signals often requires the use of a small receiver gain and small nutation angle *rf*-pulses so as to avoid saturating the receiver. Saturation of the receiver is a recurrent issue in *d*DNP and usually implies noticeable anomalies in the free induction decay and Fourier transformed signals.

iv) **Lineshape evolution**. During the course of a DNP experiment, the nuclear spin polarization of one or several nuclear spin species often dramatically increases, violating the high spin temperature approximation, even sometimes approaching values very close to unity. This can lead to changes in NMR lineshapes as observed and reported in some studies [110]–[120]. Such changes in lineshapes are theoretically not a problem for polarization estimation. Indeed, the NMR signal integrals are by nature proportional to the polarization. However, this is only true when the signal is being measured without any dead time after the application of an infinitely short *rf*-pulse. In practice, NMR *rf*-pulses and spectrometer dead times (between pulse and acquisition) are typically on the order of a few (typically 5) microseconds each. On the other hand, under *d*DNP conditions, nuclear spin T_2* can be as short as tens of microseconds. Changes in NMR lineshape can result in significant changes in T_2* decay happening during the pulse and dead time. As a result, NMR integrals can no longer be considered proportional to the polarization, and polarization estimation can become inaccurate.

v) **Radiation damping.** The large magnetization brought about by DNP can lead, under some circumstances, to massive radiation damping effects [121], [122]. Radiation damping can greatly change the NMR lineshape as shown in Figure 23, which can lead to dramatic inaccuracies in polarization estimations. Such radiation damping can lead to the observation of unusual NMR masers under *d*DNP conditions as reported recently [122]–[124]. Radiation damping can sometimes be avoided either by reducing the sample volume, and/or detuning or lowering the quality factor of the NMR circuit, or by implementing more sophisticated suppression methods [121].

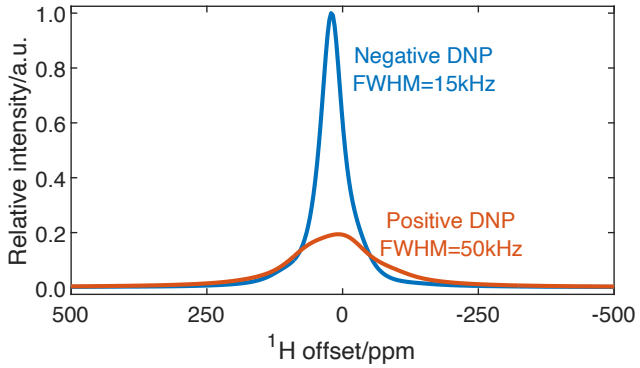

Figure 23: Typical ^{1}H NMR signal measured at 1.2 K on a DNP sample with narrowing by radiation damping of the NMR linewidth for negative polarization (blue) or broadening of the NMR linewidth for positive polarization (orange).

5.3. Microwave optimization

Very few studies report careful optimization of microwave parameters. However, this is key for efficient DNP and sometimes performances can be further boosted by applying a frequency-modulated microwave irradiation rather than a monochromatic one. Microwave irradiation parameters to be optimized are:

(i) Frequency $f_{\mu w}$;
(ii) Modulation type (usually simply triangular);
(iii) Modulation breadth $\Delta f_{\mu w}$;
(iv) Modulation rate f_{mod}; and
(v) Power $P_{\mu w}$.

The optima of these parameters can depend on many factors such as:

(i) Static magnetic field strength;
(ii) Sample temperature;
(iii) Polarizing agent (PA) type;
(iv) Concentration of PAs;
(v) Space distribution of PAs.

In principle, after changing one of these microwave parameters, a DNP build-up needs to be measured over a sufficiently long timescale to attain full DNP equilibrium. In practice, DNP studies often report parameter optimization with short DNP times (therefore without reaching DNP equilibrium). The microwave frequency modulation and power optimization has been described in detail [125]. Further experiments on frequency modulation have been reported and interpreted using numerical simulations [126].

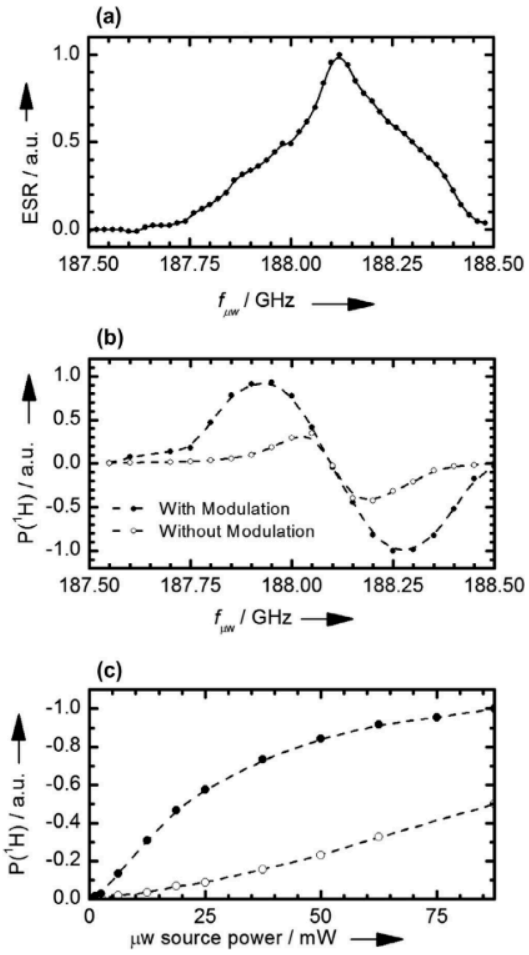

Figure 24: (a) ESR lineshape of TEMPOL measured by longitudinally detected ESR (LODESR) in a DNP polarizer at T = 1.2 K and B_0 = 6.7 T. (b) Proton polarization $P(^1H)$ with and without frequency modulation ($\Delta f_{\mu w}$ = 100 MHz) in a H_2O/D_2O/glycerol-d_8 (1/4/5 *v*/*v*/*v*) mixture with 25 mM TEMPOL, as a function of microwave frequency and (c) as a function of microwave power. Lines are drawn to guide the eye. Adapted with permission from [125].

Figure 24a shows the electron spin resonance (ESR) signal of TEMPOL measured under *d*DNP conditions by longitudinally detected ESR (LODESR) [47]. Each point of Figure 24b shows the ^1H polarization $P(^1H)$ attained for different microwave frequencies $f_{\mu w}$ with and without microwave frequency modulation. Such curves displaying polarization versus microwave frequency are usually called *DNP spectra* or *DNP profiles*. The figure shows that frequency modulation and central irradiation frequency are interdependent parameters, and that using microwave frequency modulation significantly increases the optimal polarization that can be reached by DNP (in this particular example). Figure 24c shows how by using microwave frequency modulation, one can afford better DNP performances with less microwave power $P_{\mu w}$. In this example the polarization was measured for steady-state DNP, which is not often the case for other studies. One should be aware that measuring DNP optima at short times (compared to the DNP build-up time) can result in great distortions of the so-called DNP spectrum and can therefore lead to a suboptimal choice of microwave parameters. This distortion in DNP spectra arises as soon as DNP build-up rates vary as a function of microwave parameters. Figure 25 illustrates clearly how much polarization build-up rates (or times) can vary across the DNP spectrum, by as much as an order of magnitude.

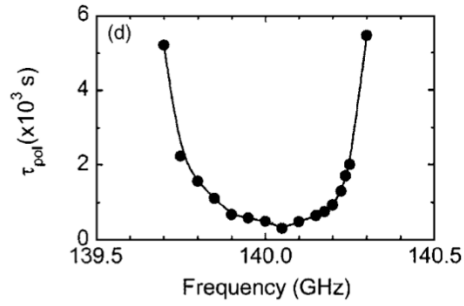

Figure 25: Polarization time constants τ_{pol} measured across the DNP spectrum with 50 mM TEMPOL at 5.0 T. Adapted with permission from [127].

The microwave modulation rate f_{mod} and breadth $\Delta f_{\mu w}$ similarly need to be optimized (see Figure 26). The modulation seeks to provide a way of saturating electron spins over a broader band of the ESR spectrum. It therefore needs to be performed at a rate higher that the electron spin lattice relaxation rate $1/T_{1e}$. This is experimentally observed by the fact that DNP reaches an optimum at sub-kHz modulation frequencies (see Figure 26a). The modulation amplitude also needs to be carefully optimized so as to saturate an appropriate portion of the ESR line that gives rise to constructive DNP. The optimum of the modulation amplitude is usually reached at a fraction of the total ESR width, and DNP tends to deteriorate when modulation is further increased (see Figure 26b).

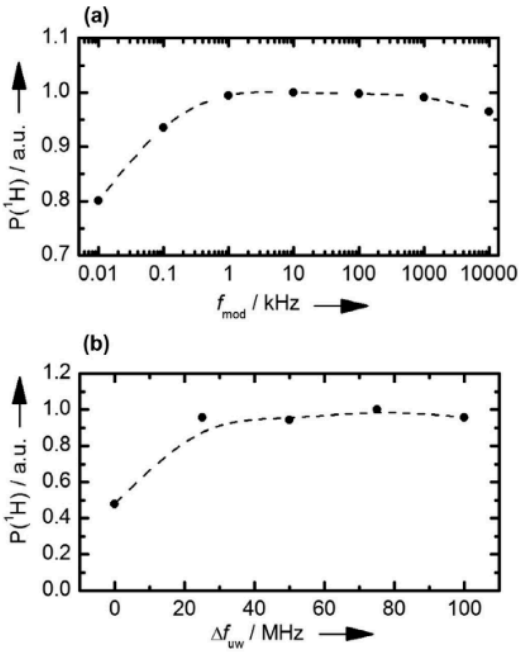

Figure 26: Proton polarization $P(^1H)$ in a H_2O/D_2O/glycerol-d_8 (1/4/5 *v*/*v*/*v*) mixture with 25 mM TEMPOL at 1.2 K and 6.7 T (a) as a function of the frequency of the modulation f_{mod} (with a fixed amplitude $\Delta f_{\mu w}$ = 100 MHz and power $P_{\mu w}$ = 87.5 mW) and (b) as a function of the modulation amplitude $\Delta f_{\mu w}$ (with a fixed modulation frequency f_{mod} = 10 kHz and power $P_{\mu w}$ = 87.5 mW). Adapted with permission from [125].

5.4. Effect of radical concentration

The PA concentration is an important parameter that needs to be optimized as it has a great impact on DNP performance. Figure 27 shows DNP spectra and DNP build-up times (without

microwave modulation) measured for different TEMPOL concentrations ranging from 20 to 65 mM. Changing the PA concentration not only greatly affects the DNP spectrum and therefore the DNP optimum, but also significantly affects the DNP build-up times (here measured at $T = 4.2$ K).

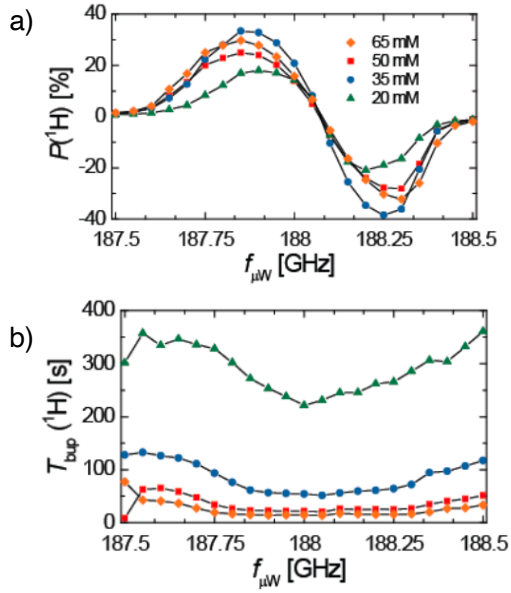

Figure 27: a) Proton polarizations $P(^1H)$ and b) DNP build-up times for TEMPOL at different concentrations in the range 20–65 mM, for different microwave frequencies 187.5 < $f_{\mu w}$ < 188.5 GHz, at $B_0 = 6.7$ T and $T = 4.2$ K. Adapted with permission from [60].

Once the optimal PA concentration is found, together with its optimal microwave irradiation parameters (see Section 5.3), any significant change in DNP, or simply T_1 , time constants, or DNP performances over time is characteristic of either an experimental imperfection (damaged microwave source or attenuated microwave beam), or a sample formulation issue (inadequate radical concentration or scavenged radicals [51]). Therefore, when no ESR apparatus is at hand, simply measuring the T_1 relaxation at 4.2 K (usually on the order of a minute for ^1H) can be a simple tool to assess the sample condition, and more precisely the PA concentration and/or distribution, see Section 3.5.

5.5. Effect of temperature and field

DNP is usually performed at temperatures down to ~1.0 K in helium bath cryostats pumped down to the millibar range (temperatures lower than ~0.9 K are more challenging and not practical for *d*DNP). Going to low temperatures has the advantage of maximizing the electron polarization and therefore the DNP efficiency, however, at the price of longer DNP build-up time constants. Another means of further increasing the electron spin polarization consists of increasing the magnetic field. During the last decade, thanks to the development of high frequency microwave sources that can deliver sufficient power (usually >10 mW needed), DNP has been performed at increasingly higher magnetic fields [59], [127]–[130], ultimately providing electron polarization levels close to unity. Figure 28 shows how temperature and magnetic field affect polarization values and build-up times.

a)

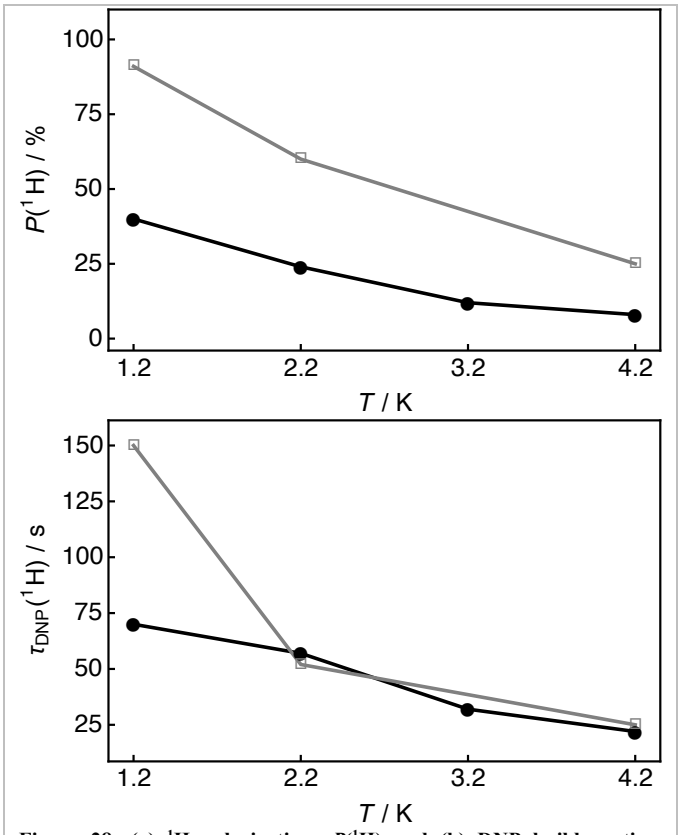

Figure 28: (a) ^1H polarizations $P(^1H)$ and (b) DNP build-up time constants τ_{DNP} in 3 M [1-^{13}C] sodium acetate in D_2O/ethanol (2/1) at different temperatures with 30 mM and 50 mM TEMPOL at $B_0 = 3.35$ T (black) and 6.7 T (grey), respectively. Data adapted with permission from [32].

5.6. ^{13}C CP optimization and multiple-CP

DNP is usually performed on low-gamma nuclear spins such as ^{13}C because of their long T_1 in the liquid-state after dissolution. The most straightforward way to polarize ^{13}C spins consists of directly transferring the electron polarization from adequate PAs such as TEMPO(L) [131], trityl [132], BDPA [133], Galvinoxyl [86], DPPH [37] or other radicals. Amongst these PAs, some have the property of polarizing ^1H spins as well (in particular when their ESR spectra are wider than the ^1H NMR frequency). In that case, not only ^1H spins become polarized, but they become polarized faster and to higher levels (presumably due to the higher gyromagnetic ratio leading to higher DNP transition probabilities, and also presumably faster spin diffusion). It is therefore of interest to combine DNP with cross-polarization (CP) [54] methods in order to take advantage of the highly and rapidly building-up ^1H polarization, and transfer it to the less polarized ^{13}C spins [52], [98], [129], [134], [135]. CP under *d*DNP conditions is very challenging since NMR lines are very broad (typically 10-100 kHz in linewidth) and therefore requires the application of intense *rf*-fields, during extended periods (typically 1-10 ms) in superfluid helium. This can easily result in probe arcing, see Section 4.5.5, and result in the failure of CP experiments. However, suitable *rf*-probe design (see Section 4.2 for an example of an *rf*-coil design suitable for low temperature CP), combined with suitable CP *rf*-pulse sequences have enabled the preparation of very high ^{13}C polarizations with CP in very short timescales. CP provides a way of consistently polarizing a broad range of molecules in standardized DNP solutions, usually containing around 10 M of ^1H spins to ensure proper ^1H spin diffusion and high proximity to the ^{13}C spins, which facilitates the CP transfer.

Demonstrations have been made showing that CP can work equally well with very low ^{13}C abundance (for example in natural samples [136], [137]) or even with deuterated molecules, where CP operates solely from the ^{1}H's of the solvent [138]. One major challenge of such an approach is related to the scaling-up of the sample size (for example for clinical studies) which inevitably requires more *rf*-power and exacerbates arcing issues. Alternatives to conventional CP requiring less *rf*-power are currently being developed and implemented in the context of *d*DNP [139], [98]. The CP strategy that we describe here is the one currently used in the context of *d*DNP that has proven to yield best performances until now.

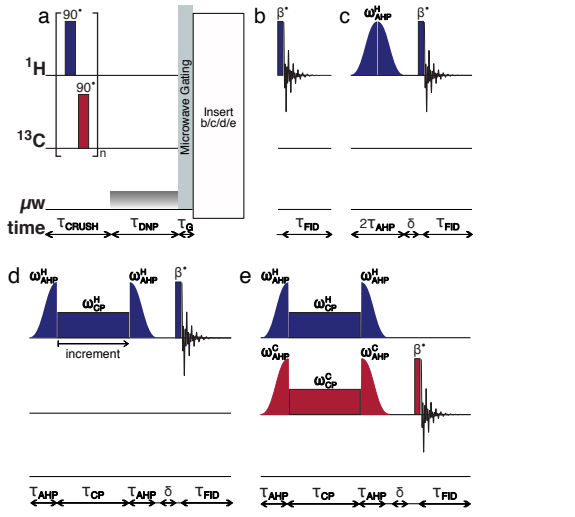

Figure 29: Pulse sequences used for a step-by-step optimization of the cross-polarization *rf*-pulse sequence.

The CP *rf*-pulse sequence used, and its optimization steps, are shown in Figure 29:

(a) **Initializing the polarization**. Saturation of the ^{1}H and ^{13}C polarization by a train of 90° *rf*-pulses, followed by a polarization time (typically 5 s) so as to build-up a repeatable ^{1}H polarization, and finally a microwave gating time (typically 0.5 s) [23] so as to let the electron spins relax to a highly polarized state. Microwave gating results in a dramatic reduction of paramagnetic relaxation during CP and therefore significantly increases the overall performance [23].

(b) **Inspecting the initial ^{1}H polarization level.** Measurement of the ^{1}H NMR signal with a small angle pulse (typically 1°).

(c) **Checking that the adiabatic *rf*-pulses preserve ^{1}H polarization.** An adiabatic half passage (AHP) *rf*-pulse sweep from -100 kHz to the center of the line in 175 ms (with a sweep rate of 0.57 kHzms^{-1}) brings the ^{1}H magnetization in the transverse plane (with a pulse strength of typically $\gamma B_1(^{1}H)/(2\pi)$ = 10-20 kHz), followed by a similar AHP *rf*- pulses sweep from the center of the line to -100 kHz to restore the ^{1}H magnetization along *z*, followed by the measurement of the ^{1}H NMR signal with the same small angle pulse as in step b (typically 1°). The measured signal is compared with the one measured in step b, and typically ~90% is preserved.

(d) **Checking that the spin-lock preserves ^{1}H polarization.** A rectangular pulse with the same phase as the adiabatic *rf*-pulses is placed in between the two adiabatic *rf*-pulses (with an *rf*-pulse strength of typically $\gamma B_1(^{1}H)/(2\pi)$ = 10-20 kHz, and a length incremented from typically 100 μs-5 ms). The measured signal should not show any significant decay during the spin-locking period if the microwaves have been gated off (see Figure 30). At this point, one is reassured that the CP sequence does not wipe out the ^{1}H polarization, and one can therefore implement the full sequence.

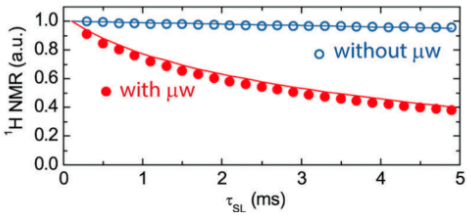

Figure 30: ^{1}H polarization measure after a spin-locking period with the *rf*-pulse sequence described in Figure 30d with and without microwave irradiation. Adapted with permission from [23].

(e) **Transferring the ^{1}H polarization to ^{13}C.** A replica of the ^{1}H pulse sequence is applied on the ^{13}C nuclear spins simultaneously, with identical adiabatic and spin-locking *rf*-pulses, and the ^{13}C signal is measured with a small angle *rf*-pulse (typically 5°). The *rf*-pulse power on the ^{13}C (or ^{1}H) *rf*-channel is optimized in order to match the so-called Hartmann-Hahn condition [53] so as to yield the best transfer of polarization. The length of the ^{13}C and ^{1}H spin lock pulse is optimized separately (typically 1 to 10 ms length) (see Figure 31a for typical optimization curves of the CP contact time). Optionally, one of the square locking pulses can be replaced by a ramp (typically a 50→100% or 80→100% amplitude ramp) to compensate for potential *rf*-coil B_1-field inhomogeneities.

Repeating the CP transfer at optimal time intervals. The maximum ^{13}C polarization is rarely attained with a single CP transfer step, but rather after a series of CP steps performed with optimal time intervals between them. This time interval needs to be experimentally optimized and usually lies between once and twice the ^{1}H DNP build-up time. This can be understood by the fact that one needs to wait after a CP step, for the ^{1}H polarization to build up close to its maximum, before performing another CP step. Figure 31b shows a typical multiple-CP build-up with and without microwave gating. More details regarding the behaviour of the ^{1}H polarization during the multiple-CP experiment can be found in [23]. A detailed study of the optimization of the inter CP delay can also be found in [140].

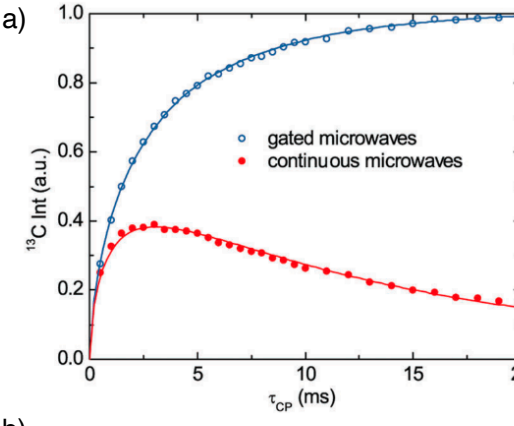

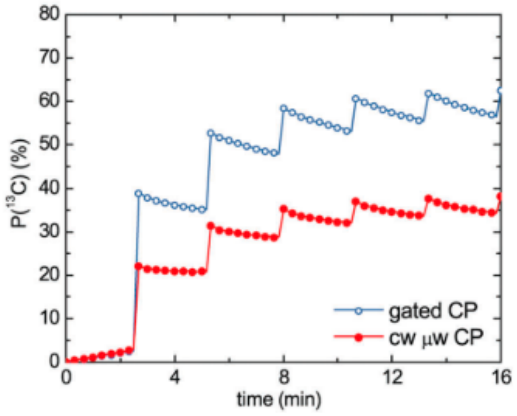

Figure 31: a) ^{13}C signal amplitudes after a single CP transfer from ^{1}H to ^{13}C as a function of the CP contact time τ_{CP}. b) Build-up of ^{13}C polarization $P(^{13}C)$ during a multiple-CP experiment with a CP step applied every 2.5 minutes. All data measured with continuous (●) or gated (○) microwave irradiation with $P_{\mu w}$ = 87.5 mW, $f_{\mu w}$ = 188.3 GHz, $\Delta f_{\mu w}$ = 50 MHz and f_{mod} = 10 kHz in a 3 M sodium [1-^{13}C]acetate solution doped with 40 mM TEMPOL at 1.2 K and 6.7 T. Adapted with permission from [23].

5.7. Thermal equilibrium

Measuring the thermal equilibrium signal of a given sample at a given temperature is in principle the best practice for enabling an accurate quantification of its absolute polarization at any time of a DNP experiment.

When should one measure it? Thermal equilibrium is best measured before any DNP is performed, after the insertion of the sample in the polarizer, so as to prevent heteronuclear polarization transfers from other polarized spins, see Section 5.2. The thermal equilibrium signal must, however, be measured after a sufficiently long time to allow the nuclear spins to reach their thermal equilibrium population distribution.

At what temperature should one measure it? The sample temperature at which the thermal equilibrium should in principle be measured is ideally the same temperature at which the DNP experiment is carried out, so as to make sure that the *rf* properties of the NMR circuit do not change (in particular the *Q*-factor of the probe, and therefore the sensitivity and *rf*-pulse angle for a given power and *rf*-pulse length). Therefore, one would theoretically prefer to measure the thermal equilibrium signal around 1 K. This is however rarely done in practice because T_1 relaxation times tend to become excessively long at such temperatures (typically several hours for ^{13}C [141]). In order to measure the thermal equilibrium signal in reasonable time, one should better measure it at around 4.2 K (or even better at a fixed pressure slightly below atmospheric pressure, resulting in a precise fixed temperature close to 4 K, typically 3.8 K in our studies). Under such conditions, nuclear spin-lattice relaxation times in the presence of free radicals are generally around a few minutes for ^{1}H and less than 1 hour for ^{13}C, depending on the spin system under investigation and the sample radical concentration. However, one has to make sure that the *rf* properties are unchanged, for example, by monitoring the *Q*-factor of the probe with a network analyzer (as explained in Section 4.4.1). At a given magnetic field and temperature, the fully relaxed thermal equilibrium polarization of a spin ½ ensemble can be calculated with Equation 1.

How should one measure it? A procedure routinely used to measure the thermal equilibrium is the following:

(i) **Saturating** the initial polarization (thermal polarization or polarization remaining from previous experiments), typically with a train of 90° *rf*-pulses;

(ii) **Acquiring** NMR signals at regular intervals during the polarization build-up, with small θ^{TE} and n^{TE} so as not to deplete the polarization that is building up, however, with sufficient RG^{TE} so as to maximise sensitivity, see Section 5.2;

(iii) **Estimating** the relaxation time and ensuring that a steady-state thermal equilibrium is attained (see Figure 32);

(iv) **Acquiring** an NMR signal S^{TE} possibly with enhanced sensitivity for better estimation of the polarization (see Figure 33), *i.e.,* with larger θ^{TE} and number n^{TE} of pulse-acquire events, see Section 5.2;

(v) **Subtracting the background signal**, arising from the sample cup and the *rf*-probe itself, measured without DNP sample, with the same procedure (*i*→*iv*).

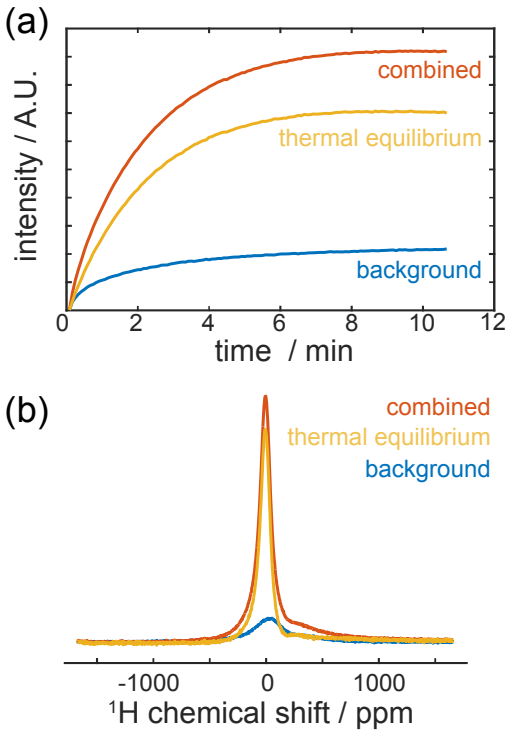

Figure 32: a) ^{1}H build-up of the background (BG) signal and thermal equilibrium signal with background (TE+BG), and after subtraction of the background (TE). b) Corresponding NMR spectra. Experiments were performed at 3.8 K and 7.05 T on a 100 □L sample of 3 M [1-^{13}C] sodium acetate solubilized in H_2O/D_2O/glycerol-d_8 (1/3/6 *v*/*v*/*v*) containing 50 mM TEMPOL. Parameters for signal acquisition were: $\theta^{TE} = \theta^{DNP} = 0.1°$, $n^{TE} = n^{DNP} = 64$, $RG^{TE} = 16$ and $RG^{DNP} = 0.25$.

Often, for ^{1}H spins, a more sensitive acquisition is not always required, as relatively high SNRs are attained with very small nutation angle *rf*-pulses (typically 64 *rf*-pulses of 0.1°) leading to an insignificant depletion of only 0.001% of the initial polarization. For ^{13}C, the build-up of the thermal equilibrium signal is typically acquired with 5° *rf*-pulses (a small number, typ. 1 to 4, for minimal saturation but sufficient sensitivity) applied every 5 to 20 minutes, followed by a train of up to 64 *rf*-pulses of 5° so as to maximize sensitivity. Figure 33 shows how remaining polarization and resulting sensitivity are affected by the number n^{TE} of 5° pulse-acquire events used for measuring the NMR signal. As an example, a train of n^{TE} =

16 pulse-acquire units with a nutation angle of 5° results in an NMR sensitivity corresponding to 33.4% of the maximal theoretical SNR (of a single 90° pulse-acquire event), while depleting the polarization by only 6%.

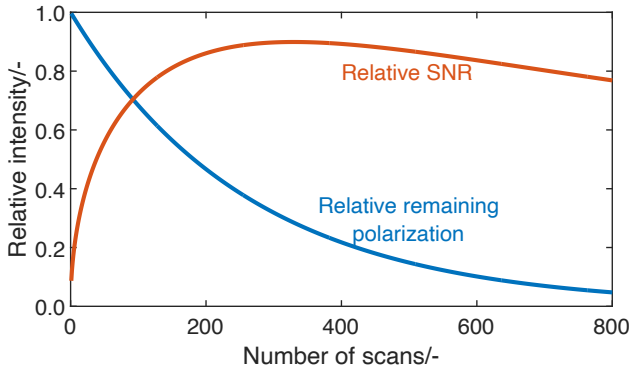

Figure 33: Polarization fraction remaining as a function of the number of 5° *rf*-pulses applied (blue) and corresponding SNR obtained (red, normalised with respect to a single 90° pulse-acquire experiment).

A substantial depletion of the ^{13}C polarization is necessarily induced by such an approach, but this does not matter in principle since the DNP sample is meant to be subsequently re-polarized. The depletion can be estimated by directly repeating the same acquisition as described in Section 5.2 and Figure 22 (using the so-called angle-tune experiment). Such a procedure provides a way to both measure a thermal equilibrium signal with good sensitivity and estimate the nutation angle precisely which is important to quantify precisely the absolute polarization brought by DNP.

What if it cannot be measured? Sometimes the thermal equilibrium signal cannot realistically be measured because of the low number of spins in the sample (for example, in the case of low concentrations of molecules at ^{13}C natural abundance), or because nuclear spin-lattice relaxation times turn out to be too long (for example, with low concentrations of PAs below 10 mM). In such cases, provided that the number of nuclear spins in the sample is known, one can estimate the polarization by cross-calibrating with a reference sample with a higher known number of nuclear spins (ideally fast relaxing). One example of such a reference sample cited earlier that has sometimes been used in our laboratory is a 3 M [1-^{13}C] sodium acetate solubilized in H_2O/D_2O/glycerol-d_8 (1/3/6 *v*/*v*/*v*) containing 50 mM TEMPOL. This method, although it is routinely described in the literature, and automatically implemented in commercial polarizers, ought to be avoided if possible, for several reasons that makes it hardly quantitative: (*i*) the presence of PAs bleaches part of the NMR signal [142][143], possibly in a different way in the DNP and reference samples, and (*ii*) the NMR lineshape can differ in both samples which affects the signal attenuation during the spectrometer dead time [144], see Section 5.2.

6. Mechanics of sample dissolution and transfer

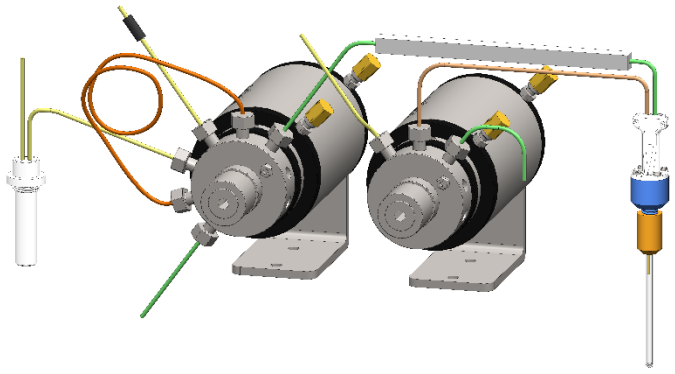

Figure 34: 3D overview of the dissolution, transfer and injection system based on a liquid-driven system, including a sample cup (left) for dissolution, a set of two 10-way valves (middle), a loop (orange capillary) and an optical sensor (black, top left) for the sample bolus selection, a liquid pump (not shown), a magnetic tunnel (top right) for transferring the selected sample, and an injector (right) for injection.

6.1. Introduction

The objective of this section is to describe the hardware and the protocols for dissolution, transfer and injection in *d*DNP experiments. Dissolution takes place after the frozen sample has been polarized to a satisfactory level. This is followed by the transfer and injection of the sample in a separate NMR spectrometer. These steps will be described, as well as the main challenges of the approach, and the pros and cons of the existing solutions. A particular focus will be placed on the hardware of such dissolution systems.

The main purpose of the dissolution process in *d*DNP experiments is to melt the frozen hyperpolarized sample while retaining the high nuclear spin polarization that is brought about by DNP, and to transfer it to an associated NMR or MRI machine. This process can be split in three parts: (*i*) the dissolution aims to warm up the frozen sample (initially at *ca.* $T = 1.2$ K) as fast as possible, to minimize polarization losses, and to melt the sample completely to make it available for liquid-state analysis; (*ii*) transferring the liquid hyperpolarized sample to an NMR machine for analysis requires special attention in terms of speed and magnetic field along the transfer pathway to minimize relaxation in the liquid-state. Typically, ^{13}C spins may relax towards thermal equilibrium in tens of seconds, while other nuclear spins such as ^{1}H may relax in a matter of a few seconds. This highlights the need for a fast transfer to keep the highest polarization possible and enable hyperpolarization and subsequent dissolution of faster relaxing nuclear spins. Having a reproducible means to transfer a precise and controlled sample volume is also of great interest so as to enable reproducible injections; and (*iii*) injecting the hyperpolarized sample into a dedicated receiver while minimizing fluid motions, gas bubbles and degassing processes in the NMR detection coil is desirable in order to prevent inhomogeneous line broadening. Reproducibility in terms of timing, volume and analyte concentration, in order to ensure reproducible *d*DNP-enhanced NMR spectra, is also greatly desired. Finally, the NMR system needs to be prepared in an adequate state including pre-shimming on a similar solution before dissolution to ensure the acquisition of high-resolution spectra.

The following sections will detail the different steps of the dissolution process:

Dissolution system. To achieve fast dissolution, a large amount of heat needs to be rapidly transferred to the sample. This includes the energy needed to warm up and melt the frozen sample of *ca.* 50-200 µL at ~1 K, as well as the losses due to heat exchange with the system along the solvent path, including the capillary walls and sample cup. While many strategies can be designed, one commonly uses hot pressurized solvents such as D_2O for this purpose. The chosen solvent is pushed using helium gas onto the sample through capillaries, dissolves the sample, and is then pushed and transferred out of the polarizer. Two strategies exist to couple the capillaries to the sample cup for the dissolution: (*i*) either by coupling a warm dissolution stick to the cold sample cup; or (*ii*) using a built-in fluid path already attached to the cold sample cup. Great attention has to be given in both cases to the temperature of the dissolution solvent, the helium gas pressure, and the capillary diameters to ensure complete melting of the DNP sample and to prevent freezing along the fluid path. Melting of the sample can under some circumstances be improved by modifying the geometry of the inlet capillary to the DNP sample with a so-called "nozzle" (freezing the DNP sample into small pellets, rather than a block may also help). In addition, the dead volume of the sample cup must also be carefully considered to minimize mixing-induced bubbles which may affect the reproducibility of the transfer.

Transfer system. The hyperpolarized sample is usually transferred over a few metres of capillary with a driving fluid which is either a gas or a liquid. Gas-driven transfer has the advantage of being simple as the dissolved sample is directly pushed from the sample cup into a receiving container situated within the bore of the NMR spectrometer. One problem that can arise with this strategy is that the hyperpolarized sample, which initially presents itself as a single liquid bolus in the capillary, may be "contaminated" by the pushing gas during transfer. This may be due to turbulences, high speed, and slow transfer, which can lead to the fragmentation of the bolus of the dissolved sample. Transferring a mix of liquid and bubbles will lead to a poor transfer and injection reproducibility. It is possible to limit this problem by adjusting the capillary's diameter and the driving pressure of the gas, usually at the expense of speed. Liquid-driven transfers do not suffer from such problems and can achieve fast and high precision injections, especially over long distances using high performance liquid pumps. This method involves the use of dedicated valves that first select a bolus of the hyperpolarized sample just after the dissolution, and then transfer this bolus using a dedicated pump (see Figure 34 for a schematic representation of such a system). In this case, turbulences may induce mixing between the driving liquid and the dissolved sample along the transfer. Such mixing can contaminate the front of the dissolved hyperpolarized sample bolus which is ultimately injected. The capillary diameter, the driving flow as well as the driving liquid properties must be carefully chosen to prevent such contaminations. Another important concern with the transfer of the hyperpolarized sample is the loss of polarization due to zero to low field regions. The mechanisms responsible for this loss are discussed in Section 7. Several approaches exist to produce a field high enough to limit polarization losses, generally using permanent magnets or electromagnets.

Injection. The injection of the dissolved sample requires a dedicated device that holds the NMR tube, here called the injector. We will limit ourselves to the case of 5 mm NMR tubes, as those are more frequently used. Since many applications require reproducibility, precise control of the injected volume and sample concentration is important. Having

a fully automated system that selects a desired volume can be an answer, since it can improve reproducibility. Another way consists of transferring the whole bolus to a reservoir prior to injection, which is time consuming and ultimately less reproducible [52]. Finally, avoiding broadening of the NMR linewidth is essential to reaching the standard of high-resolution NMR. Compared to direct classical acquisition, *d*DNP involves fluid motion due to the transfer and injection, and micro-bubbles potentially caused by degassing. Both will lead to line broadening. Among the ways of dealing with those issues, using liquid-driven transfers can help reduce fluid motion, applying a back-pressure can limit degassing and treating the NMR tube walls with dedicated solutions can prevent bubble blockage during injection.

6.2. Dissolution strategy

6.2.1. System preparation for dissolution

After achieving a satisfactory level of polarization, the dissolution step is conducted, which consists of sending a hot liquid solvent into a cryostat filled with liquid helium. A few points must be taken into consideration before starting the dissolution step.

First, the hot solvent must be warmed prior to dissolution. The solvent, usually D_2O, is placed in a reservoir surrounded by resistive wires. A simple power supply can then warm up the solvent to the desired temperature. Pressure is often chosen to monitor the solvent temperature, since it can be more difficult to precisely know the temperature inside the heater. To reach higher temperatures, the solvent is first pre-pressurized with helium gas at room temperature, and then warmed up until the pressure of the heater reaches a target value. In our laboratory, we usually pre-pressurized the solvent up to 6 bar, and then warm up to 9 bar. The heating step takes ~10 mins and should be started before the end of the polarization step to synchronize with the time when the build-up of the polarization is optimal.

A key point for numerous successful dissolutions is to decrease thermal contact between the sample cup and the liquid helium bath. While having liquid helium surrounding the sample cup during dissolution will lead to a big heat load in the bath, thus wasting liquid helium, it will also lead to increase the risk of freezing the dissolution solvent. The sample cup must therefore be lifted above the liquid helium bath, usually using dynamic o-rings or standard compressed o-rings. Liquid helium level sensors can prove useful to determine the height of the lift.

Considering the long T_1 of commonly studied nuclei such as ^{1}H and ^{13}C at liquid helium temperatures, *rf*-pulses and microwaves should be stopped prior to the dissolution process. Though dependent on the nuclear species, relaxation will be negligible in most cases during the time span required to start a dissolution. See Section 7 for more details regarding relaxation during this step.

When sending the hot solvent onto the sample, input and output capillaries must be connected and coupled to the sample cup to avoid spraying solvent into the cryostat. Two main approaches exist: (*i*) the capillaries are connected to the sample cup during the entire polarizing step using a so-called “fluid-path”; or (*ii*) the capillaries must be manually connected just prior to the dissolution. Both approaches will be discussed in more detail in the following subsections. However, the latter usually necessitates opening the cryostat to insert a tube, here called a “dissolution stick”, containing the input and output capillaries. To avoid cryo-pumping during this operation, an overpressure of helium gas is applied, usually a few tens of millibar above atmospheric pressure. The increase in pressure in the cryostat will induce an increase in the sample temperature, since the helium bath temperature will rise to ~4.2 K. A fluid-path associated with dynamic o-rings allows dissolution in a pumped cryostat, with a ~1 K helium bath temperature.

6.2.2. Shimming procedure

While increasing the NMR signal amplitude (integral) of the sample is the main goal of *d*DNP, having high resolution spectra is also of great importance. The relaxation of the hyperpolarized species in the liquid-state prevents the user from shimming after the injection. Instead, proper shimming parameters must be known before performing the dissolution. A possible method used in our laboratory is to perform a “fake” dissolution in liquid nitrogen outside the polarizer on a similar, ideally identical, sample using the same solvent, pressure and temperature as in the actual dissolution. Indeed, there is no need for hyperpolarization here. Shimming can then be optimized on the sample injected through the injector. The same shimming parameters are then used for the actual dissolution experiments, resulting (in our case) in ^{13}C linewidths of <1 Hz on [1-^{13}C] sodium acetate dissolved in D_2O solvent at 700 MHz.

After preparing the system, including the shimming procedure, one is now ready to perform a dissolution by coupling input and output capillaries to the sample cup. The design details of two approaches will be presented in the next section.

6.2.3. Dissolution stick and fluid path

When considering the dissolution process, one has to consider how to connect the cooking pot to the sample cup. Two predominant methods are used: (*i*) manually coupling a dissolution stick; or (*ii*) using a fluid path.

The first approach consists of a tube housing two capillaries, one for injecting the hot solvent and one for ejecting the hyperpolarized solution. Both capillaries are attached at the bottom of the tube to a so-called “dissolution interface”. This part, usually machined in polytetrafluoroethylene (PTFE) or in polyether ether ketone (PEEK), has a specific geometry used to couple it to the sample cup. The system is made leak-tight by manually pressing the dissolution stick to the sample cup. The coupling must be done just before sending the hot solvent, to reduce heat transfer from the warm dissolution stick to the cold sample, which would decrease the nuclear spin polarization in the solid-state. Thus, using a dissolution stick requires trained operators.

Figure 35 shows the design of our dissolution stick. The sample cup is screwed to a washer and soldered to an outer stainless-steel tube. During the dissolution step, the dissolution stick is inserted inside the outer tube, and is coupled to the sample cup. A small stainless-steel tube is used to reduce the inner diameter of the input capillary to improve the dissolution efficiency. This will be discussed in more detail in a following subsection.

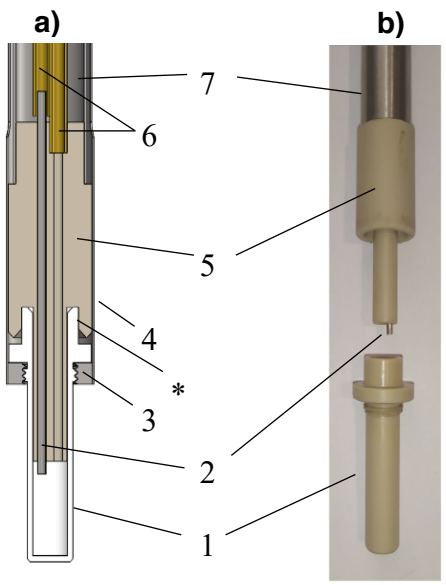

F : a) 3D model and b) photograph of the dissolution stick and sample cup, comprised of: (1) PEEK sample cup; (2) 1/16'' OD stainless-steel tube; (3) washer with screwing hole; (4) 16 mm OD stainless-steel tube; (5) PEEK dissolution interface; (6) two 1/8'' OD and 1/16'' inner diameter (ID) PEEK tubes; and (7) 13.37 mm OD stainless-steel tube. *Shows the area that must be made leak tight at the time of the coupling.

Another approach consists of keeping the input and output capillaries attached during the whole polarization step. Such a method has important advantages: (*i*) it becomes possible to perform a dissolution without opening the cryostat to couple the capillaries, thus allowing a dissolution at ~1 K; (*ii*) no trained operators are needed for the dissolution step, since no manual coupling is required; and (*iii*) by using dynamic o-rings it becomes possible to automate the whole dissolution process, including the lifting of the sample cup prior to sending the hot solvent. Such automated processes are a crucial step towards making *d*DNP accessible for all and improving reliability and reproducibility.

The main problem when dealing with a fluid path is to make the sample/capillaries leak tight with respect to superfluid liquid helium. Indeed, if the liquid helium of the bath enters this system, it will fill the capillaries, creating a column of liquid helium that will most likely freeze the hot solvent during the dissolution. Ardenkjær-Larsen et al. showed the first fluid path [92], [145], originally designed for the commercial *SPINLab*. It features concentric capillaries, with the hot solvent coming through the inner one, and coming out through the annular space between the concentric tubes. A UV-cured epoxy (*Dymax Corp*, CT, USA) is used between the outer tube and the sample cup to obtain a leak tight system. Due to the sterility requirements of the *SPINlab*, this fluid path can only be used once. The same group has developed two other non-sterile versions [146], [147]. The concentric capillaries are glued onto an intermediate part, which is screwed to the sample cup with a disposable PTFE o-ring (see Figure 36). This reusable fluid path makes it easier to access the sample cup.

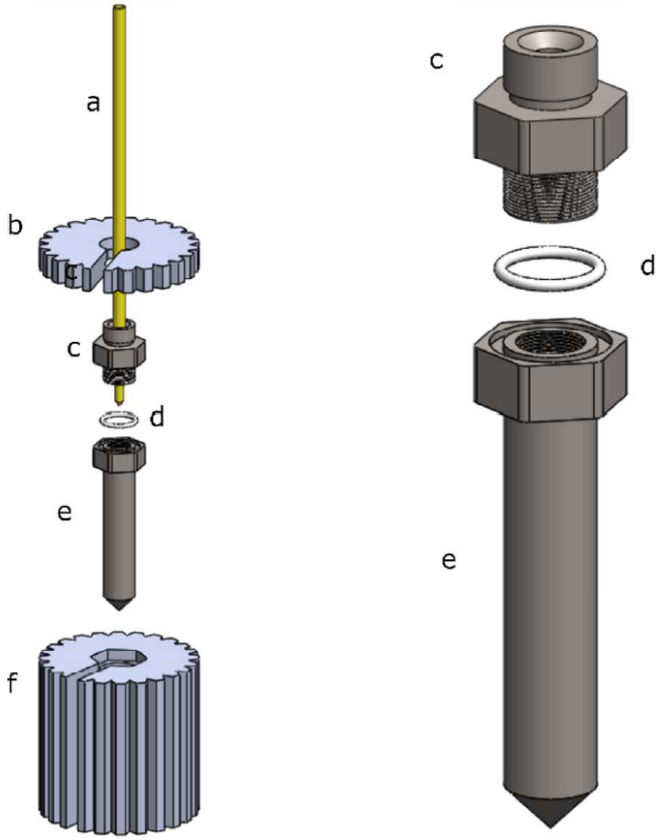

Figure 36: Alternative version of the fluid path developed by Capozzi et al. [146]**. The sample cup (e) is screwed to the intermediate part (c), and is made leak tight using a PTFE o-ring (d). The concentric capillaries (a) are glued using an UV-cured epoxy onto the intermediate part. Homebuilt wrenches (b) and (f) are used to tighten the o-ring. Adapted with permission from**[146]**.**

Krajewski et al. proposed a method that combines the two discussed above, with a dissolution stick present in the cryostat during the polarization step, but not coupled to the sample cup [148]. A motor is triggered just prior to the dissolution to lift the sample cup above the liquid helium bath and couple it to the dissolution stick without pressurizing the cryostat. This automated dissolution system allows up to four samples to be polarized simultaneously in the cryostat.

To complete the idea of performing the dissolution in a ~1 K liquid helium bath, a gate valve system has also been proposed to insert the sample cup without pressurizing the cryostat [92], [130], [148], [149]. The sample is first inserted into a closed chamber from which the air is pumped. A lower gate valve is then opened to the cold cryostat and the sample cup is inserted using a dynamic o-ring. This system prevents the cryostat from warming up due an overpressure, thus reducing the loss of helium. However, it requires a more expensive and complex instrumentation.

Once the sample cup is lifted and coupled to the input and output capillaries, hot solvent can be sent onto the sample to dissolve it. One must consider the amount of energy needed to melt the sample for this step.

6.2.4. Energy required for dissolution

During the dissolution process, a certain amount of heat must be transferred to the sample to make sure it will melt, as well as to make sure that the solvent will not freeze. This heat is directly linked to the solvent volume and temperature. To

determine the volume and temperature, one could start by looking at the energy needed to melt the sample. However, as Bowen and Ardenkjær-Larsen showed [150], when a mass of solvent ~10 times higher than the mass of the sample is warmed up to 170 °C, ~5% of the heat available is needed to melt the sample and bring it to room temperature. At this point, it is reasonable to assume that too much solvent was used. However, as presented in their article, the frozen sample is not always recovered in the liquid-state after the dissolution (see Figure 37). The sample recovery gets worse when lowering the solvent temperature. The reason is that a large part of the heat is transferred to the system components, such as the capillaries or the valves. The efficiency of the heat transfer to the sample is also important, but this will be discussed further in the next subsection.

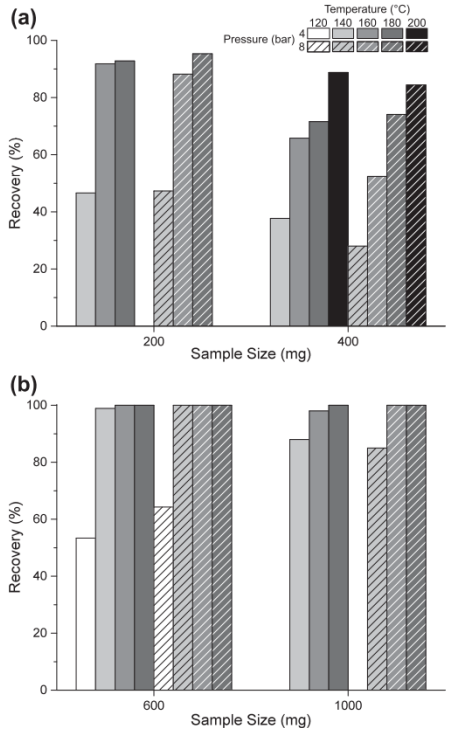

Figure 37: Recovery of acetate samples (sodium acetate/glycerol/H_2O (4.7/2.1/3.2 *w/w/w*) with 0.5 mM of bromocresol green) depending on the solvent temperature, pre-pressurization and sample size. (a) 4 mL of solvent (water) was used. (b) 10 mL of solvent (water) was used for larger sample sizes. Adapted with permission from from Bowen and Ardenkjær-Larsen [150]**.**

Freezing, which can happen if the dissolution stick or fluid path are poorly cleaned and dried prior to dissolution, can also occur if the solvent temperature is not high enough. The dissolution efficiency can be optimized through different parameters and is presented in the next subsection.

6.2.5. Optimizing the dissolution efficiency

With either a dissolution stick or fluid path, a few key parameters must be considered when dealing with the dissolution: (*i*) the volume and temperature of the solvent; (*ii*) the pressure at which the solvent is pushed; (*iii*) the diameters and length of the capillaries; and (*iv*) the dead volume of the sample cup.

Solvent volume and temperature, as discussed above, must be chosen so that enough energy will be available to melt the sample and avoid freezing. Freezing is also linked to the diameter of the capillaries in the polarizer, since smaller capillaries will increase the contact surface of the solvent to the cold capillary walls. Longer capillaries also increase the contact time and thus the risk of freezing, but this parameter is usually set by the polarizer design.

One study by Ardenkjær-Larsen et al. [151] investigated the dissolution efficiency depending on the solvent velocity and temperature, and showed that the jet impingement of the solvent onto the frozen sample plays an important role in speeding up the sample dissolution. Higher solvent mass flow rates, due to higher pushing pressure of the solvent and smaller capillaries, increases the impingement. However, it will decrease the contact time between the solvent and the sample, which decreases the efficiency of the heat transfer by diffusion. The study also showed that the solvent tends to vaporize when entering the sample cup, which lowers the heat transfer capability. To prevent this, the capillary diameters must be carefully chosen, and the solvent temperature should not be too high. Furthermore, adding a step diameter, a nozzle, can significantly improve the melting efficiency [150], [152]. Indeed, a nozzle will increase the flow rate, and thus the impingement, and decrease vaporization. By carefully choosing its dimensions, Ardenkjær-Larsen et al. showed that a pyruvic acid sample could be entirely dissolved in 4 s using a nozzle, whereas a part of the sample still remains solid when no nozzle is used, even after all the solvent went through the sample cup (10 s later, same solvent parameters in both cases).

Finally, the dead volume of the sample is also important, since it will affect the efficiency of the following transfer. Indeed, the sample cup volume is a place where the initial helium gas can mix with the solvent due to high turbulences. This mixing induces bubbles and makes precise and repeatable transfers complicated. To reduce this effect, we lengthened the dissolution interface of our dissolution stick with a cylinder that enters the sample and fills a part of the dead volume (see Figure 6.2).

The dissolution process can be complex from a thermodynamic point of view and finding the optimal parameters can be challenging. After melting the sample, one has to transfer it as fast and as possible for analysis.

6.3. Transfer and injection for a gas-driven system

6.3.1. Direct gas-driven transfer

Originally, the dissolved sample leaving the polarizer was gathered in a reservoir, and injected manually into a 5 mm NMR tube [9]. Although simple, this method is relatively slow and the transfer to the NMR tube happens in low field, potentially inducing additional polarization losses, see Section 7. Furthermore, the timing is hardly repeatable, which affects the reproducibility of the signal amplitude ultimately measured.

Although this method still exists, especially for MRI applications [148], [153], efforts have been made towards automated injection of the hyperpolarized sample. Jannin et al. have reported an automated system that first gathers the liquid sample in a reservoir to mix it homogeneously with the solvent, and then injects a controlled volume into the NMR tube. Overall timings of ~7-10 s were obtained [52], [129], [154], [155]. By injecting directly into the NMR tube and carefully controlling the driving gas pressure and internal capillary diameters, Granwehr et al. [156] obtained a transfer time of ~2.5 s. Pinon et al. [147] decreased the transfer time down to ~2 s, though their approach injected the sample in a 10 mm NMR tube,

which allows higher driving pressure without risking a blockage due to bubbles during the injection. Frydman at al. showed transfer times as fast as ~1.2 s [157] using non-miscible solvents. Pushing forward the idea of faster transfer, more sophisticated and exotic approaches have been proposed, as presented in the next subsection.

6.3.2. Dedicated transfer system

Instead of pushing a liquid hyperpolarized sample, Meier et al [34] transferred the sample in the solid-state, in a pellet of PTFE. The dissolution and injection take place inside the NMR spectrometer. A transfer time of ~70 ms, with ~ 800 ms for the dissolution and injection, was reported. Another way of reducing transfer time is to shorten the distance between the polarizing and acquisition areas. Two different groups have proposed to integrate both areas in the same device. The time between the dissolution and analysis has been reported to be 700 ms [33] and 300 ms [158]. Although extremely fast, such methods require dedicated, complex and expensive infrastructures.

To improve the transfer speed in a more classical way, Hilty et al. developed a transfer and injection device comprised of a 8-way valve and a two different driving gas pressures [159]. After dissolution, a portion of the hyperpolarized sample is first selected in a capillary called a loop, whereupon the 8-way valve is switched, connecting the loop to the second driving gas pressure for the transfer to the NMR tube. An overall timing from dissolution to analysis was reported to be ~1.2 s. This transfer system has also been implemented in other laboratories [160], [161]. One should note at this point that the sample selection in the loop must be done carefully if good reproducibility is desired. Indeed, the sample concentration profile is not constant across the bolus of solvent, as shown by Bowen and Ardenkjær-Larsen [150] (see Figure 38). After switching the 8-way valve, the highest concentration of the profile should be at the front of the bolus, increasing the sensitivity and decreasing concentration variations.

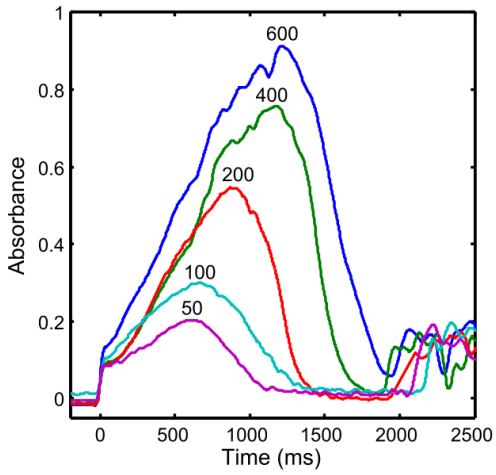

Figure 38: Absorbance, proportional to the sample concentration, along the solvent bolus after dissolution, depending on the sample size (50-600 mg aliquots). The sample, sodium acetate/glycerol/H_2O (4.7/2.1/3.2 *w/w/w*) with 0.5 mM of bromocresol green, was dissolved in H_2O. Adapted with permission from from Bowen and Ardenkjær-Larsen [150].

When pushing a liquid over long distances with pressurized gas, contamination by bubbles will occur and can ultimately degrade injection.

6.3.3. Bubble contamination

When a liquid is pushed in a tube using gas as the driving fluid, mixing will occur due to turbulences [156], [162], creating bubbles along the liquid bolus of liquid. Increasing the gas pressure, and thus the transfer speed, will increase the turbulences and therefore the extent of the resulting mixing. Furthermore, the liquid will leave a trail along the tube walls, decreasing the liquid bolus length [163]–[166]. This trail becomes thicker when increasing the gas pressure and thus the transfer speed. Transfer over longer distances will also imply a shorter liquid bolus at the time of injection. Such a loss of liquid bolus will decrease the reproducibility of the injection.

6.3.4. Injections with gas-driven transfer

Injecting a gas-driven liquid sample can be difficult. Especially when injecting in a 5 mm NMR tube, since gas bubbles might be present in the coil detection area. Furthermore, after ending the injection, the driving pressure is released, inducing degassing within the sample [156], [159], [160]. The resulting microbubbles will broaden the signal. Hilty et al. proposed a system with an applied back-pressure at the end of the injection step to prevent degassing [159]. Fluid motion after injection has been reported [156], [160], [167], which also leads to line broadening.

For most injections, a custom-built injector has to be developed. Such injectors must hold the NMR tube, include the input capillary through which the liquid is injected, as well as an exhaust for the gas. It also has to fit within the NMR spectrometer bore. If a back-pressure is applied, the injector must remain leak tight and resistant to pressure, usually in the order of 10 bar. Our homebuilt injector is presented Figure 39. It includes a 5 mm medium-wall NMR tube that handle up to 10 bar of pressure, an input 1/16'' OD capillary for injection and an 1/8'' OD capillary for exhaust and back-pressure gases. A custom 3D printed spinner, made leak tight with o-rings, links the capillaries and the NMR tube.

Very few studies have investigated the reproducibility of the obtained liquid-state polarization level with a gas-driven transfer. Indeed, the compressibility of the gas used might prove to be an obstacle in reaching an acceptable level of reproducibility. Krajewski et al. [148] have reported a polarization level of 18.7 ± 2.3% over 24 experiments, using four different dissolution sticks. This study, however, was for *in vivo* studies in rats, using a small animal MRI system. Bornet et al. showed, over 8 dissolutions with a 500 MHz spectrometer, a coefficient of variation of ~3.6% [154]. Even though this work requires trained operators for the dissolution process, such repeatable results such repeatable results have paved the way towards applications requiring high repeatability, such as hyperpolarized metabolomics studies [136].

Gas-driven transfers are the most widely used method in *d*DNP. However, the approach has challenging fluidic issues that could be overcome by using a different driving fluid, as presented in the next section.

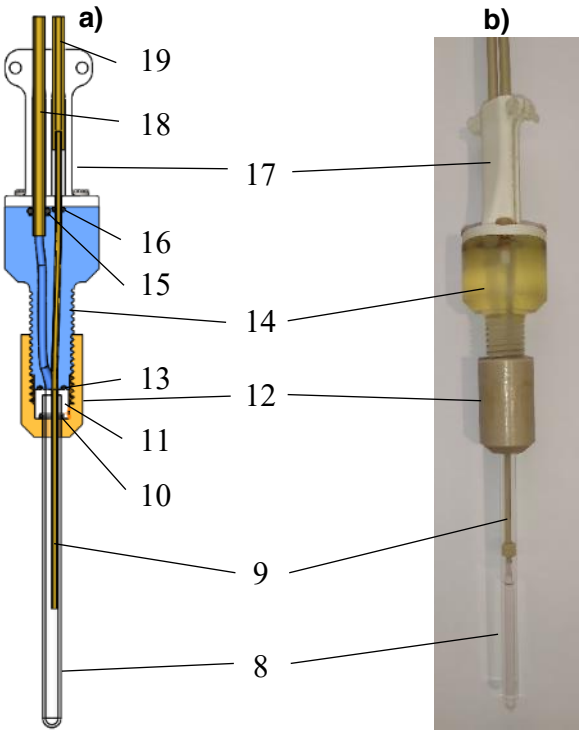

Figure 39: a) 3D model and b) photograph of an injector, comprised of: (1) 5 mm NMR tube with 3.4 mm ID; (2) 1/16'' OD PEEK tube; three o-rings with 1 mm cross section and 5 mm ID (3), 5.5 mm ID (6) and 1/16'' ID (9); (4) tube head in PEEK; (5) custom-made PEEK nut; (7) 3D-printed custom spinner; (8) o-ring with 1/16'' cross-section and 1/8'' ID; (10) 3D-printed plug; two 1/8'' OD PEEK tubes with 2.2 mm ID (11) and 1/16'' ID (12).

6.4. Transfer and injection for a liquid-driven system

6.4.1. Liquid-driven transfer

Considering the challenges brought by gas-driven injection, one might consider pushing the sample with a different fluid. Hilty et al. developed a liquid-driven transfer based on their previously described fast gas-driven transfer [167], [168]. The selection of a part of the sample in a loop capillary using a 10-way valve remains the same, but a powerful liquid pump is triggered to transfer the loop segment instead of pressurized gas. Such systems can achieve fast transfer times, with ~0.7 s reported (~1.6 s for the overall dissolution to injection time).

Although this system was used with a flow cell, it is possible to adapt it to a classical 5 mm NMR tube. The advantages of such liquid-driven transfers become especially important when dealing with long distance transfers. Indeed, as explained in the previous section, a gas-driven high-speed transfer will decrease the liquid bolus length. Over longer distances, a liquid bolus rupture can occur, leading to a poor injection consisting of droplets. A liquid-driven injection avoids this problem. Figure 40 shows our transfer and injection system. The dissolution step using a dissolution stick and the injector have been presented in the previous sections. The transfer system, based on the work of Hilty et al., uses the first 10-way fast switching valve and an optical sensor to select a part of the dissolved sample in the loop capillary. A micro-annular gear pump is used to transfer the sample in the injector through a magnetic tunnel [50]. A second 10-way fast switching valve is triggered at the end of the injection to apply a backpressure to prevent degassing. A transfer time of ~ 2 s can be obtained over 9.5 m of capillary. Long distance transfer can be useful in laboratories where the spectrometer configurations cannot be changed.

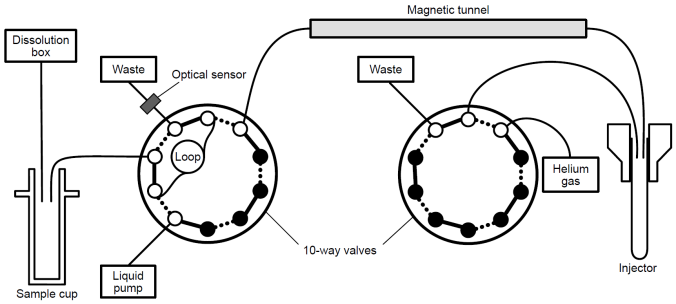

Figure 40: Schematic overview of the dissolution, transfer and injection system based on a liquid-driven system, including a dissolution box and sample cup for the dissolution step, a set of two 10-way valves, a loop and an optical sensor for the selection of the sample bolus, a liquid pump and a magnetic tunnel for transferring the selected sample bolus, and an injector with a back-pressure of helium gas for the injection.

6.4.2. Sample contamination

Liquid-driven transfers avoid any rupture with the liquid sample bolus. However, turbulences and axial diffusion can still create a mixing between the driving liquid and the dissolved hyperpolarized sample [169]–[172]. The mixing length depends on several factors, among which are the capillary dimensions, the fluid properties and the driving liquid speed. To avoid contamination and further dilution of the injected sample, one must carefully choose the parameters used for the transfer. Fortunately, as described in the literature [171], [172], when the turbulences becomes high enough, the axial dispersion decreases as well as the mixing length. Such observations have been made in our group, with no contamination observed for the faster transfer.

6.4.3. Injections with liquid-driven transfer

Injection using liquid-driven transfer can prove to be efficient, as reported by Hilty et al. [167]. Linewidths of ~1.8-4.0 Hz have been shown. Furthermore, a comparison between gas-driven injections in a 5 mm NMR tube and liquid-driven injections in a flow-cell, shown in Figure 41, indicates that liquid-driven injections have a faster stabilization time. As indicated above, liquid-driven injections into a 5 mm NMR tube should be associated with a back-pressure to avoid degassing.

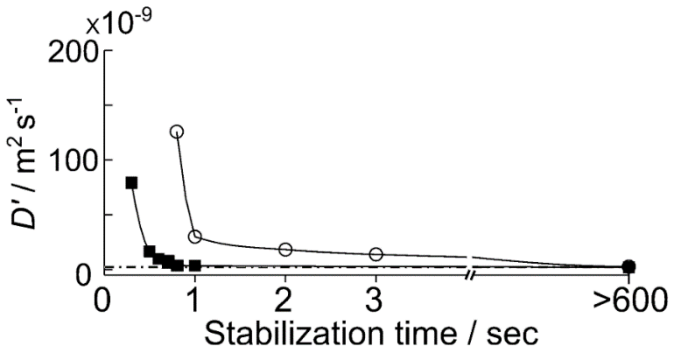

Figure 41: Diffusion coefficients of hyperpolarized samples transferred and injected using gas (white circles) or liquid (black squares) showing a faster stabilization with liquid transfer. Image adapted with permission from the work of Chen and Hilty [167].

6.5. Avoiding low-field regions during the transfer

When transferring a hyperpolarized sample from the polarizer to the acquisition device, whether an NMR spectrometer or an MRI, it is of primal importance to avoid low-field regions. Such regions will destroy the polarization, see Section 7. To maintain a magnetic field high enough to limit polarization losses, usually greater than a few milliTesla, two main approaches are used. The first is based on permanent magnets. Milani et al. [50] proposed a magnetic tunnel where the hyperpolarized solution travels through an array of permanent magnets placed in a Halbach configuration. This system can produce a field >0.9 T (see Figure 42). Other studies proposed transportable systems, used for MRI, with magnetic fields of ~0.2 T [173], [174].

Another similar approach consists in using electromagnets for transporting the hyperpolarized solution. This method can be safer especially when approaching an NMR or MRI instrument, since the electromagnet can be turned off. Shang et al. [175] proposed a handheld device producing over 5 milliTesla over the dissolution sample container. In our laboratory, when a rigid permanent structure such as a magnetic tunnel cannot be used for practical reasons, we wind a single-layer coil around the capillaries to create a 4 mT field using a 2 A power source. The single layer configuration keeps the capillary flexible, which can be useful especially while performing a manual coupling of the dissolution stick.

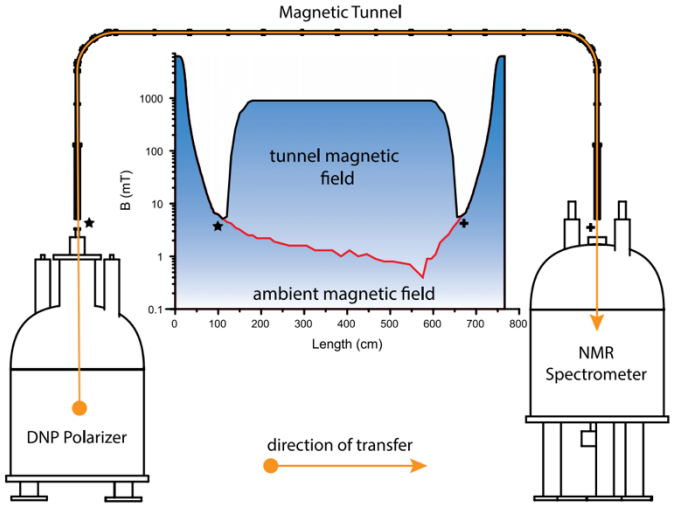

Figure 42: The magnetic field strength in the course of the transfer of the hyperpolarized fluid from an unshielded DNP polarizer to an unshielded 300 MHz NMR spectrometer through a magnetic tunnel (black line) or without tunnel (red line). The stars and crosses indicate the polarizer-tunnel and tunnel-spectrometer junctions. Adapted with permission from Milani et al. [50]**.**

7. Physics of sample dissolution

7.1. Introduction

This section aims to present the mechanisms through which nuclear spin polarization might decay during the processes of dissolution and transfer from the polarizer to the liquid-state NMR or MRI magnet. We will discuss the key relaxation mechanisms as well as the strategies that allow for prevention of some of these polarization losses.

Table 4: Steps of the dissolution and transfer process, and the corresponding sources of polarization losses. *Strongly dependent on the experimental setup.

	Step	Phase	Temperature	Field	Incoherent mechanisms	Coherent mechanisms
A	End of the DNP build-up	Solid	~1.2-4.2 K	High (3.35–7 T)	Solid-state paramagnetic relaxation	
B	Before dissolution			Moderate (1-7 T)		
C	During dissolution	Solid to liquid	Increasing (4.2→350 K)			If the solid is exposed to lower fields, nuclear thermal mixing may occur
D	Exiting the polarizer	Liquid	High (300-350 K)	Decreasing (T→mT/μT)		Non-adiabatic field decrease may create coherences
E	Transfer between the magnets		Moderate (300 K)	Low to moderate* (<mT)	Liquid-state relaxation at low to moderate fields	Rotation of the field creating coherences
F	Entering the spectrometer			Increasing		Non-adiabatic field increase the creation of coherences
G	After injection			High field	High field liquid-state relaxation	

Main functions. During the processes of dissolution and transfer, the sample goes from a solid to liquid phase. Furthermore, the spins experience a varying magnetic field, temperature, pressure and in some cases pH. Table 4 decomposes the entire process into steps from A to G and relates each step to the sources of polarization losses. The steps are illustrated on Figure 43.

A. At the end of the DNP build-up, the sample is at low temperature and high field;
B. Prior to dissolution, the sample is usually lifted by a few centimetres above the helium bath in a cold helium gas atmosphere to improve the thermodynamics of the dissolution process;
C. Upon injection of hot solvent, the temperature of the sample increases and the sample melts, in principle remaining at high field;
D. The sample is expelled from the polarizer (discussed in the previous sections), and as a result; the spins experience a rapid decrease in magnetic field. At the same time, the temperature increases;
E. The sample is transferred to the liquid-state at a temperature that is difficult to estimate and is highly dependent upon the experimental setup. The magnetic field during the transfer also depends on the experimental setup since it is a sum of contributions from the surrounding magnets and the earth. In some cases, guiding fields may be added;
F. The sample enters the liquid-state NMR magnet, and the spins experience an increase in magnetic field;
G. The sample is in the liquid-state NMR magnet at high field and is generally close to room temperature.

During each of these steps, a variety of relaxation mechanisms may cause losses of polarization [50], [176], [177]. The interactions are separated into two types: incoherent and coherent. What we call incoherent polarization loss is the return of the polarization to thermal equilibrium through relaxation, that is, longitudinal or spin-lattice relaxation. During steps A and B, the sample is in the solid-state and relaxes mainly through paramagnetic relaxation, which is described in Section 7.2. During steps D-G, the sample is in the liquid-state and may relax through a number of mechanisms. Section 7.3 presents the most usual liquid-state relaxation mechanisms for *d*DNP, namely, through dipole-dipole couplings, chemical shift anisotropy (CSA) and paramagnetic interactions. Some relaxation mechanisms are stronger at lower magnetic fields (although the difference is not always significant) and as such may be mitigated by the use of a guiding field during the sample transfer (stage E). Section 7.3 aims to account for the field dependence of the relaxation mechanisms to understand in which cases the magnetic field may have to be actively increased to preserve the nuclear spin polarization during the transfer. This is usually enacted by setting up a magnetic tunnel around the capillary through which the solution travels.

The loss of polarization through coherent mechanisms is the result of non-adiabatic field variations, either rotations or changes in intensity, which induce coherences between nuclear spin states. The latter may be avoided by using a guiding field as well as by adjusting the flow rate of the solution during sample transfer.

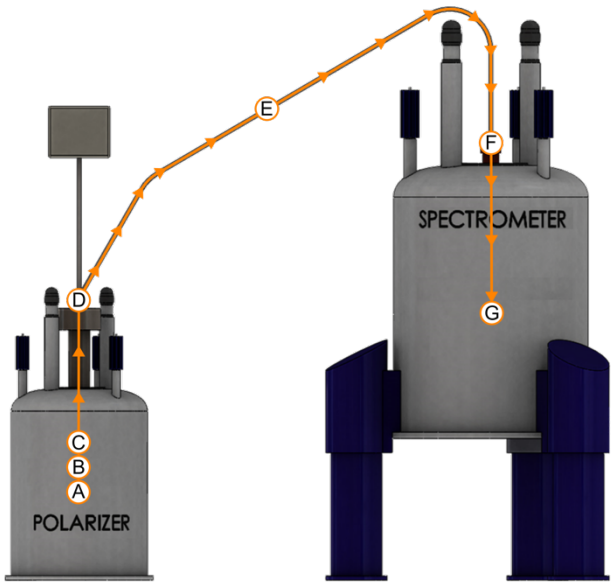

Figure 43: Schematic representation of a *d*DNP experiment and its steps as detailed in Table 4.

7.2. Generalities of relaxation theory

Relaxation theory is a large and complex topic and so the following sections only aim to cover aspects which are necessary to understand how to perform a dissolution experiment with minimal polarization losses. Hyperpolarized nuclear spins return to Boltzmann equilibrium because they are subject to random fluctuations of their Hamiltonian. These fluctuations are stochastic and depend on the physical parameters related to the experimental setup (temperature, magnetic field profile, etc.), the sample formulation, dissolution solvent (presence of radicals, dissolved oxygen, protonation level, etc.) and the properties of the hyperpolarized molecule (dipolar couplings, CSA, *J*-couplings, chemical exchange, etc). By definition, these fluctuations average to zero if we consider a single spin on a sufficiently long timescale or a sufficiently large number of spins. Intuitively, one can say that a nuclear spin may relax to thermal equilibrium whenever it experiences a magnetic field which oscillates near or at its Larmor frequency. For example, a pair of neighbouring ^{1}H spins in a molecule exert a magnetic field on each other. The intensity of this interaction depends on the orientation of the molecule. Due the rapid reorientation of the molecule in solution, this interaction averages to zero and does not influence the Larmor frequency of the spins, *i.e.,* it does not shift the resonance peak associated with these spins. Now, imagine that the molecule is rotating in space at a frequency near the Larmor frequency: the intensity of the interaction will vary in time at the Larmor frequency, which will give the opportunity for spins to relax.

It is impossible, or at least challenging, to describe this sort of interaction completely or in a deterministic manner. The common strategy is to describe them with probabilities. A key parameter is then the correlation time of the fluctuating interaction, which usually takes the symbol τ_c. Many definitions may be found for this quantity. To give a qualitative and intuitive account, we may often refer to τ_c as the average time during which the interaction causing relaxation keeps a given value. For example, in the case of solid-state paramagnetic relaxation, τ_c corresponds to the average time during which an unpaired electron remains in the α or β state (often in the microsecond to millisecond range). In the case of liquid-state intramolecular dipole-dipole relaxation, the correlation time corresponds to average time during which a molecule rotates through an angle of 1 radian (typically in the picosecond to nanosecond range). It is important to notice that relaxation theory is usually more concerned by the order of magnitude of the correlation time than by its precise value. As we go through the relaxation mechanisms that are important to *d*DNP in the following sections, we will mention the interactions on which each mechanism relies and the timescales on which such interactions oscillate [178]–[183].

7.3. Solid-state relaxation

Under *d*DNP conditions, the main source of solid-state polarization losses is paramagnetic relaxation, which we intend to briefly summarize. The unpaired electron of a paramagnetic agent and the nuclear spins in the sample interact through dipolar interactions (also referred to as a hyperfine or super hyperfine interactions). Since the spin state of the electron fluctuates, the nearby nuclear spins experience a randomly varying magnetic field which causes them to relax. The relaxation of these nuclear spins is then spread throughout the sample via nuclear flip-flops (nucleus-nucleus dipolar interactions). Macroscopically, this process is referred to as "spin diffusion". The paramagnetic centers and their surrounding nuclear spins thus act as relaxation sinks which affect nuclear spins even if the nuclear spins themselves do not interact directly with an electron spin. This two-step mechanism was first proposed by Bloembergen in 1949 [184] and was followed by a vast literature in the 60s and 70s. Ramanathan's review on spin diffusion in 2008 [185] provides an overview of the field. Relevant treatments of relaxation mechanisms can be found in Section 8.7 and 8.9 of a review on paramagnetic NMR [186], or in the recent literature on low temperature static DNP [16], [187]–[189]. Two key parameters dictate the efficiency of this relaxation mechanism:

1) The temperature influences the correlation time of the electronic spin state and hence the intensity of direct paramagnetic relaxation. The higher the temperature, the shorter the correlation time. In the limit where the correlation time is small with respect to the nuclear Larmor period, the nuclear spin relaxation rate constant becomes proportional to the correlation time.

2) The rate at which polarization may diffuse depends on the strength of the dipolar interactions between nuclear spins [190]. We will not go into the details of this dependence here, but we note that lower-gamma nuclear spins experience weaker spin diffusion and are less susceptible to indirect paramagnetic relaxation. In addition, more dilute nuclear spins have larger average internuclear distances and thus weaker dipolar interactions, and hence also weaker spin diffusion. As a consequence, diminishing the concentration of the nuclear spins of interest also diminishes the effect of paramagnetic relaxation. It should be noted that minimizing spin diffusion, if mitigating paramagnetic relaxation, can also result in hindering the efficiency of DNP.

We now move to the practical implications of paramagnetic relaxation for the dissolution experiment itself. Once the sample is hyperpolarized and ready for the dissolution and transfer steps, most experimental *d*DNP setups require the sample space to be pressurized above atmospheric pressure and the sample to be lifted outside of the liquid helium bath to prevent the dissolution solvent from freezing upon arrival at the sample cup. During this time, the sample is no longer being irradiated by the microwave source and is thus subjected to relaxation without being repolarized by DNP. In the case of ^{13}C DNP, the nuclear longitudinal relaxation time constant T_1 in standard DNP juice remains on the order of hours, provided the temperature does not increase significantly above that of liquid helium temperature (ca. 4.2 K) and the magnetic field does not significantly drop below (ca. 1.0 T). In the case of ^{1}H DNP, the relaxation time constant is in the order of minutes so the rapidity at which the dissolution is performed starts to play an important role in preserving the previously accrued nuclear polarization. The different behaviour of ^{13}C and ^{1}H nuclear spins is an illustration of the principles presented previously. Indeed, the larger gyromagnetic ratio typically engenders shorter relaxation time constants. In addition, ^{1}H not only has a high gyromagnetic ratio but is usually present at concentrations higher than those of ^{13}C spins, which engenders faster nuclear spin diffusion and ultimately faster paramagnetic relaxation. Another important parameter is the paramagnetic agent concentration. At higher concentrations, the correlation time of the electron decreases due to stronger electron-electron dipolar couplings and the

average distance between the paramagnetic agents and nuclear spins also decreases. Both factors account for stronger nuclear spin-lattice relaxation.

A critical moment of the dissolution process occurs when the dissolution stick comes into contact with the sample. At this point, the room temperature dissolution stick brings a significant heat load causing the temperature of the sample to raise rapidly, which dramatically shortens the electron correlation time and hence the nuclear longitudinal relaxation time constant. To avoid detrimental polarization losses, the sample should be dissolved as rapidly as possible. This implies that the dissolution solvent should be injected immediately after coupling the dissolution stick to the sample. This point is as critical as the rapidity of the dissolution process itself. Furthermore, the dissolution solvent heats the sample before it can melt and be dissolved into solution. During this time, the sample is warming up towards the melting point but is still solid, and therefore not yet diluted and with a high polarizing agent concentration. Therefore, paramagnetic relaxation can become very efficient, especially for high-gamma nuclear spins. This is therefore important for the dissolution process which much be carefully optimized. See Section 6 for more information. Although there are no detailed studies on this question, one can expect that a lower radical concentration in the DNP sample will cause lower polarization losses through the mechanism described above.

In addition to paramagnetic relaxation, nuclear thermal mixing in regions of low magnetic field should be avoided to prevent polarization losses. At low magnetic field (typically in the mT field range), the difference in Zeeman energies between heteronuclear spins might be compensated by the dipolar interaction allowing for the direct transfer of polarization [5], for example between ^{1}H and ^{13}C nuclear spins. All nuclear spins connected via thermal mixing relax together, and thus act as relaxation sinks for each other. This effect is only present in the solid-state, where the dipolar interaction is not averaged. This relaxation mechanism is avoided by performing the dissolution step in a region of sufficiently high magnetic field. However, in the case where the sample would escape the sample space as a suspension of partially melted particles, nuclear thermal mixing can be expected to cause significant polarization losses. Therefore, one has to set up dissolution parameters so as to ensure that the sample leaves the high magnetic field once entirely melted and dissolved.

7.4. Liquid-state relaxation

In this section, we will list the main relaxation mechanisms which operate in the liquid-state (during steps D-G of the *d*DNP experiment, see Table 4), with a particular attention to the magnetic field dependence of each interaction. Understanding the magnetic field dependence allows the experimentalist to choose an appropriate strategy for the sample transfer step. It will be shown that, in some cases, adding a magnetic tunnel between the polarizer and liquid-state NMR spectrometer so that the solution experiences a non-vanishing field during the transfer can help to sustain polarization. Section 6.4 reviews some practical solutions.

Providing a full description of each relaxation mechanism is beyond the scope of this review but the reader will be referred to the appropriate literature. Table 5 summarizes the physical parameters which govern the relaxation dynamics of each mechanism, in particular their field dependence; an overview of the relaxation rates of ^{13}C spins in bio-relevant molecules is given elsewhere [28]. The theory underlying liquid-state relaxation is available can be found in several texts [178]–[181], [191], [192].

Dipole-dipole couplings. Nuclear spins interact through space via an interaction known as the dipole-dipole (DD) coupling. In the solid-state, this interaction leads to distinctive spectral patterns [193]. In the liquid-state, this interaction does not lead to any observable spectral features since it is averaged to zero (apart from line broadening through relaxation). Nonetheless, the random motion of molecules in solution (orientational tumbling) causes rapid variations of this interaction and engenders nuclear relaxation. In the case of intramolecular DD relaxation, two (or more) nearby nuclear spins experience a fluctuating magnetic field due to the rotation of the molecule in solution, and hence the variation of the DD interaction with respect to the static magnetic field. The time constant which governs this interaction is the rotational correlation time of the molecule which is on the order of tens or hundreds of picoseconds for small molecules in water at room temperature [194]. DD relaxation rates are proportional to the square of the dipole interaction between nuclei, which is proportional to the inverse cube of the distance between the spins. DD relaxation rates are thus proportional to the inverse sixth power of the distance between spins and so it is most effective for very close nuclei. For example, DD relaxation is efficient for geminal ^{1}H spins in amino acids or peptides [195] or ^{13}C spins with adjacent ^{1}H nuclear spins, such as in a ^{13}C-formate anion $HCOO^{-}$. In the case of non-rigid molecules, extra degrees of freedom add to the effects of rotational diffusion. Methyl groups are a common example of this process. The rapid rotation of the three ^{1}H spins in ^{13}C-methyl groups shortens the relaxation time of the ^{13}C spin via the intramolecular DD interactions, although rotation of the methyl group itself attenuates those couplings.

Most *d*DNP experiments aim at polarizing small molecules which have sub-nanosecond rotational correlation times that are short compared to the Larmor period of nuclear spins even at high magnetic fields. This limit, known as extreme narrowing, implies that the DD relaxation rate is magnetic field-independent and proportional to the overall correlation time of the molecule in solution. As a consequence, if the principal source of signal attenuation during the sample transfer step is DD relaxation, adding a magnetic tunnel to sustain a higher magnetic field, see Section 6.5, is not expected to bring any improvement. On the contrary, increasing the temperature ensures longer relaxation times since it decreases the rotational correlation time, except in unusual circumstances.

DD relaxation may also occur between molecules, *i.e.,* intermolecular DD relaxation. In this case, translational diffusion of molecules leads to nuclear relaxation. For example, the rapid diffusion of ^{1}H nuclear spins in water may relax spins on nearby molecules. This is the reason why deuterated solvents are preferred as solvents for dissolution. For the case of water hyperpolarized by *d*DNP, this mechanism is the main source of polarization losses, apart from those caused by traces of paramagnetic species remaining in solution. In this case, raising the temperature of the solution during the transfer step was shown to greatly increase the hyperpolarization lifetime of water during the transfer [196].

Chemical shift anisotropy. The induced magnetic field in the electron cloud around the nucleus shifts the nuclear Larmor frequency in a predictable manner. The isotropic part of this shift, which corresponds to the average of the shift over time or molecular orientation, leads to the isotropic chemical shift that

is observed in liquid-state NMR experiments. The anisotropic part of the chemical shift tensor, named chemical shift anisotropy (CSA), leads to distinctive patterns in solid-state NMR spectra. As a molecule tumbles in solution, the CSA tensors reorient, leading to a time dependent variation of the chemical shift. Although this variation averages to zero, it may still cause relaxation, as in the case of the DD relaxation mechanism. Since CSA depends on the tumbling of the molecule, it also depends on a reorientational correlation time, in a fashion similar to DD relaxation. The strengths of both the symmetric and antisymmetric CSA interactions are proportional to the strength of the static magnetic field B_0. It follows that the CSA relaxation rate is proportional to the square of the static magnetic field, in contrast to DD relaxation. Since CSA relaxation results from the shielding of a nuclear spin by the electron cloud, it does not require the participation of a second nuclear spin.

In the case of ^{1}H spins, the CSA is often weak and thus rarely provides an efficient relaxation pathway. On the contrary, ^{13}C spins may experience large CSAs, especially for the case of carbonyl groups [197]. This example is important for *d*DNP as many experiments are performed on [1-^{13}C]-pyruvic acid, [1-^{13}C]-acetic acid and other molecular derivatives which are labelled at the carbonyl position. At high magnetic fields, CSA might therefore provide an efficient relaxation pathway for these molecules. As the intensity of the interaction increases with the magnetic field, using a magnetic tunnel during the sample transfer step is of no help in mitigating this source of nuclear relaxation. Nonetheless, the typical field strength of magnetic tunnels constructed using a Halbach array of permanent magnets is at best about ~1 T [50] where CSA relaxation is weak for most molecules. Consequently, the use of a magnetic tunnel might diminish some polarization losses but is not expected to significantly increase relaxation from CSA.

Liquid-state paramagnetic interactions. The strong magnetic moment of unpaired electrons of paramagnetic agents provides an efficient relaxation source in the liquid-state. This relaxation mechanism is important for *d*DNP as all polarizing agents are paramagnetic. Furthermore, solutions naturally contain dissolved dioxygen which is also paramagnetic.

As solutes diffuse in solution, their distance from paramagnetic agents fluctuates, which modulates the magnetic field experienced by the nuclei of the solutes, causing nuclear relaxation which occurs when the random field variation matches the Larmor frequency of the nuclear spins (or other frequencies corresponding to zero and double quantum transitions of the electron-nucleus spins system). It follows that the rate at which the solute diffuses near the paramagnetic centre determines the efficiency of the relaxation mechanism. Hence, the diffusion coefficient of the solute usually governs the paramagnetic relaxation rate [198].

There is an intricate dependence of the paramagnetic relaxation rate constant on the diffusion coefficient and the magnetic field. As a rule of thumb, increasing the temperature (diminishing the viscosity) decreases the paramagnetic relaxation rate [198]. In common cases, for a given temperature and solvent viscosity, the relaxation rate increases at lower magnetic field and plateaus below a certain value, as shown on Figure 44 [49], [177], [198]. The magnetic field strength below which paramagnetic relaxation usually becomes efficient is on the order of 0.1 to 1.0 T [49], [177]. In other words, paramagnetic relaxation is usually efficient, *i.e.,* detrimental, in the mT regime while it is weak, *i.e.* safe, in the Tesla regime. In a common laboratory, as the solution travels between the *polarizer* and the liquid-state spectrometer, it experiences magnetic fields of a few mT and sometimes lower, especially if the NMR magnets are shielded or far apart. This means that paramagnetic relaxation might be detrimental during the transfer of the hyperpolarized solution. A magnetic tunnel may therefore be employed to sustain the magnetic field during the transfer. Magnetic tunnels using Halbach arrays of four permanent magnets can readily produce guiding fields up to ~1 T and have proved to greatly improve the final liquid-state polarization in certain cases [50]. Indeed, it can increase the relaxation time of certain molecules by factors up to 3 or 4 [49], [50], [177].

Table 5: Summary of the main relaxation sources for small molecules in solution. The symbols τ_c, T, η and B_0 stand for the rotational correlation time, temperature, viscosity of the liquid and magnetic field, respectively. The symbols γ_I, γ_S, and r_{IS} stand for the gyromagnetic ratios of spins I and S and the distance between them, respectively, which governs the size of the dipole-dipole coupling constant D_{00}. δ^{aniso} is the chemical shift anisotropy parameter. In the context of intermolecular DD relaxation, C is the concentration of a spin bearing molecule causing a species to relax. In the context of paramagnetic ("para") relaxation, $C_{radical}$ is the radical concentration. Finally, $J(\omega,\tau_c) = \tau_c/(1+\tau_c^2\omega^2)$ is the spectral density function.

	Relevant parameters	Field dependence	
DD	τ_c (T, η) B_0 $D_{00} \propto (\gamma_I^2, \gamma_S^2, r_{IS}^{-3})$ C (intermolecular DD)	General:	$J((\gamma_I-\gamma_S)B_0, \tau_c)$ $J((\gamma_I+\gamma_S)B_0, \tau_c)$ $J(\gamma_I B_0, \tau_c)$
		Extreme narrowing:	$J \approx \tau_c$, no field dependence
CSA	τ_c (T, η) B_0^2 δ^{aniso}	General:	$B_0^2 J(\gamma_I B_0, \tau_c)$
		Extreme narrowing:	$\tau_c B_0^2$
Para	η $C_{radical}$	$C_{radical}$ Usually higher at lower fields	

Adding a magnetic tunnel mitigates the losses due to paramagnetic relaxation but does not completely suppress them. Complementary strategies consist in reducing the radical concentration in solution. The first obvious way is to use lower radical concentrations in DNP samples. For ^{1}H DNP, TEMPOL is an efficient polarizing agent for typical concentrations up to 50 mM. The dissolution process dilutes the sample by a typical factor 50, so that the TEMPOL concentration drops to ~1 mM in the liquid-state. A concentration of 25 mM TEMPOL in the DNP sample reaches nearly the same DNP performance as 50 mM TEMPOL [40] but will lead to a concentration of only ~0.5 mM in the liquid-state. The liquid-state paramagnetic relaxation rate constant is proportional to the radical concentration [199]. Diminishing the radical concentration in the liquid-state by a known factor reduces paramagnetic relaxation by the same amount. It is therefore often preferable to use a TEMPOL concentration of 25 mM when performing *d*DNP experiments. The concentration of TEMPOL in solution can be further reduced by quenching the radicals at the moment of dissolution with sodium ascorbate (vitamin C). [51] Sodium ascorbate may either be added to the dissolution solvent at a concentration of typically >10 mM or in pellets mixed with the sample in the sample holder in higher concentration, typically >1 M. In either case, sodium ascorbate must be in large excess with respect to TEMPOL immediately after dissolution so that the reaction is fast and consumes most of the TEMPOL.

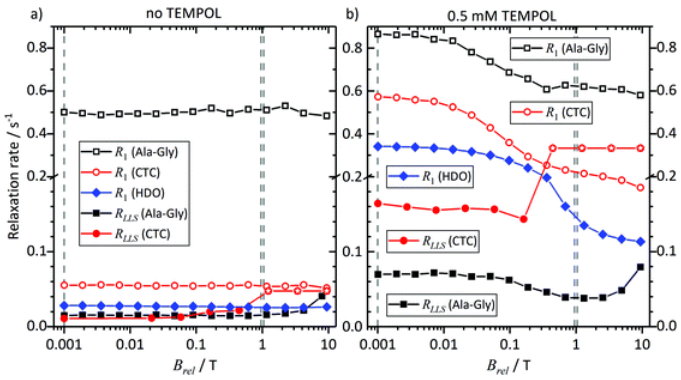

Figure 44: a) ^{1}H relaxometry measurements for several molecules in D_2O without and with 0.5 mT TEMPOL in liquid-state at room temperature in a field of 1 mT to 10 T. b) Relaxation rates as a function of the magnetic field. CTC stands for 3-chlorothiphene-2-carboxylate. Adapted with permission from [177].

More sophisticated strategies consist of covalently attaching radical molecules to materials that are filtered out after the dissolution step, producing a radical-free solution, without relying on any chemical reaction [41], [42], [44], [200]. In the case of hybrid polarizing solids (HYPSOs), the radical molecules are grafted onto the surface of a porous silica matrix and the solution of interest is impregnated in the pores of the material [42], [44], [200]. Similarly, hyperpolarizing porous polymers (HYPOPs) are epoxide-based porous polymers where the radical is incorporated within the polymer walls [77]. In the case of filterable labelled agents for polarization (FLAP), the radical molecules are attached to an organic polymer which precipitates at high ionic strength. [41] The solution of interest is impregnated in the polymer powder. The dissolution is performed with a sodium chloride solution which ensures that the polymer precipitates and can be filtered out before the transfer. Alternatively, non-persistent radicals such as UV-induced radicals are another promising strategy [147]. These *in situ*-generated radicals efficiently polarize the ^{1}H spins but recombine at ~100 K, therefore producing radical-free hyperpolarized solutions.

The strategies above were developed for ^{1}H using radicals with broad EPR lines to produce hyperpolarized ^{1}H or ^{13}C using cross polarization. In the case of direct hyperpolarization of ^{13}C using narrow line radicals such as trityls, the radical can also be filtered out after precipitation by an acidic dissolution solvent [150].

Other relaxation mechanisms. The liquid-state relaxation mechanisms listed above are those which are most effective and common during the sample transfer stage of a typical *d*DNP experiment. The relevant parameters for each of the aforementioned relaxation mechanisms can be found in Table 5. Yet, there are a number of other mechanisms that may be encountered and cause further relaxation losses in *d*DNP experiments. Such mechanisms are not detailed in this review, but references are given in some cases:

(i) ***Chemical exchange*** may cause relaxation when the exchange induces a change in chemical shift and occurs on the timescale of the nuclear Larmor frequency of the spins of interest. In some cases, chemical exchange depends on pH and therefore the relaxation rate constant itself also depends on pH [201].

(ii) ***Scalar relaxation of the second kind*** (SR2K) is a mechanism whereby a nuclear spin relaxes on a timescale that matches the nuclear Larmor frequency of a *J*-coupled neighbour, therefore causing it to relax. At high field, nuclei causing SR2K often have very short values of nuclear T_1. Common cases often involve quadrupolar nuclei [202]. At low fields, nuclei such as ^{14}N can also cause relaxation by SR2K [173] [191].

(iii) **Spin rotation** is a mechanism whereby nuclear spin states couple to rotational states engendering relaxation [203], [204]. A common case where such as relaxation mechanism occurs is in rapidly rotating methyl groups [205]–[207].

7.5. Coherent losses of polarization

During a *d*DNP experiment, the hyperpolarized solution travels from one magnet, the polarizer, to another, the liquid-state spectrometer. As the solution leaves the polarizer, it experiences a stray field with decreasing intensity. Conversely, as the sample enters the liquid-state spectrometer, it experiences its increasing stray field. How do the spins react to this field decrease and increase? Furthermore, what happens in the middle where the field might go to very low values or possibly vanish completely. This section aims at answering these two questions. In some cases, a rapid variation of the intensity or of direction of the field experienced by the nuclear spins during the transfer can excite coherence between NMR transitions. The portion of hyperpolarization that is turned into coherence rapidly dephases and is lost. We refer to these sorts of losses as "coherent" because they are the result of a deterministic process. No stochastic or random interactions are involved.

The ideal scenario for *d*DNP experiments is that the polarizer and the liquid-state spectrometer have non-shielded magnets with opposite polarity [50]. Indeed, non-shielded magnets have strong stray fields and, when the polarity of the magnets is opposite, their stray fields add up in the space between them. Such a situation typically ensures a minimal magnetic field on the order of mT along the transfer, with the direction of the field experienced by the spins changing smoothly from the polarizer to the liquid-state spectrometer. On the contrary, shielded magnets have rapidly decaying stray fields, which will cause fast variations of the field experienced by the nuclei during transfer. Furthermore, when the polarity of the two magnets is the same, their stray fields may cancel out at some point along the transfer pathway. In such cases, the use of a magnetic tunnel might be essential to preserve the polarization during the transfer.

Creation of coherences by rotation of the magnetic field. Let us consider a single spin subject to a magnetic field. Let us now assume that this magnetic field has a fixed intensity but is rotating in space around an axis. We assume that, at time $t = 0$, the spin is aligned with the magnetic field. If the rotation of the field is infinitely slow, the spin always remains aligned with the magnetic field. Such a transformation is said to be "adiabatic". In the opposite limit, if the direction of the field jumps infinitely fast by an angle, say $\pi/2$, the spin effectively experiences a sudden change of its Hamiltonian. This kind of transformation is said to be "non-adiabatic" or sudden [208]. Its state is now the superposition of two eigenstates in the basis of the new Hamiltonian. In other words, the spin is no longer in a stationary state: the instantaneous rotation has turned the population difference into a coherence. Whether the rotation may be considered as slow or fast is determined by the Larmor frequency of the spin. If the field rotates at a frequency that is slow with respect to the Larmor frequency, the spin is able to adapt and remains in an eigenstate of the Hamiltonian.

For example, during a *d*DNP experiment, a ^{13}C spin travels at 5 ms^{-1} from a polarizer to a liquid-state spectrometer with

opposite polarities separated by 5 m (transfer in 1 s). The field experienced by the spin goes from $-z$ to $+z$ (or conversely) which corresponds to a π rotation. We assume for simplicity that the rotation has a constant frequency. The field thus rotates at a frequency of 0.5 Hz. The gyromagnetic ratio of ^{13}C is 10.7 $MHzT^{-1}$. If the minimal field experienced by the spin is 1 mT during the transfer, its minimal Larmor frequency will be of 10.7 kHz. This is far above the frequency of the field rotation so the transfer will surely be adiabatic and will not cause any loss of polarization. If the magnetic field goes as low at 1 μT, however, the Larmor frequency of the ^{13}C spin will be 10.7 Hz. This is still factor 20 higher than the frequency of the magnetic field rotation but is not as safe.

This simple reasoning allows one to develop an intuition for situations where the magnetic field rotation may not be adiabatic, and therefore induce the creation of coherences and consequent polarization losses. The risk of polarization losses may be assessed quantitatively, provided the precise field profile experienced by the spins during the transfer is known. Derived from Bloch's equations, the considerations above can be formalized by defining an adiabaticity parameter based on the comparison of the field rotation frequency with the Larmor frequency [50], [176], [208]:

$$\frac{1}{B^2}\left|\vec{B}\times\frac{\mathrm{d}\vec{B}}{\mathrm{d}t}\right| \ll \gamma B \quad (14)$$

where B and γ are the magnetic field and the gyromagnetic ratio of the spins, respectively. The adiabaticity parameter may then be defined as:

$$A = \left|\vec{B}\times\frac{\mathrm{d}\vec{B}}{\mathrm{d}t}\right|\frac{1}{\gamma B^3} \quad (15)$$

The transfer is adiabatic when A is small compared to 1.

Such calculations might be important when shielded spectrometers are used. When the solution enters the stray field of the magnet, the direction of the field varies rapidly. In the case of a shielded magnet, this occurs at a lower magnetic field than for a non-shielded magnet. Equation 15 also shows that although going through a region of zero field or worse, going through a field inversion may cause polarization losses. Indeed, when the magnetic field becomes vanishingly small, the denominator of the adiabaticity parameter goes to zero causing the parameter A to become infinite. In this situation, any variation of the field direction may induce coherences. The use of a magnetic tunnel is then crucial to maintain the polarization during the transfer [50]. Equations 14 and 15 are derived from Bloch's equations [208], and so only apply for an isolated single spin. Coupled spins may behave similarly in many cases but in special circumstances, one might have to take more effects into account by using a quantum mechanical description of the transfer. Such cases are illustrated in the next section.

Section 6.4 reviews some practical solutions to increase the magnetic field between the polarizer and the liquid-state spectrometer. Such strategies may prevent coherent polarization losses.

Creation of coherences by a variation of intensity of the magnetic field. For a single isolated spin, a change in the magnetic field intensity affects the Larmor frequency of the spin but does not mix its eigenstates. As a consequence, no matter how fast the variation of the magnetic field intensity is, it cannot induce coherences. On the other hand, pairs of J-coupled spins have different eigenstates depending on the magnetic field strength. There is a critical magnetic field where the difference in Zeeman energies matches the J-coupling. When the magnetic field is far above this critical value, the spins can be considered to be in the Zeeman basis. When it is far below, the spins can be considered to be in the singlet-triplet basis [209]. The effect of transport through low fields on the lineshape of NMR spectra in the liquid-state has already been documented for the case where the spins enter the strong coupling regime adiabatically, *i.e.,* when the field decreases slowly enough to preserve populations without creating any coherences [177]. If the field drops or increases rapidly near the critical field value, it may induce coherences and therefore cause polarization losses. The critical field value at which the transition between the two regimes occurs strongly depends on the spin system. For heteronuclear spin systems, this may occur in the μT regime, which is well known and exploited in the field of zero- to ultra-low field NMR (ZULF). [210] For homonuclear spin pairs, the critical point can occur at a magnetic field that depends on the strength of the J-coupling and the chemical shift difference between the two spins of interest [177]. Although this has not been reported yet, one may expect that the spin dynamics at low field may induce polarization losses by creating coherences in certain spin systems. This may occur at any point where the field intensity varies strongly. This could be when the solution leaves the polarizer, when in enters or leaves a magnetic tunnel, when it enters the liquid-state spectrometer or when it travels through an undesired field inversion. The phenomena that we foresee here as pitfalls for maintaining polarization are in fact deliberately encountered by those using parahydrogen hyperpolarization [211] and level anti-crossings (LACs) to transfer polarization [212], [213].

8. Hyperpolarized liquid-state NMR

One of the challenges of *d*DNP is that the detection in the liquid-state is an experiment in which the hyperpolarization is only possible once, after a long preparation in the solid-state. This section aims at guiding the operator through the choice of parameters for the liquid-state detection. We will then present two methods for the quantification of the liquid-state polarization which is a key result of all *d*DNP experiments.

8.1. Parameters for liquid-state detection

Virtually all conventional NMR experiments can be applied to samples hyperpolarized by *d*DNP. However, since the polarization and signal decay with time, one has to adapt the *rf*-pulse sequences and experimental schemes. As an example, 2D experiments may be performed on a *d*DNP hyperpolarized sample, provided one uses ultrafast (UF) versions of the *rf*-pulse sequences. In this section, we will detail how to set the parameters for a series of 1D acquisitions with small nutation angle *rf*-pulses and separated by a constant delay. This type of state detection, referred to as pseudo-2D, is the simplest and most common in *d*DNP and is illustrated in Figure 8a. Since each acquisition only costs a fraction of the magnetization, the evolution of the hyperpolarized spins can be monitored as a function of time. As simple as this detection scheme can be, it may give access to information on the longitudinal relaxation of the hyperpolarized spins, chemical exchange, chemical reaction and the stability of the injection process.

Due to the transient nature of hyperpolarized magnetization, one cannot shim the magnet, tune the probe and choose the acquisition parameters after the injection of the hyperpolarized sample in the liquid-state spectrometer. By the time these procedures would be finished, the polarization would have largely decayed. Therefore, one must prepare the liquid-state spectrometer for the acquisition on a different sample. An efficient strategy consists in performing a "blank" dissolution experiment, that is, to perform the dissolution and injection procedure on a sample that was not hyperpolarized but with the same experimental parameters and sample as the actual *d*DNP experiment, in order to obtain a sample in the liquid-state with the same composition and physical properties as the one that will result of the true *d*DNP experiment. This blank sample may be used to shim the magnet and tune the *rf*-probe. The final concentration of solutes in the liquid-state is usually on the order of 10 mM or less. Performing a nutation experiment with such low concentrations might not always be straightforward for low-gamma nuclei. In this case, one might have to increase the concentration of the solute so as to be able to perform nutation experiments. One must make sure that the change in concentration does not change the nutation parameters, especially if the solute is a salt.

The magnetic field used for liquid-state detection plays an important role here: higher magnetic fields of course imply improved sensitivity which is useful both for reference experiments at thermal equilibrium and to gain extra sensitivity in the actual *d*DNP experiment. On the other hand, the higher the magnetic field, the more shimming is required, and the *rf*-probe tuning is sensitive to subtle changes in the sample composition, filling of the NMR tube and physical parameters such as susceptibility and temperature. Such parameters may not be perfectly repeatable from one *d*DNP experiment to the next, which may affect the magnet shimming and *rf*-probe tuning at higher fields.

Since the intensity of NMR signals obtained by *d*DNP is large, care must be taken not to saturate the receiver. Furthermore, one usually does not want to use the entire polarization of the sample in a single acquisition. A natural choice is then to detect the hyperpolarized signal using a series of small angle *rf*-pulses separated by a delay. Ideally, one would first estimate the expected signal intensity so as to set the detection parameters rationally. Using the blank sample described above, one can determine the signal integral per mol.L^{-1} of solute for a single scan with a gain of 1:

$$S_{n,m} = \frac{S}{NS \cdot RG \cdot C} \quad (16)$$

where $S_{n,m}$, NS, RG and C are the normalized molar signal, the number of scans, the receiver gain and the concentration of the solute, respectively. Based on the expected DNP enhancement and expected final concentration, one can estimate the signal integral that will be measured when performing the hyperpolarized experiment:

$$S^{DNP} \approx \epsilon \cdot S_{n,m} \cdot C^{DNP} \cdot RG^{DNP} \cdot \sin\theta^{DNP} \quad (17)$$

where S^{DNP}, ϵ, C^{DNP}, RG^{DNP} and θ^{DNP} are the estimated signal integral, the expected DNP enhancement, the expected solute concentration, the receiver gain and the pulse angle, respectively. With this in mind, one can set the gain and the *rf*-pulse angle so that the resulting signal remains below the saturation limit of the receiver. A common choice is to use 5° *rf*-pulses with a gain between 4 and 16, provided the signal does not saturate the receiver.

One also ought to choose the delay between acquisitions. Three considerations dictate this choice: the *rf*-pulse angle, the T_2^* of the hyperpolarized solutes and the timescale of the process being studied. If P_0^{DNP} is the polarization of the solute just after injection, the remaining polarization after the i^{th} signal acquisition is given by (in analogy with Equation 8):

$$P_{i+1} = P_0^{DNP}(\cos\theta^{DNP})^i \quad (18)$$

The larger the *rf*-pulse angle, the more polarization each acquisition takes from the hyperpolarized solute. For example, applying 100 *rf*-pulses with an angle of 5° leaves 68% of the initial polarization. If the operator wishes to observe the decay of hyperpolarization during 100 s and chooses to separate each acquisition by 1 s, at the end of the detection a non-negligible portion of the signal decay (~32%) will be due to the application of the *rf*-pulses. Whether this is acceptable or not all depends on the aim of the experiment. How to account for the effect of the pulses in the data analysis is discussed in the next section. The time between each acquisition also limits the acquisition time, *i.e.,* the time during which the free induction decay (FID) may be recorded. If the acquisition time is longer than 5 times the T_2^* of each hyperpolarized solute the FID will be truncated, and the Fourier transformed signals will be distorted. Finally, whether the aim of the *d*DNP experiment is to monitor chemical reactions or to study relaxation, among other applications, the time between acquisitions will be crucial to appropriately capture the dynamics under scrutiny. Figure 45b-c shows an example of hyperpolarized decay recorded using a pseudo-2D experiment.

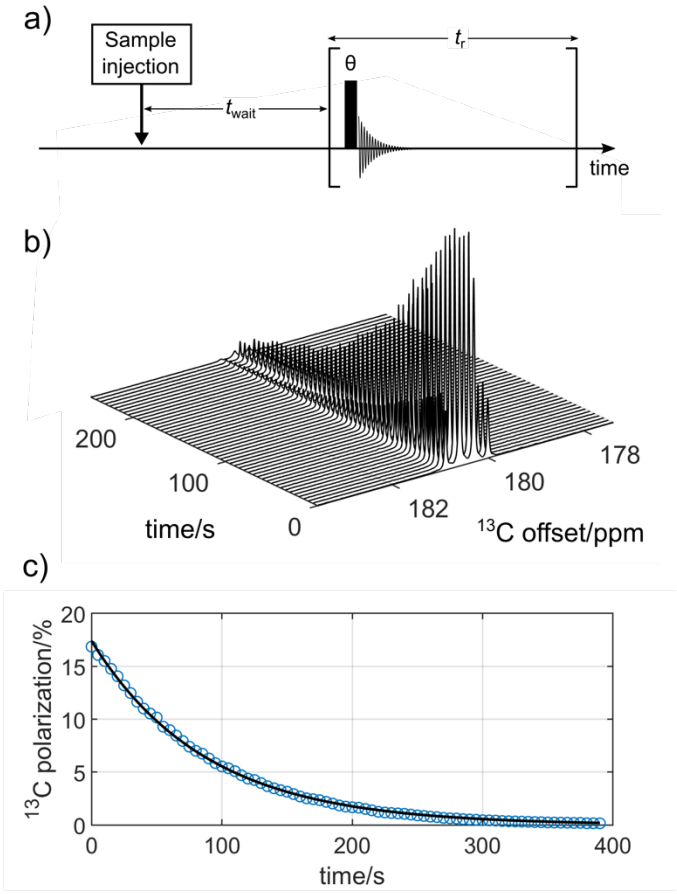

Figure 45: a) Pulse sequence for the detection of hyperpolarized species in liquids. The symbols t_{wait} and t_r stand for the waiting delay and repetition time, respectively. b) Typical decay of the hyperpolarized quadruplet of [1-^{13}C] sodium acetate recorded at 1.88 T (^{13}C nuclear Larmor frequency = 20.13 MHz) and 298.15 K acquired using *rf*-pulses with a 5° angle without ^{1}H decoupling with a repetition time of 5 s and a waiting delay of 8 s. c) Decay of the signal integral (blue circles) fitted with Equation 29.

What we have described here corresponds to the most basic liquid-state NMR experiments that can be performed in combination with *d*DNP, and already permits a number of applications such as monitoring of chemical reactions in the context of organic chemistry [214]–[217], enzymology [218], drug screening [110], [219]–[221], and other biological assays [222].

There are a number of more advanced *rf*-pulse sequences used in *d*DNP experiments. We will list some of them without going into the details. In particular, it is possible to 2D experiments or even 3D experiments. A straightforward approach consists of acquiring a series of spectra sequentially, exciting only a fraction of the magnetization for each spectrum [223]. This allowed for the acquisition of hyperpolarized HMQC and HSQC spectra with *d*DNP. More versatile is the use of ultrafast (UF)-2D NMR which is based on spatial encoding with pulsed field gradients [224]–[226]. UF-2D NMR allows for the acquisition of 2D spectra in a single scan and is compatible with *d*DNP hyperpolarization [224], [227]. UF-2D NMR has successfully been used for HSQC, HMQC [227]–[229] and HMBC [137] experiments as well as for obtaining 2D diffusion-T_2 correlation maps (Laplace NMR) [230], [231] diffusion ordered spectroscopy (DOSY) or diffusion-chemical shift correlation shift maps [232], and COSY.[233] The band-Selective Optimized Flip-Angle Short-Transient heteronuclear multiple quantum coherence (SO-FAST-HMQC) methodology [234] has also been used together with *d*DNP to study protein dynamics. [235]–[237]. In some particular molecular systems, hyperpolarization lifetimes (or coherences) can be extended by the use of long-lived states (and coherences) and used for specific application such as drug screening. [238]–[242] These applications are presented in a number of reviews on hyperpolarized NMR spectroscopy [21], [220], [226].

Finally, probably the main driving force for the development of *d*DNP has been its application to *in vivo* imaging [243]. Hyperpolarized metabolites such as [1-^{13}C]pyruvate are used for the monitoring of real-time metabolism in three spatial dimensions [244], which allows for the detection of early-stage prostate tumours [245] in humans [30], [246], [247]. Other *in vivo* applications include the imaging of pH using ^{13}C-bicarbonate [248] and angiography using hyperpolarized water [249]–[251].

8.2. Polarization quantification

Quantifying the polarization in the liquid-state is of major importance to assess the success of *d*DNP procedures. However, it can often be difficult and lengthy. In this section, two methods for the quantification of the polarization will be presented and compared. The first is conceptually the most straightforward and consists in comparing the integral between the hyperpolarized and thermal equilibrium signals. The second is named Spin PolarimetrY (SPY) and consists of inferring the polarization of a nucleus of interest from the asymmetry of the multiplet pattern of a *J*-coupled neighbouring spin (the spy). We will also show how to analyse the polarization decay in the liquid-state and extract relaxation information while accounting for the effects of the rf-pulses, in some simple cases.

Note that we prefer to express *d*DNP results in terms of polarization rather than in terms of enhancement factors. This choice was made purposefully since enhancements depend on the field at which the liquid-state detection is performed. For example, injecting a sample with a ^{13}C polarization of 20% represents enhancements of 24'700 and 12'300 at 9.4 T and 18.8 T, respectively. We thus consider that polarization gives a more objective metric in the context of *d*DNP.

Comparison with a thermal equilibrium reference. The polarization can be measured by comparing the signal integral of the hyperpolarized signal with that of a thermal equilibrium reference. The most direct comparison is the following: after recording the liquid-state hyperpolarized signal, the sample is allowed to remain in the spectrometer until the hyperpolarization has completely vanished, *i.e.,* until thermal equilibrium is established. Then, a thermal equilibrium signal is recorded on the very sample produced by the *d*DNP experiment, with the same *rf*-probe on the same nucleus (only changing the number of scans, nutation angle and receiver gain, if appropriate). We will see how to calculate the polarization based on such measurement. In general, the polarization is given by:

$$P = P^{TE}\epsilon^{DNP} \quad (19)$$

where P^{TE} is the spin polarization at thermal equilibrium, calculated using the Boltzmann distribution, see Section 1. As an example, the ^{13}C thermal polarization at 9.4 T and 298 K is 8.097x10^{-6}. In general, the signal enhancement is given by the ratio between the hyperpolarized and thermal equilibrium signals, both normalized by the receiver gain, the number of scans and the pulse angle, S_n^{DNP} and S_n^{TE}, respectively:

$$\epsilon^{DNP} = \frac{S_n^{DNP}}{S_n^{TE}} \quad (20)$$

where the normalized signal integral corresponds to that obtained with a single π/2 pulse and a receiver gain of 1. For a number of scans *NS*, a pulse angle θ and a receiver gain *RG* (assuming a linear scale), the normalized signal S_n is:

$$S_n = \frac{S}{RG \cdot NS \cdot \sin\theta} \quad (21)$$

In particular, a common case is to record the hyperpolarized signals with small angle *rf*-pulses without averaging several scans while the thermal equilibrium is obtained by summing NS^{TE} scans recorded with π/2 pulses. In this case, the signal enhancement yields:

$$\epsilon^{DNP} = \frac{S^{DNP}}{S^{TE}} \frac{RG^{TE}}{RG^{DNP}} \frac{NS^{TE}}{\sin\theta^{DNP}} \quad (22)$$

where the symbols and indices have the same meaning as above. However, it might not always be possible to record the thermal equilibrium signal, either because the sensitivity is too low or because the hyperpolarized solute has been consumed during the experiment (among other reasons). This situation may be encountered, for example, with ^{13}C hyperpolarization and liquid-state detection at low magnetic fields. For example, in the case of [1-^{13}C] pyruvate, the three ^{1}H methyl spins may be easily detected at low field in a single scan while the ^{13}C signal would require the averaging of an outrageous number of scans after sample dissolution.

In this case, after the *d*DNP experiment, once the hyperpolarized signal has decayed, the ^{1}H (or other nuclear spin) signal is recorded with sufficient SNR. In a separate experiment, a reference sample with a known concentration is measured. This allows for the determination of the normalized molar signal integral per equivalent solute spin, that is, the normalized signal integral for a solute concentration of 1 molL^{-1} where the number of equivalent spins contributing to the integrated signal n_{eq} has been accounted for:

$$S_{n,m} = \frac{S}{RG \cdot NS \cdot C \cdot n_{eq}} \quad (23)$$

where *C* is the concentration of the solute in the reference sample. This quantity can be measured for both ^{1}H and ^{13}C on the reference sample. The concentration of the solute in the *d*DNP sample is then determined comparing its ^{1}H thermal signal integral with that of the reference sample:

$$C^{DNP} = \frac{S_n^{TE}(^1H)}{S_{n,m}^{REF}(^1H)} \frac{1}{n_{eq}(^1H)} \quad (24)$$

where S_n^{TE} and $S_{n,m}^{REF}$ are normalized ^{1}H signal integral of the *d*DNP sample and the normalized molar ^{1}H signal integral per equivalent spin of reference sample, respectively, while $n_{eq}(^1H)$ is the number of equivalent ^{1}H nuclei integrated for the thermal equilibrium signal ($n_{eq}(^1H) = 3$ in the case of pyruvate). The ^{13}C thermal equilibrium signal integral of the *d*DNP sample $S_n^{TE}(^{13}C)$ which could not be measured directly can be calculated using the previously calculated concentration of the solute C^{DNP} and normalized molar ^{13}C signal integral per equivalent spin of reference sample $S_{n,m}^{REF}(^{13}C)$:

$$S_n^{TE}(^{13}C) = S_{n,m}^{REF}(^{13}C) \cdot C^{DNP} \cdot n_{eq}(^{13}C) \quad (25)$$

where $n_{eq}(^{13}C)$ is the number of equivalent ^{13}C spins of the hyperpolarized signal. In the case of [1-^{13}C] pyruvate, there is a single ^{13}C spin, so this number is 1. Finally, the calculated thermal equilibrium signal is used to estimate the signal enhancement and the polarization of the hyperpolarized spins by using Equations 19 and 20.

We previously mentioned the case where the hyperpolarized solute would be consumed during the course of the liquid-state experiment. The use of the method discussed above supposes that the signal of some nuclei of the solute can be recorded after the hyperpolarization has decayed. If the solute was consumed during the experiment, its concentration at the moment of injection needs to be estimated by other means. For example, provided the dissolution and injection process is sufficiently reproducible, a blank experiment without chemical reaction can be performed to measure the concentration of the solute in the liquid-state. If such an experiment is possible, the method above may be used to measure the polarization.

Absolute polarization quantification by SPY-MR. An alternative strategy allows for the absolute polarization quantification without relying on a thermal equilibrium reference measurement [45]. This method is only applicable for *J*-coupled spins and its application is straightforward only in the case where the hyperpolarized spin has a weakly coupled neighbour. Let us assume that we want to measure the polarization of a spin-½ labelled A which is weakly coupled to spins X_n. The coupling of A to X splits the NMR line of X_n into a doublet. In conventional NMR, *i.e.,* when the nuclear spin polarization is weak, the two peaks of the doublet of X_n have equal intensities. Indeed, their relative intensity corresponds to the probability of finding A in state α or β; the two probabilities are practically equal when the polarization is low and so the two lines have equal intensities. However, when the polarization is far from zero, the excess of one nuclear state of A over the other causes the doublet of X_n to become asymmetric. The polarization of A may therefore be read straightforwardly from the asymmetry of X_n (for the case where the signs of the gyromagnetic ratios of the two spins are the same):

$$P_A = \mathrm{sgn}(J_{AX}) \frac{S_{LF}^X - S_{HF}^X}{S_{LF}^X + S_{HF}^X} \quad (26)$$

where J_{AX}, S_{LF}^X and S_{HF}^X are the *J*-coupling between A and X_n and the signal intensities of the low and high frequency lines of the doublet, respectively. An interesting aspect of this method is that it allows for the determination of the sign of the *J*-coupling, provided one knows the sign of the spin polarization that the *d*DNP experiment has produced. The method may also be applicable to larger spin systems but the equations are not detailed here [45].

Equation 26 applies if the coupling between A and X_n is weak, which is always true for heteronuclei at high field. This condition may still hold true in many homonuclear cases. The reader is referred to the original paper for the exact limits [45]. Furthermore, the asymmetry of X_n reflects the Zeeman population of A only if higher spin orders are not populated. Certain relaxation pathways may be favoured during the transfer of the molecule from the polarizer to the liquid-state spectrometer, causing an excess/lack of an $2\hat{I}_{iz}\hat{I}_{jz}$ term. The presence of such terms in the density operator results in an

asymmetry which need not be a true reflection of the polarization before the transfer[177]. Note that a deviation from the high temperature approximation, i.e., from the linear approximation of Boltzmann's law, automatically leads to the appearance of a $2\hat{I}_{iz}\hat{I}_{jz}$ term.

As compared with the use of a thermal equilibrium reference sample, polarization quantification by SPY-MR has the advantage of being faster since it does not require the detection of further signals in addition to the hyperpolarized one. Moreover, it is not subject to changes in the NMR sample that may occur between the acquisition of the hyperpolarized and thermal equilibrium spectra, such as chemical degradation, precipitation or appearance/disappearance of bubbles, to name a few. On the other hand, the SPY approach requires a good understanding of the spin dynamics at play during the transfer as one could falsely attribute a high polarization in the liquid-state to what could in fact be the presence of multiple spin order. Finally, we note that the two methods combined together can be used as a means to assess the nature of polarization losses during the transfer.

Polarization decay and the effect of pulses. The decay of hyperpolarization in the liquid-state is usually monitored using a series of small angle *rf*-pulses which allows for the determination of the T_1 relaxation time constant of the hyperpolarized solute. However, if the effect of the *rf*-pulses is not negligible, the fitted T_1 time constant may be underestimated. When the effect of the *rf*-pulses is negligible, the normalized mono-exponentially decaying signal as a function of time is:

$$\frac{S(t)}{S_0} = \exp\left(-\frac{t}{T_1}\right) \quad (27)$$

Assuming a constant delay τ between the pulses with angle θ, the corrected formula yields:

$$\frac{S(t)}{S_0} = \exp\left(-\frac{t}{T_1}\right)(\cos\theta)^{\frac{t}{\tau}} \quad (28)$$

This equation can be rewritten as:

$$\frac{S(t)}{S_0} = \exp\left\{-t\left(\frac{1}{T_1} - \frac{\ln|\cos\theta|}{\tau}\right)\right\} \quad (29)$$

Inspection of this formula shows that the effect of the *rf*-pulses preserves the mono-exponential character of the decay curve. As a consequence, if one does not pay attention to the effect of the *rf*-pulses, the T_1 constant may be underestimated. In the worst case, the decay is solely the consequences of the *rf*-pulses and not of relaxation. Figure 46 shows simulated decays that would be obtained using different *rf*-pulse angles. The figure shows how the apparent T_1 is affected by the *rf*-pulse angle.

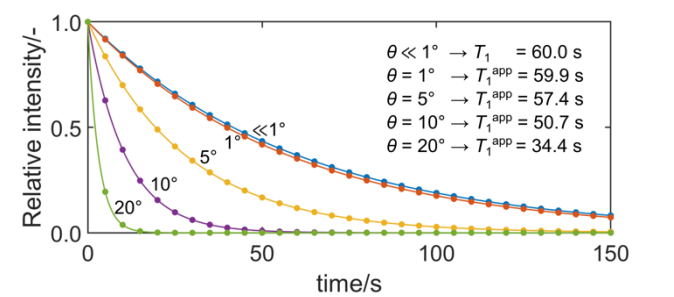

Figure 46: Simulated hyperpolarized decay detected with pulses separated by 5 s with different *rf*-pulse angles for a nucleus with T_1 = 60 s. Dots represent the intensity of each measurement. Lines correspond to the decays obtained by Equation 29. The value T_1^{app} is the apparent T_1 that would be obtained if the approximate Equation 27 were used.

9. Conclusions

We have presented a detailed review of *d*DNP experimentation, with the aim of providing useful guidelines and tips for readers in order to easily perform *d*DNP experiments in their own laboratories. We have discussed the following key areas: sample preparation and health; systems diagnosis and maintenance; mechanics and spin dynamics of sample dissolution; and the reliable quantification of nuclear spin polarization levels. For each subject we have highlighted problematic issues and provided simple solutions. These insights have been gained from our own practical experience in our own laboratory. Although methods and instrumentation will continue to evolve in the field, *e.g.,* by the extended introduction of cryogen-free DNP polarizers and the implementation of *d*DNP at higher and higher magnetic fields, the basic conditions required in order to perform a successful *d*DNP experiment will remain largely the same, and as a result; we hope that, as the *d*DNP field broadens, this review will continue to provide assistance for those new to the field as well as longstanding members of the community, well into the future.

10. Acknowledgements

This research was supported by ENS-Lyon, the French CNRS, Lyon 1 University, the European Research Council under the European Union's Horizon 2020 research and innovation program (ERC Grant Agreements No. 714519 / HP4all and Marie Skłodowska-Curie Grant Agreement No. 766402 / ZULF). The authors gratefully acknowledge *Bruker Biospin*, and particularly Dmitry Eshchenko, Roberto Melzi, Marc Rossire, Marco Sacher and James Kempf for their technical advice and experimental support. The authors are indebted to Patrick Giraudeau, Dennis Kurzbach and Arnab Dey for kindly proof-reading the manuscript prior to submission, and Geoffrey Bodenhausen and Dominique Massiot for editing the manuscript and for all their corrections and constructive feedback. The authors additionally acknowledge Catherine Jose and Christophe Pages of the ISA Prototype Service; and Stéphane Martinez of the UCBL mechanical workshop for assistance with maintaining apparatus software and hardware.

11. References

[1] D. I. Hoult and R. E. Richards, "The signal-to-noise ratio of the nuclear magnetic resonance experiment," *J. Magn. Reson.*, vol. 24, no. 1, pp. 71–85, 1976, doi: 10.1016/0022-2364(76)90233-X.

[2] J. H. Ardenkjaer-Larsen, "On the present and future of dissolution-DNP," *J. Magn. Reson.*, vol. 264, pp. 3–12, Mar. 2016, doi: 10.1016/j.jmr.2016.01.015.

[3] M. L. Hirsch, B. A. Smith, M. Mattingly, A. G. Goloshevsky, M. Rosay, and J. G. Kempf, "Transport and imaging of brute-force 13C hyperpolarization," *J. Magn. Reson.*, vol. 261, pp. 87–94, 2015, doi: 10.1016/j.jmr.2015.09.017.

[4] M. L. Hirsch, N. Kalechofsky, A. Belzer, M. Rosay, and J. G. Kempf, "Brute-Force Hyperpolarization for NMR and MRI," *J. Am. Chem. Soc.*, vol. 137, no. 26, pp. 8428–8434, Jul. 2015, doi: 10.1021/jacs.5b01252.

[5] D. G. Gadian, K. S. Panesar, A. J. Perez Linde, A. J. Horsewill, W. Köckenberger, and J. R. Owers-Bradley, "Preparation of highly polarized nuclear spin systems using brute-force and low-field thermal mixing," *Phys. Chem. Chem. Phys.*, vol. 14, no. 16, pp. 5397–5402, Mar. 2012, doi: 10.1039/c2cp23536f.

[6] D. T. Peat, M. L. Hirsch, D. G. Gadian, A. J. Horsewill, J. R. Owers-Bradley, and J. G. Kempf, "Low-field thermal mixing in [1-13C] pyruvic acid for brute-force hyperpolarization," *Phys. Chem. Chem. Phys.*, vol. 18, no. 28, pp. 19173–19182, 2016, doi: 10.1039/c6cp02853e.

[7] A. Abragam and M. Goldman, "Principles of dynamic nuclear polarisation," *Reports Prog. Phys.*, vol. 41, no. 3, pp. 395–467, 1978, doi: 10.1088/0034-4885/41/3/002.

[8] A. S. Lilly Thankamony, J. J. Wittmann, M. Kaushik, and B. Corzilius, "Dynamic nuclear polarization for sensitivity enhancement in modern solid-state NMR," *Prog. Nucl. Magn. Reson. Spectrosc.*, vol. 102–103, pp. 120–195, Nov. 2017, doi: 10.1016/j.pnmrs.2017.06.002.

[9] J. H. Ardenkjær-Larsen, B. Fridlund, A. Gram, G. Hansson, L. Hansson, M. H. Lerche, R. Servin, M. Thaning, and K. Golman, "Increase in signal-to-noise ratio of >10,000 times in liquid-state NMR," *Proc. Natl. Acad. Sci. U. S. A.*, vol. 100, no. 18, pp. 10158–10163, Sep. 2003, doi: 10.1073/pnas.1733835100.

[10] J. H. Ardenkjaer-Larsen, "Hyperpolarized MR – What's up Doc?," *J. Magn. Reson.*, vol. 306, pp. 124–127, 2019, doi: 10.1016/j.jmr.2019.07.017.

[11] J. H. Ardenkjaer-Larsen, "Introduction to dissolution DNP: Overview, instrumentation, and human applications," *eMagRes*, vol. 7, no. 4, pp. 63–78, 2018, doi: 10.1002/9780470034590.emrstm1549.

[12] W. T. Wenckebach, "Dynamic nuclear polarization via the cross effect and thermal mixing: A. The role of triple spin flips," *J. Magn. Reson.*, vol. 299, pp. 124–134, 2019, doi: 10.1016/j.jmr.2018.12.018.

[13] W. T. Wenckebach, "Dynamic nuclear polarization via the cross effect and thermal mixing: B. Energy transport," *J. Magn. Reson.*, vol. 299, pp. 151–167, Feb. 2019, doi: 10.1016/j.jmr.2018.12.020.

[14] S. Jannin, A. Comment, and J. J. van der Klink, "Dynamic Nuclear Polarization by Thermal Mixing Under Partial Saturation," *Appl. Magn. Reson.*, vol. 43, no. 1–2, pp. 59–68, 2012, doi: 10.1007/s00723-012-0363-4.

[15] D. Shimon, Y. Hovav, I. Kaminker, A. Feintuch, D. Goldfarb, and S. Vega, "Simultaneous DNP enhancements of 1H and 13C nuclei: Theory and experiments," *Phys. Chem. Chem. Phys.*, vol. 17, no. 17, pp. 11868–11883, 2015, doi: 10.1039/c5cp00406c.

[16] Y. Hovav, A. Feintuch, and S. Vega, "Theoretical aspects of dynamic nuclear polarization in the solid state - The cross effect," *J. Magn. Reson.*, vol. 214, pp. 29–41, 2012, doi: 10.1016/j.jmr.2011.09.047.

[17] W. T. Wenckebach, "Spectral diffusion and dynamic nuclear polarization: Beyond the high temperature approximation," *J. Magn. Reson.*, vol. 284, pp. 104–114, 2017, doi: 10.1016/j.jmr.2017.10.001.

[18] V. A. Atsarkin, "Dynamic nuclear polarization: Yesterday, today, and tomorrow," *J. Phys. Conf. Ser.*, vol. 324, p. 012003, 2011, doi: 10.1088/1742-6596/324/1/012003.

[19] K. V. Kovtunov, E. V. Pokochueva, O. G. Salnikov, S. F. Cousin, D. Kurzbach, B. Vuichoud, S. Jannin, E. Y.

Chekmenev, B. M. Goodson, D. A. Barskiy, and I. V. Koptyug, “Hyperpolarized NMR Spectroscopy: *d* - DNP, PHIP, and SABRE Techniques,” *Chem. - An Asian J.*, vol. 13, no. 15, pp. 1857–1871, Aug. 2018, doi: 10.1002/asia.201800551.

[20] K. M. Brindle, S. E. Bohndiek, F. A. Gallagher, and M. I. Kettunen, “Tumor imaging using hyperpolarized 13C magnetic resonance spectroscopy,” *Magn. Reson. Med.*, vol. 66, no. 2, pp. 505–519, 2011, doi: 10.1002/mrm.22999.

[21] B. Plainchont, P. Berruyer, J.-N. N. Dumez, S. Jannin, and P. Giraudeau, “Dynamic Nuclear Polarization Opens New Perspectives for NMR Spectroscopy in Analytical Chemistry,” *Anal. Chem.*, vol. 90, no. 6, pp. 3639–3650, Mar. 2018, doi: 10.1021/acs.analchem.7b05236.

[22] S. Jannin, J.-N. N. Dumez, P. Giraudeau, and D. Kurzbach, “Perspectives in Magnetic Resonance Application and methodology of dissolution dynamic nuclear polarization in physical, chemical and biological contexts,” *J. Magn. Reson.*, vol. 305, pp. 41–50, 2019, doi: 10.1016/j.jmr.2019.06.001.

[23] A. A. Bornet, A. Pinon, A. Jhajharia, M. Baudin, X. Ji, L. Emsley, G. Bodenhausen, J. H. Ardenkjaer-Larsen, and S. Jannin, “Microwave-gated dynamic nuclear polarization,” *Phys. Chem. Chem. Phys.*, vol. 18, no. 44, pp. 30530–30535, 2016, doi: 10.1039/c6cp05587g.

[24] W. Kockenberger, “Dissolution dynamic nuclear polarization,” in *eMagRes*, vol. 3, no. 2, Chichester, UK: John Wiley & Sons, Ltd, 2014, pp. 161–170.

[25] Ü. Akbey, W. Trent Franks, A. Linden, M. Orwick-Rydmark, S. Lange, and H. Oschkinat, *Dynamic nuclear polarization enhanced NMR in the solid-state*, vol. 338. 2013.

[26] F. Jähnig, G. Kwiatkowski, and M. Ernst, “Conceptual and instrumental progress in dissolution DNP,” *J. Magn. Reson.*, vol. 264, no. Supplement C, pp. 22–29, 2016, doi: 10.1016/j.jmr.2015.12.024.

[27] J. Van Bentum, B. Van Meerten, M. Sharma, and A. Kentgens, “Perspectives on DNP-enhanced NMR spectroscopy in solutions,” *J. Magn. Reson.*, vol. 264, pp. 59–67, 2016, doi: 10.1016/j.jmr.2016.01.010.

[28] K. R. Keshari and D. M. Wilson, “Chemistry and biochemistry of 13C hyperpolarized magnetic resonance using dynamic nuclear polarization,” *Chem. Soc. Rev.*, vol. 43, no. 5, pp. 1627–1659, 2014, doi: 10.1039/c3cs60124b.

[29] P. Berthault, C. Boutin, C. Martineau-corcos, and G. Carret, “Progress in Nuclear Magnetic Resonance Spectroscopy Use of dissolved hyperpolarized species in NMR : Practical considerations,” *Prog. Nucl. Magn. Reson. Spectrosc.*, vol. 118–119, pp. 74–90, 2020, doi: 10.1016/j.pnmrs.2020.03.002.

[30] S. E. Day, M. I. Kettunen, F. A. Gallagher, D. E. Hu, M. Lerche, J. Wolber, K. Golman, J. H. Ardenkjaer-Larsen, and K. M. Brindle, “Detecting tumor response to treatment using hyperpolarized 13C magnetic resonance imaging and spectroscopy,” *Nat. Med.*, vol. 13, no. 11, pp. 1382–1387, 2007, doi: 10.1038/nm1650.

[31] P. Miéville, S. Jannin, L. Helm, and G. Bodenhausen, “Kinetics of yttrium-Ligand complexation monitored using hyperpolarized 89Y as a model for gadolinium in contrast agents,” *J. Am. Chem. Soc.*, vol. 132, no. 14, pp. 5006–5007, 2010, doi: 10.1021/ja1013954.

[32] A. Bornet and S. Jannin, “Optimizing dissolution dynamic nuclear polarization,” *J. Magn. Reson.*, vol. 264, pp. 13–21, 2016, doi: 10.1016/j.jmr.2015.12.007.

[33] J. Leggett, R. Hunter, J. Granwehr, R. Panek, A. J. Perez-Linde, A. J. Horsewill, J. McMaster, G. Smith, and W. Köckenberger, “A dedicated spectrometer for dissolution DNP NMR spectroscopy,” *Phys. Chem. Chem. Phys.*, vol. 12, no. 22, p. 5883, 2010, doi: 10.1039/c002566f.

[34] K. Kouřil, H. Kouřilová, S. Bartram, M. H. Levitt, and B. Meier, “Scalable dissolution-dynamic nuclear polarization with rapid transfer of a polarized solid,” Dec. 2019. doi: 10.1038/s41467-019-09726-5.

[35] A. Leavesley, C. B. Wilson, M. Sherwin, and S. Han, “Effect of water/glycerol polymorphism on dynamic nuclear polarization,” *Phys. Chem. Chem. Phys.*, vol. 20, no. 15, pp. 9897–9903, 2018, doi: 10.1039/c8cp00358k.

[36] L. Lumata, Z. Kovacs, A. D. Sherry, C. Malloy, S. Hill, J. Van Tol, L. Yu, L. Song, and M. E. Merritt, “Electron spin resonance studies of trityl OX063 at a concentration optimal for DNP,” *Phys. Chem. Chem. Phys.*, vol. 15, no. 24, pp. 9800–9807, 2013, doi: 10.1039/c3cp50186h.

[37] L. L. Lumata, R. Martin, A. K. Jindal, Z. Kovacs, M. S. Conradi, and M. E. Merritt, “Development and performance of a 129-GHz dynamic nuclear polarizer in an ultra-wide bore superconducting magnet,” *Magn. Reson. Mater. Physics, Biol. Med.*, vol. 28, no. 2, pp. 195–205, 2015, doi: 10.1007/s10334-014-0455-2.

[38] Y. Crémillieux, F. Goutailler, B. Montcel, D. Grand, G. Vermeulen, and P. E. Wolf, “A Super-Wide Bore DNP System for Multiple Sample Polarization: Cryogenic Performance and Polarization at Low Temperature,” *Appl. Magn. Reson.*, vol. 43, no. 1–2, pp. 167–180, 2012, doi: 10.1007/s00723-012-0354-5.

[39] M. Batel, M. Krajewski, K. Weiss, O. With, A. Däpp, A. Hunkeler, M. Gimersky, K. P. Pruessmann, P. Boesiger, B. H. Meier, S. Kozerke, and M. Ernst, “A multi-sample 94 GHz dissolution dynamic-nuclear-polarization system,” *J. Magn. Reson.*, vol. 214, no. 1, pp. 166–174, 2012, doi: 10.1016/j.jmr.2011.11.002.

[40] A. Bornet, J. Milani, B. Vuichoud, A. J. Perez Linde, G. Bodenhausen, and S. Jannin, “Microwave frequency modulation to enhance Dissolution Dynamic Nuclear Polarization Dedicated to To Martial Rey, as a token of appreciation.,” *Chem. Phys. Lett.*, vol. 602, pp. 63–67, 2014, doi: 10.1016/j.cplett.2014.04.013.

[41] B. Vuichoud, A. Bornet, F. de Nanteuil, J. Milani, E. Canet, X. Ji, P. Miéville, E. Weber, D. Kurzbach, A. Flamm, R. Konrat, A. D. Gossert, S. Jannin, and G. Bodenhausen, “Filterable Agents for Hyperpolarization of Water, Metabolites, and Proteins,” *Chem. - A Eur. J.*, vol. 22, no. 41, pp. 14696–14700, Oct. 2016, doi: 10.1002/chem.201602506.

[42] M. Cavaillès, A. A. Bornet, X. Jaurand, B. Vuichoud, D. Baudouin, M. Baudin, L. Veyre, G. Bodenhausen, J.-N. Dumez, S. Jannin, C. Copéret, and C. Thieuleux, “Tailored Microstructured Hyperpolarizing Matrices for Optimal Magnetic Resonance Imaging,” *Angew. Chemie - Int. Ed.*, vol. 57, no. 25, pp. 7453–7457, Jun.

2018, doi: 10.1002/anie.201801009.
[43] B. C. Dollmann, M. J. N. Junk, M. Drechsler, H. W. Spiess, D. Hinderberger, and K. Münnemann, "Thermoresponsive, spin-labeled hydrogels as separable DNP polarizing agents," *Phys. Chem. Chem. Phys*, vol. 12, no. 22, p. 5850, 2010, doi: 10.1039/c003349a.
[44] D. Gajan, A. Bornet, B. Vuichoud, J. Milani, R. Melzi, H. A. Van Kalkeren, L. Veyre, C. Thieuleux, M. P. Conley, W. R. Grüning, M. Schwarzwälder, A. Lesage, C. Copéret, G. Bodenhausen, L. Emsley, and S. Jannin, "Hybrid polarizing solids for pure hyperpolarized liquids through dissolution dynamic nuclear polarization," *Proc. Natl. Acad. Sci.*, vol. 111, no. 41, pp. 14693–14697, Oct. 2014, doi: 10.1073/pnas.1407730111.
[45] B. Vuichoud, J. Milani, Q. Chappuis, A. Bornet, G. Bodenhausen, and S. Jannin, "Measuring absolute spin polarization in dissolution-DNP by Spin PolarimetrY Magnetic Resonance (SPY-MR) Dedicated to Stefan Schäublin, Alfred Höhener and Richard Ernst for their pioneering work.," *J. Magn. Reson.*, vol. 260, pp. 127–135, 2015, doi: 10.1016/j.jmr.2015.09.006.
[46] Y. Li, A. Equbal, K. Tagami, S. Han, and H. Songi, "Electron spin density matching for cross-effect dynamic nuclear polarization ChemComm Chemical Communications," *Chem. Commun.*, vol. 55, no. 53, pp. 7571–7716, 2019, doi: 10.1039/c9cc03499d.
[47] J. Granwehr, J. Leggett, and W. Köckenberger, "A low-cost implementation of EPR detection in a dissolution DNP setup," *J. Magn. Reson.*, vol. 187, no. 2, pp. 266–276, 2007, doi: 10.1016/j.jmr.2007.05.011.
[48] M. M. Albannay, J. M. O. Vinther, A. Capozzi, V. Zhurbenko, and J. H. Ardenkjaer-Larsen, "Optimized microwave delivery in dDNP," *J. Magn. Reson.*, vol. 305, pp. 58–65, 2019, doi: 10.1016/j.jmr.2019.06.004.
[49] P. Miéville, S. Jannin, and G. Bodenhausen, "Relaxometry of insensitive nuclei: Optimizing dissolution dynamic nuclear polarization," *J. Magn. Reson.*, vol. 210, no. 1, pp. 137–140, 2011, doi: 10.1016/j.jmr.2011.02.006.
[50] J. Milani, B. Vuichoud, A. Bornet, P. Miéville, R. Mottier, S. Jannin, and G. Bodenhausen, "A magnetic tunnel to shelter hyperpolarized fluids," *Rev. Sci. Instrum.*, vol. 86, no. 2, 2015, doi: 10.1063/1.4908196.
[51] P. Miéville, P. Ahuja, R. Sarkar, S. Jannin, P. R. P. R. P. R. Vasos, S. Gerber-Lemaire, M. Mishkovsky, A. Comment, R. Gruetter, O. Ouari, P. Tordo, and G. Bodenhausen, "Scavenging free radicals to preserve enhancement and extend relaxation times in NMR using dynamic nuclear polarization," *Angew. Chemie - Int. Ed.*, vol. 49, no. 35, p. 7834, 2010, doi: 10.1002/anie.201000934.
[52] A. Bornet, R. Melzi, A. J. Perez Linde, P. Hautle, B. Van Den Brandt, S. Jannin, and G. Bodenhausen, "Boosting dissolution dynamic nuclear polarization by cross polarization," *J. Phys. Chem. Lett.*, vol. 4, no. 1, pp. 111–114, 2013, doi: 10.1021/jz301781t.
[53] S. R. Hartmann and E. L. Hahn, "Nuclear double resonance in the rotating frame," *Phys. Rev.*, vol. 128, no. 5, pp. 2042–2053, 1962, doi: 10.1103/PhysRev.128.2042.
[54] A. Pines, M. G. Gibby, and J. S. Waugh, "Proton-enhanced nuclear induction spectroscopy 13C chemical shielding anisotropy in some organic solids," *Chem. Phys. Lett.*, vol. 15, no. 3, pp. 373–376, 1972, doi: 10.1016/0009-2614(72)80191-X.
[55] S. Jannin, A. A. Bornet, S. Colombo, and G. Bodenhausen, "Low-temperature cross polarization in view of enhancing dissolution Dynamic Nuclear Polarization in NMR," *Chem. Phys. Lett.*, vol. 517, no. 4–6, pp. 234–236, 2011, doi: 10.1016/j.cplett.2011.10.042.
[56] A. Bornet, R. Melzi, S. Jannin, and G. Bodenhausen, "Cross Polarization for Dissolution Dynamic Nuclear Polarization Experiments at Readily Accessible Temperatures $1.2 < T < 4.2$ K," *Appl. Magn. Reson.*, vol. 43, no. 1–2, pp. 107–117, 2012, doi: 10.1007/s00723-012-0358-1.
[57] J. Milani, B. Vuichoud, A. Bornet, R. Melzi, S. Jannin, and G. Bodenhausen, "Hyperpolarization of nitrogen-15 nuclei by cross polarization and dissolution dynamic nuclear polarization," *Rev. Sci. Instrum.*, vol. 88, no. 1, 2017, doi: 10.1063/1.4973777.
[58] M. Otikovs, G. L. Olsen, Ē. Kupče, and L. Frydman, "Natural Abundance, Single-Scan 13C-13C-Based Structural Elucidations by Dissolution DNP NMR," *J. Am. Chem. Soc.*, vol. 141, no. 5, pp. 1857–1861, 2019, doi: 10.1021/jacs.8b12216.
[59] M. Baudin, B. Vuichoud, A. Bornet, G. Bodenhausen, and S. Jannin, "A cryogen-consumption-free system for dynamic nuclear polarization at 9.4 T," *J. Magn. Reson.*, vol. 294, pp. 115–121, Sep. 2018, doi: 10.1016/j.jmr.2018.07.001.
[60] B. Vuichoud, "Novel Sample Formulations for Pure and Persistent Hyperpolarized Solutions via Dissolution Dynamic Nuclear Polarization," 2017.
[61] K. Murata and H. Tanaka, "in aqueous organic solutions," *Nat. Commun.*, pp. 4–6, 2013, doi: 10.1038/ncomms3844.
[62] K. Murata, "Liquid--liquid transition without macroscopic phase separation in a water--glycerol mixture," *Nat. Mater.*, vol. 11, no. March, pp. 4–6, 2012, doi: 10.1038/nmat3271.
[63] I. Popov, A. G. Gutina, A. P. Sokolov, and Y. Feldman, "water – glycerol mixtures," pp. 18063–18071, 2015, doi: 10.1039/c5cp02851e.
[64] D. A. Jahn, J. Wong, J. Bachler, and N. Giovambattista, "Glass polymorphism in glycerol – water mixtures : I . A computer simulation study," no. Ldl, pp. 11042–11057, 2016, doi: 10.1039/c6cp00075d.
[65] P. Cerreia Vioglio, G. Mollica, M. Juramy, C. E. Hughes, P. A. Williams, F. Ziarelli, S. Viel, P. Thureau, and K. D. M. M. Harris, "Insights into the Crystallization and Structural Evolution of Glycine Dihydrate by In Situ Solid-State NMR Spectroscopy," *Angew. Chemie - Int. Ed.*, vol. 57, no. 22, pp. 6619–6623, May 2018, doi: 10.1002/anie.201801114.
[66] V. Berejnov, N. S. Husseini, A. Alsaied, and R. E. Thorne, "research papers Effects of cryoprotectant concentration and cooling rate on vitrification of aqueous solutions research papers," pp. 244–251, 2006, doi: 10.1107/S0021889806004717.
[67] N. Giovambattista and T. Loerting, "Glass polymorphism in glycerol–water mixtures: II. Experimental studies," pp. 11058–11068, 2016, doi: 10.1039/c5cp08069j.

[68] P. G. Debenedetti and H. E. Stanley, "[Debenedetti and Stanley, 2003] Supercooled and glassy water.pdf," *Physics Today*, vol. June. pp. 40–46, 2003.

[69] K. Yoshizawa, A. Toyotama, T. Okuzono, and J. Yamanaka, "Exclusion of impurity particles in charged colloidal crystals," *Soft Matter*, vol. 10, no. 19, pp. 3357–3361, 2014, doi: 10.1039/c3sm52912f.

[70] B. Wunderlich, "Theory of cold crystallization of high polymers," *J. Chem. Phys.*, vol. 29, no. 6, pp. 1395–1404, 1958, doi: 10.1063/1.1744729.

[71] E. M. M. Weber, G. Sicoli, H. Vezin, G. Frébourg, D. Abergel, G. Bodenhausen, and D. Kurzbach, "Sample Ripening through Nanophase Separation Influences the Performance of Dynamic Nuclear Polarization," *Angew. Chemie - Int. Ed.*, vol. 57, no. 18, pp. 5171–5175, 2018, doi: 10.1002/anie.201800493.

[72] D. Bruck, R. Dudley, C. A. Fyfe, and J. Van Delden, "Sample magnetization using immobilized free radicals for use in flow NMR systems," *J. Magn. Reson.*, vol. 42, no. 1, pp. 51–59, 1981, doi: 10.1016/0022-2364(81)90009-3.

[73] R. Gitti, C. Wild, C. Tsiao, K. Zimmer, T. E. Glass, and H. C. Dorn, "Solid-Liquid Intermolecular Transfer of Dynamic Nuclear Polarization. Enhanced Flowing Fluid]H NMR Signals via Immobilized Spin Labels," *J. Am. Chem. Soc.*, vol. 110, no. 7, pp. 2294–2296, 1988, doi: 10.1021/ja00215a047.

[74] D. L. Silverio, H. A. Van Kalkeren, T.-C. C. Ong, M. Baudin, M. Yulikov, L. Veyre, P. Berruyer, S. Chaudhari, D. Gajan, D. Baudouin, M. Cavaill es, B. Vuichoud, A. elien Bornet, G. Jeschke, G. Bodenhausen, A. Lesage, L. Emsley, S. Jannin, C. Thieuleux, C. Cop eret, M. Cavaillès, B. Vuichoud, A. Bornet, G. Jeschke, G. Bodenhausen, A. Lesage, L. Emsley, S. Jannin, C. Thieuleux, and C. Copéret, "Tailored Polarizing Hybrid Solids with Nitroxide Radicals Localized in Mesostructured Silica Walls," *Helv. Chim. Acta*, vol. 100, no. 6, 2017, doi: 10.1002/hlca.201700101.

[75] E. Besson, F. Ziarelli, E. Bloch, G. Gerbaud, S. Queyroy, S. Viel, and S. Gastaldi, "Silica materials with wall-embedded nitroxides provide efficient polarization matrices for dynamic nuclear polarization NMR," *Chem. Commun.*, vol. 52, no. 32, pp. 5531–5533, Apr. 2016, doi: 10.1039/c6cc01809b.

[76] T. Cheng, M. Mishkovsky, M. J. N. Junk, K. Münnemann, and A. Comment, "Producing Radical-Free Hyperpolarized Perfusion Agents for In Vivo Magnetic Resonance Using Spin-Labeled Thermoresponsive Hydrogel," *Macromol. Rapid Commun.*, vol. 37, no. 13, pp. 1074–1078, 2016, doi: 10.1002/marc.201600133.

[77] T. El Darai, S. F. Cousin, Q. Chappuis, M. Ceilllier, J. G. Kempf, D. Eshchenko, R. Melzi, M. Schnell, L. Gremillard, A. Bornet, J. Milani, Basile Buichou, O. Cala, D. Montarnal, and S. Jannin, "Porous Functionalized Polymers enable Generating and Transporting Hyperpolarized Arbitrary Solutions," *Nat. Res.*, pp. 1–20, 2021, doi: 10.21203/rs.3.rs-123790/v1.

[78] A. Cavagna, "Supercooled liquids for pedestrians," *Phys. Rep.*, vol. 476, no. 4–6, pp. 51–124, 2009, doi: 10.1016/j.physrep.2009.03.003.

[79] B. Lama, J. H. P. Collins, D. Downes, A. N. Smith, and J. R. Long, "Expeditious dissolution dynamic nuclear polarization without glassing agents," *NMR Biomed.*, vol. 29, no. 3, pp. 226–231, 2016, doi: 10.1002/nbm.3473.

[80] B. Y. J. L. Stephenson, "ICE CRYSTAL GROWTH D U R I N G T H E RAPID F R E E Z I N G OF TISSUES," vol. 2, no. 4, pp. 45–52, 1956.

[81] C. Kroll and H. H. Borchert, "Metabolism of the stable nitroxyl radical 4-oxo-2,2,6,6-tetramethylpiperidine-N-oxyl (TEMPONE)," *Eur. J. Pharm. Sci.*, vol. 8, no. 1, pp. 5–9, 1999, doi: 10.1016/S0928-0987(98)00047-5.

[82] C. L. Hawkins and M. J. Davies, "Detection and characterisation of radicals in biological materials using EPR methodology," *Biochim. Biophys. Acta - Gen. Subj.*, vol. 1840, no. 2, pp. 708–721, 2014, doi: 10.1016/j.bbagen.2013.03.034.

[83] J. B. Gerken and S. S. Stahl, "High-potential electrocatalytic O2 reduction with nitroxyl/NOx mediators: Implications for fuel cells and aerobic oxidation catalysis," *ACS Cent. Sci.*, vol. 1, no. 5, pp. 234–243, 2015, doi: 10.1021/acscentsci.5b00163.

[84] G. R. Eaton, S. S. Eaton, D. P. Barr, and R. T. Weber, *Quantitative EPR*, SpringerWi. Springer New York, 2010.

[85] A. Comment, B. Van Den Brandt, K. Uffmann, F. Kurdzesau, S. Jannin, J. A. Konter, P. Hautle, W. T. Wenckebach, R. Gruetter, and J. J. Van Der Klink, "Design and Performance of DNP Polarizer Coupled to a rodent MRI Scanner," *Concepts Magn. Reson. Part B Magn. Reson. Eng. An Educ. J.*, vol. 31, no. 4, pp. 255–269, 2007.

[86] L. L. Lumata, M. E. Merritt, C. R. Malloy, A. D. Sherry, J. Van Tol, L. Song, and Z. Kovacs, "Dissolution DNP-NMR spectroscopy using galvinoxyl as a polarizing agent," *J. Magn. Reson.*, vol. 227, pp. 14–19, 2013, doi: 10.1016/j.jmr.2012.11.006.

[87] L. Lumata, A. K. Jindal, M. E. Merritt, C. R. Malloy, A. D. Sherry, and Z. Kovacs, "DNP by thermal mixing under optimized conditions yields >60 000-fold enhancement of 89Y NMR signal," *J. Am. Chem. Soc.*, vol. 133, no. 22, pp. 8673–8680, 2011, doi: 10.1021/ja201880y.

[88] Y. Matsuki, T. Maly, O. Ouari, H. Karoui, F. Le Moigne, E. Rizzato, S. Lyubenova, J. Herzfeld, T. Prisner, P. Tordo, and R. G. Griffin, "Dynamic Nuclear Polarization with a Rigid Biradical," *Angew. Chemie*, vol. 121, no. 27, pp. 5096–5100, Jun. 2009, doi: 10.1002/ange.200805940.

[89] K. Adamic, D. F. Bowman, T. Gillan, and K. U. Ingold, "Kinetic Applications of Electron Paramagnetic Resonance Spectroscopy. I. Self-Reactions of Diethyl Nitroxide Radicals," *J. Am. Chem. Soc.*, vol. 93, no. 4, pp. 902–908, 1971, doi: 10.1021/ja00733a018.

[90] R. G. Hicks, "What's new in stable radical chemistry?," *Org. Biomol. Chem.*, vol. 5, no. 9, pp. 1321–1338, 2007, doi: 10.1039/b617142g.

[91] J. E. Nutting, M. Rafiee, and S. S. Stahl, "Tetramethylpiperidine N-Oxyl (TEMPO), Phthalimide N-Oxyl (PINO), and Related N-Oxyl Species: Electrochemical Properties and Their Use in Electrocatalytic Reactions," *Chem. Rev.*, vol. 118, no.

9, pp. 4834–4885, 2018, doi: 10.1021/acs.chemrev.7b00763.
[92] J. H. Ardenkjaer-Larsen, A. M. Leach, N. Clarke, J. Urbahn, D. Anderson, and T. W. Skloss, “Dynamic nuclear polarization polarizer for sterile use intent,” *NMR Biomed.*, vol. 24, no. 8, pp. 927–932, 2011, doi: 10.1002/nbm.1682.
[93] A. B. Barnes, E. Markhasin, E. Daviso, V. K. Michaelis, E. A. Nanni, S. K. Jawla, E. L. Mena, R. DeRocher, A. Thakkar, P. P. Woskov, J. Herzfeld, R. J. Temkin, and R. G. Griffin, “Dynamic nuclear polarization at 700MHz/460GHz,” *J. Magn. Reson.*, vol. 224, pp. 1–7, 2012, doi: https://doi.org/10.1016/j.jmr.2012.08.002.
[94] P. R. Jensen, S. Meier, J. H. Ardenkjær-Larsen, J. Ø. Duus, M. Karlsson, and M. H. Lerche, “Detection of low-populated reaction intermediates with hyperpolarized NMR,” *Chem. Commun.*, no. 34, pp. 5168–5170, 2009, doi: 10.1039/B910626J.
[95] B. L. Koelsch, R. Sriram, K. R. Keshari, C. Leon Swisher, M. Van Criekinge, S. Sukumar, D. B. Vigneron, Z. J. Wang, P. E. Z. Larson, and J. Kurhanewicz, “Separation of extra- and intracellular metabolites using hyperpolarized (13)C diffusion weighted MR,” *J. Magn. Reson.*, vol. 270, pp. 115–123, Sep. 2016, doi: 10.1016/j.jmr.2016.07.002.
[96] E. Miclet, D. Abergel, A. Bornet, J. Milani, S. Jannin, and G. Bodenhausen, “Toward quantitative measurements of enzyme kinetics by dissolution dynamic nuclear polarization,” *J. Phys. Chem. Lett.*, vol. 5, no. 19, pp. 3290–3295, 2014, doi: 10.1021/jz501411d.
[97] S. Meier, M. Karlsson, P. R. Jensen, M. H. Lerche, and J. Ø. Duus, “Metabolic pathway visualization in living yeast by DNP-NMR,” *Mol. BioSyst.*, vol. 7, no. 10, pp. 2834–2836, 2011, doi: 10.1039/C1MB05202K.
[98] J. M. O. O. Vinther, V. Zhurbenko, M. M. Albannay, and J. H. Ardenkjær-Larsen, “Design of a local quasi-distributed tuning and matching circuit for dissolution DNP cross polarization,” *Solid State Nucl. Magn. Reson.*, vol. 102, pp. 12–20, 2019, doi: 10.1016/j.ssnmr.2019.04.006.
[99] B. Aghelnejad, G. Bodenhausen, and S. Marhabaie, “A Low-Temperature Broadband NMR Probe for Multinuclear Cross-Polarization,” *ChemPhysChem*, vol. 20, no. 21, pp. 2830–2835, 2019, doi: 10.1002/cphc.201900723.
[100] O. Rybalko, S. Bowen, V. Zhurbenko, and J. H. Ardenkjær-Larsen, “Tunable 13C/1H dual channel matching circuit for dynamic nuclear polarization system with cross-polarization,” in *2016 46th European Microwave Conference (EuMC)*, Oct. 2016, pp. 1227–1230, doi: 10.1109/EuMC.2016.7824571.
[101] M. Batel, M. Krajewski, K. Weiss, O. With, A. Däpp, A. Hunkeler, M. Gimersky, K. P. Pruessmann, P. Boesiger, B. H. Meier, S. Kozerke, and M. Ernst, “A multi-sample 94GHz dissolution dynamic-nuclear-polarization system,” *J. Magn. Reson.*, vol. 214, pp. 166–174, 2012, doi: https://doi.org/10.1016/j.jmr.2011.11.002.
[102] S. Elliott, M. Ceillier, O. Cala, Q. Chappuis, S. Cousin, and S. Jannin, “No Title,” *Prep.*, 2021.
[103] S. J. Elliott, S. F. Cousin, Q. Chappuis, O. Cala, M. Ceillier, A. Bornet, and S. Jannin, “Dipolar order mediated \chem{^{1}H\to^{13}C} cross-polarization for dissolution-dynamic nuclear polarization,” *Magn. Reson.*, vol. 1, no. 1, pp. 89–96, 2020, doi: 10.5194/mr-1-89-2020.
[104] X.-A. Mao and C.-H. Ye, “Radiation Damping in a Simple Way,” *Concepts Magn. Reson.*, vol. 9, no. 3, pp. 173–187, Jan. 1997, doi: https://doi.org/10.1002/(SICI)1099-0534(1997)9:3<173::AID-CMR4>3.0.CO;2-W.
[105] K. J. Harris, A. Lupulescu, B. E. G. Lucier, L. Frydman, and R. W. Schurko, “Broadband adiabatic inversion pulses for cross polarization in wideline solid-state NMR spectroscopy,” *J. Magn. Reson.*, vol. 224, pp. 38–47, 2012, doi: https://doi.org/10.1016/j.jmr.2012.08.015.
[106] Q. Chappuis, S. Cousin, F. Mentink-Viger, A. Pinon, S. Elliott, O. Cala, and J. S, “No Title,” *Submitted*, 2020.
[107] S. F. J. Cox, V. Bouffard, and M. Goldman, “The coupling of two nuclear Zeeman reservoirs by the electronic spin-spin reservoir,” *J. Phys. C Solid State Phys.*, vol. 6, no. 5, 1973, doi: 10.1088/0022-3719/6/5/006.
[108] A. Gennaro, A. Karabanov, A. Potapov, and W. Köckenberger, “Heteronuclear DNP of 1H and 19F nuclei using BDPA as a polarizing agent,” *Phys. Chem. Chem. Phys.*, vol. 22, no. 15, pp. 7803–7816, 2020, doi: 10.1039/d0cp00892c.
[109] D. Guarin, S. Marhabaie, A. Rosso, D. Abergel, G. Bodenhausen, K. L. Ivanov, and D. Kurzbach, “Characterizing Thermal Mixing Dynamic Nuclear Polarization via Cross-Talk between Spin Reservoirs,” *J. Phys. Chem. Lett.*, vol. 8, no. 22, pp. 5531–5536, Nov. 2017, doi: 10.1021/acs.jpclett.7b02233.
[110] Q. Chappuis, J. Milani, B. Vuichoud, A. Bornet, A. D. Gossert, G. Bodenhausen, and S. Jannin, “Hyperpolarized water to study protein-ligand interactions,” *J. Phys. Chem. Lett.*, vol. 6, no. 9, pp. 1674–1678, 2015, doi: 10.1021/acs.jpclett.5b00403.
[111] N. N. Kuzma, P. Håkansson, M. Pourfathi, R. K. Ghosh, H. Kara, S. J. Kadlecek, G. Pileio, M. H. Levitt, and R. R. Rizi, “Lineshape-based polarimetry of dynamically-polarized 15N 2O in solid-state mixtures,” *J. Magn. Reson.*, vol. 234, pp. 90–94, 2013, doi: 10.1016/j.jmr.2013.06.008.
[112] N. S. Sullivan and R. V. Pound, “Nuclear-Spin-Lattice Relaxation of Solid Hydrogen at Low Temperatures,” *Phys. Rev. A.*, vol. 6, no. 3, pp. 1102–1107, 1972, doi: 10.1017/CBO9781107415324.004.
[113] M. M. Willmering, Z. L. Ma, M. A. Jenkins, J. F. Conley, and S. E. Hayes, “Enhanced NMR with Optical Pumping Yields 75As Signals Selectively from a Buried GaAs Interface,” *J. Am. Chem. Soc.*, vol. 139, no. 11, pp. 3930–3933, 2017, doi: 10.1021/jacs.6b08970.
[114] C. M. Edwards, D. Zhou, and N. S. Sullivan, “Unusual low-temperature effects on the NMR line shapes in solid hydrogen,” *Phys. Rev. B*, vol. 43, no. 9, pp. 6540–6542, 1986, doi: 10.1097/00042560-200105010-00007.
[115] N. N. Kuzma, P. Hakansson, M. Pourfathi, R. K. Hosh, H. Kara, S. J. Kadlecek, G. Pileio, M. H. Levitt, and R. R. Rizzi, “Lineshape-based polarimetry of dynamically-polarized 15N2O in solid-state mixtures,”

J. Magn. Reson., vol. 234, pp. 90–94, 2013, doi: 10.1038/jid.2014.371.

[116] P. Kuhns, O. Gonen, and J. S. Waugh, "Proton spin-spin and spin-lattice relaxation in CaSO4 · xH2O below 1 K," *J. Magn. Reson.*, vol. 82, no. 2, pp. 231–237, 1989, doi: 10.1016/0022-2364(89)90027-9.

[117] A. Abragam, M. Chapellier, J. F. Jacquinot, and M. Goldman, "Absorption lineshape of highly polarized nuclear spin systems," *J. Magn. Reson.*, vol. 10, no. 3, pp. 322–346, 1973, doi: 10.1016/0022-2364(73)90253-9.

[118] J. S. Waugh, O. Gonen, and P. Kuhns, "Fourier transform NMR at low temperatures," *J. Chem. Phys.*, vol. 86, no. 7, pp. 3816–3818, 1987, doi: 10.1063/1.451940.

[119] B. Aghelnejad, S. Marhabaie, M. Baudin, and G. Bodenhausen, "Spin Thermometry : A Straightforward Measure of Millikelvin Deuterium Spin Temperatures Achieved by Dynamic Nuclear Polarization Spin Thermometry : a Straightforward Measure of Millikelvin Deuterium Spin Temperatures Achieved by Dynamic Nuclear Polarizati," no. April, pp. 0–20, 2020, doi: 10.1021/acs.jpclett.0c00713.

[120] D. Mammoli, N. Salvi, J. Milani, R. Buratto, A. Bornet, A. A. Sehgal, E. Canet, P. Pelupessy, D. Carnevale, S. Jannin, and G. Bodenhausen, "Challenges in preparing, preserving and detecting para-water in bulk: overcoming proton exchange and other hurdles," *Phys. Chem. Chem. Phys.*, vol. 17, no. 40, pp. 26819–26827, 2015, doi: 10.1039/c5cp03350k.

[121] V. V. Krishnan and N. Murali, "Radiation damping in modern NMR experiments: Progress and challenges," *Prog. Nucl. Magn. Reson. Spectrosc.*, vol. 68, pp. 41–57, 2013, doi: 10.1016/j.pnmrs.2012.06.001.

[122] E. M. M. Weber, D. Kurzbach, and D. Abergel, "A DNP-hyperpolarized solid-state water NMR MASER: observation and qualitative analysis," *Phys. Chem. Chem. Phys.*, vol. 21, no. 38, pp. 21278–21286, 2019, doi: 10.1039/c9cp03334c.

[123] C. P. Grey, L. Emsley, and M. A. Hope, "A Magic Angle Spinning Activated 17O DNP Raser Michael," pp. 0–4, 2021, doi: 10.1021/acs.jpclett.0c03457.

[124] M. T. Pçschko, B. Vuichoud, J. Milani, A. A. Bornet, M. T. Pöschko, B. Vuichoud, J. Milani, A. A. Bornet, M. Bechmann, G. Bodenhausen, S. Jannin, and N. Müller, "Spin Noise Detection of Nuclear Hyperpolarization at 1.2 K," *ChemPhysChem*, vol. 16, no. 18, pp. 3859–3864, Dec. 2015, doi: https://doi.org/10.1002/cphc.201500805.

[125] A. Bornet, J. Milani, B. Vuichoud, A. J. Perez Linde, G. Bodenhausen, S. Jannin, A. J. P. Linde, G. Bodenhausen, and S. Jannin, "Microwave frequency modulation to enhance Dissolution Dynamic Nuclear Polarization," *Chem. Phys. Lett.*, vol. 602, pp. 63–67, 2014, doi: 10.1016/j.cplett.2014.04.013.

[126] Y. Hovav, A. Feintuch, S. Vega, and D. Goldfarb, "Dynamic nuclear polarization using frequency modulation at 3.34T," *J. Magn. Reson.*, vol. 238, pp. 94–105, Jan. 2014, doi: 10.1016/j.jmr.2013.10.025.

[127] S. Jannin, A. Comment, F. Kurdzesau, J. A. Konter, P. Hautle, B. Van Den Brandt, and J. J. Van Der Klink, "A 140 GHz prepolarizer for dissolution dynamic nuclear polarization," *J. Chem. Phys.*, vol. 128, no. 24, p. 241102, 2008, doi: 10.1063/1.2951994.

[128] F. Jähnig, G. Kwiatkowski, A. Däpp, A. Hunkeler, B. H. Meier, S. Kozerke, and M. Ernst, "Dissolution DNP using trityl radicals at 7 T field," *Phys. Chem. Chem. Phys.*, vol. 19, no. 29, pp. 19196–19204, 2017, doi: 10.1039/c7cp03633g.

[129] S. Jannin, A. Bornet, R. Melzi, and G. Bodenhausen, "High field dynamic nuclear polarization at 6.7 T: Carbon-13 polarization above 70% within 20 min," *Chem. Phys. Lett.*, vol. 549, pp. 99–102, 2012, doi: 10.1016/j.cplett.2012.08.017.

[130] J. H. Ardenkjær-Larsen, S. Bowen, J. R. Petersen, O. Rybalko, M. S. Vinding, M. Ullisch, and N. C. Nielsen, "Cryogen-free dissolution dynamic nuclear polarization polarizer operating at 3.35 T, 6.70 T, and 10.1 T," *Magn. Reson. Med.*, vol. 81, no. 3, pp. 2184–2194, Mar. 2019, doi: 10.1002/mrm.27537.

[131] F. Kurdzesau, B. Van Den Brandt, A. Comment, P. Hautle, S. Jannin, J. J. Van Der Klink, and J. A. Konter, "Dynamic nuclear polarization of small labelled molecules in frozen water-alcohol solutions," *J. Phys. D. Appl. Phys.*, vol. 41, no. 15, pp. 155506–10, 2008, doi: 10.1088/0022-3727/41/15/155506.

[132] J. H. Ardenkjaer-Larsen, S. MacHoll, and H. Jóhannesson, "Dynamic nuclear polarization with trityls at 1.2 K," *Appl. Magn. Reson.*, vol. 34, no. 3–4, pp. 509–522, 2008, doi: 10.1007/s00723-008-0134-4.

[133] L. L. Lumata, S. J. Ratnakar, A. K. Jindal, M. E. Merritt, A. Comment, C. R. Malloy, A. D. Sherry, Z. Kovacs, S. James Ratnakar, A. K. Jindal, M. E. Merritt, A. Comment, C. R. Malloy, A. D. Sherry, Z. Kovacs, S. J. Ratnakar, A. K. Jindal, M. E. Merritt, A. Comment, C. R. Malloy, A. D. Sherry, and Z. Kovacs, "BDPA: An Efficient Polarizing Agent for Fast Dissolution Dynamic Nuclear Polarization NMR," *Natl. Inst. Heal.*, vol. 17, no. 39, pp. 10825–7, Sep. 2011, doi: 10.1002/chem.201102037.BDPA.

[134] A. J. Perez Linde, "Application of cross polarisation techniques to dynamic nuclear polarisation dissolution experiments," no. November, 2010, [Online]. Available: http://etheses.nottingham.ac.uk/1417/.

[135] M. Batel, A. Däpp, A. Hunkeler, B. H. Meier, S. Kozerke, and M. Ernst, "Cross-polarization for dissolution dynamic nuclear polarization," *Phys. Chem. Chem. Phys.*, vol. 16, no. 39, pp. 21407–21416, 2014, doi: 10.1039/c4cp02696a.

[136] A. Dey, B. Charrier, E. Martineau, C. Deborde, E. Gandriau, A. Moing, D. Jacob, D. Eshchenko, M. Schnell, R. Melzi, D. Kurzbach, M. Ceillier, Q. Chappuis, S. F. Cousin, J. G. Kempf, S. Jannin, J.-N. Dumez, and P. Giraudeau, "Hyperpolarized NMR Metabolomics at Natural 13 C Abundance," *Anal. Chem.*, vol. 92, pp. 14867–14871, 2020, doi: 10.1021/acs.analchem.0c03510.

[137] J. N. Dumez, J. Milani, B. Vuichoud, A. Bornet, J. Lalande-Martin, I. Tea, M. Yon, M. Maucourt, C. Deborde, A. Moing, L. Frydman, G. Bodenhausen, S. Jannin, and P. Giraudeau, "Hyperpolarized NMR of plant and cancer cell extracts at natural abundance," *Analyst*, vol. 140, no. 17, pp. 5860–5863, 2015, doi: 10.1039/c5an01203a.

[138] B. Vuichoud, J. Milani, A. Bornet, R. Melzi, S. Jannin, and G. Bodenhausen, "Hyperpolarization of deuterated metabolites via remote cross-polarization and dissolution dynamic nuclear polarization," *J. Phys.*

Chem. B, vol. 118, no. 5, pp. 1411–1415, 2014, doi: 10.1021/jp4118776.

[139] S. J. Elliott, S. F. Cousin, Q. Chappuis, O. Cala, M. Ceillier, A. Bornet, and S. Jannin, "Dipolar order mediated 1H → 13C cross-polarization for dissolution-dynamic nuclear polarization," *Magn. Reson.*, vol. 1, no. 1, pp. 89–96, 2020, doi: 10.5194/mr-1-89-2020.

[140] A. Bornet, "De l'usage des protons hyperpolarisés pour augmenter la sensibilite de la RMN," vol. 6581, 2015.

[141] A. Kiswandhi, P. Niedbalski, C. Parish, P. Kaur, A. Martins, L. Fidelino, C. Khemtong, L. Song, A. D. Sherry, and L. Lumata, "Impact of Ho3+-doping on 13C dynamic nuclear polarization using trityl OX063 free radical," *Phys. Chem. Chem. Phys.*, vol. 18, no. 31, pp. 21351–21359, 2016, doi: 10.1039/c6cp03954e.

[142] R. Rogawski, I. V. Sergeyev, Y. Zhang, T. H. Tran, Y. Li, L. Tong, and A. E. McDermott, "NMR Signal Quenching from Bound Biradical Affinity Reagents in DNP Samples," *J. Phys. Chem. B*, vol. 121, no. 48, pp. 10770–10781, 2017, doi: 10.1021/acs.jpcb.7b08274.

[143] S. Hediger, D. Lee, F. Mentink-Vigier, and G. De Paëpe, *MAS-DNP enhancements: Hyperpolarization, depolarization, and absolute sensitivity*, vol. 7, no. 4. 2018.

[144] S. Elliott, I. Koptyug, and S. Jannin, "No Title," *Prep.*, 2021.

[145] R. M. Malinowski, K. W. Lipsø, M. H. Lerche, and J. H. Ardenkjær-Larsen, "Dissolution Dynamic Nuclear Polarization capability study with fluid path," *J. Magn. Reson.*, vol. 272, pp. 141–146, 2016, doi: 10.1016/j.jmr.2016.09.015.

[146] A. Capozzi, M. Karlsson, J. R. Petersen, M. H. Lerche, and J. H. Ardenkjaer-Larsen, "Liquid-State 13C Polarization of 30% through Photoinduced Nonpersistent Radicals," *J. Phys. Chem. C*, vol. 122, no. 13, pp. 7432–7443, 2018, doi: 10.1021/acs.jpcc.8b01482.

[147] A. C. Pinon, A. Capozzi, and J. H. Ardenkjær-Larsen, "Hyperpolarized water through dissolution dynamic nuclear polarization with UV-generated radicals," *Commun. Chem. 2020 31*, vol. 3, no. 1, pp. 1–9, 2020, doi: 10.1038/s42004-020-0301-6.

[148] M. Krajewski, P. Wespi, J. Busch, L. Wissmann, G. Kwiatkowski, J. Steinhauser, M. Batel, M. Ernst, and S. Kozerke, "A multisample dissolution dynamic nuclear polarization system for serial injections in small animals," *Magn. Reson. Med.*, vol. 77, no. 2, pp. 904–910, 2017, doi: 10.1002/mrm.26147.

[149] T. Cheng, A. P. Gaunt, I. Marco-Rius, M. Gehrung, A. P. Chen, J. J. Klink, A. Comment, I. Marco-Rius, M. Gehrung, A. P. Chen, J. J. van der Klink, and A. Comment, "A multisample 7 T dynamic nuclear polarization polarizer for preclinical hyperpolarized MR," *NMR Biomed.*, no. October 2019, pp. 1–10, Jan. 2020, doi: 10.1002/nbm.4264.

[150] S. Bowen and J. H. Ardenkjaer-Larsen, "Enhanced performance large volume dissolution-DNP," *J. Magn. Reson.*, vol. 240, pp. 90–94, 2014, doi: 10.1016/j.jmr.2014.01.009.

[151] J. Jain, S. Dey, L. Muralidharan, A. M. Leach, and J. H. Ardenkjaer-Larsen, "Jet Impingement Melting With Vaporization: A Numerical Study," in *Heat Transfer: Volume 2*, Jan. 2008, vol. 2, pp. 559–567, doi: 10.1115/HT2008-56148.

[152] N. (US) Jan Henrik Ardenkjaer-larsen, Amersham (GB); David Dietrich, Niskayuna, NY (US); Karl Andreas Gram, Oslo (NO); Andrew M. Leach, Clifton Park, NY (US); Peter Miller, New London, CT (US); Eric J. Telfeyan, Guilderland, NY (US); Mikkel Thaning, Oslo (NO); Da, "Patent - NOZZLE FOR DNP POLARIZER," vol. 1, no. 5, pp. 739–740, 2011.

[153] D. M. Wilson, K. R. Keshari, P. E. Z. Larson, A. P. Chen, S. Hu, M. Van Criekinge, R. Bok, S. J. Nelson, J. M. MacDonald, D. B. Vigneron, and J. Kurhanewicz, "Multi-compound polarization by DNP allows simultaneous assessment of multiple enzymatic activities in vivo," *J. Magn. Reson.*, vol. 205, no. 1, pp. 141–147, 2010, doi: 10.1016/j.jmr.2010.04.012.

[154] A. Bornet, M. Maucourt, C. Deborde, D. Jacob, J. Milani, B. Vuichoud, X. Ji, J. N. Dumez, A. Moing, G. Bodenhausen, S. Jannin, and P. Giraudeau, "Highly Repeatable Dissolution Dynamic Nuclear Polarization for Heteronuclear NMR Metabolomics," *Anal. Chem.*, vol. 88, no. 12, pp. 6179–6183, 2016, doi: 10.1021/acs.analchem.6b01094.

[155] X. Ji, A. A. Bornet, B. Vuichoud, J. Milani, D. Gajan, A. J. A. J. Rossini, L. Emsley, G. Bodenhausen, and S. Jannin, "Transportable hyperpolarized metabolites," *Nat. Commun.*, vol. 8, no. 1, p. 13975, Apr. 2017, doi: 10.1038/ncomms13975.

[156] J. Granwehr, R. Panek, J. Leggett, and W. Köckenberger, "Quantifying the transfer and settling in NMR experiments with sample shuttling," *J. Chem. Phys.*, vol. 132, no. 24, p. 244507, Jun. 2010, doi: 10.1063/1.3446804.

[157] T. Harris, C. Bretschneider, and L. Frydman, "Dissolution DNP NMR with solvent mixtures: Substrate concentration and radical extraction," *J. Magn. Reson.*, vol. 211, no. 1, pp. 96–100, 2011, doi: 10.1016/j.jmr.2011.04.001.

[158] S. G. J. Van Meerten, G. E. Janssen, and A. P. M. Kentgens, "Experiments Rapid-melt DNP for Multidimensional and Heteronuclear High-field NMR Experiments," *J. Magn. Reson.*, p. 106656, 2019, doi: 10.1016/j.jmr.2019.106656.

[159] S. Bowen and C. Hilty, "Rapid sample injection for hyperpolarized NMR spectroscopy," *Phys. Chem. Chem. Phys.*, vol. 12, no. 22, pp. 5766–5770, May 2010, doi: 10.1039/c002316g.

[160] S. Katsikis, I. Marin-Montesinos, M. Pons, C. Ludwig, and U. L. Günther, "Improved Stability and Spectral Quality in Ex Situ Dissolution DNP Using an Improved Transfer Device," *Appl. Magn. Reson.*, vol. 46, no. 7, pp. 723–729, 2015, doi: 10.1007/s00723-015-0680-5.

[161] G. Olsen, E. Markhasin, O. Szekely, C. Bretschneider, and L. Frydman, "Optimizing water hyperpolarization and dissolution for sensitivity-enhanced 2D biomolecular NMR," *J. Magn. Reson.*, vol. 264, pp. 49–58, 2016, doi: 10.1016/j.jmr.2016.01.005.

[162] K. A. Triplett, S. M. Ghiaasiaan, S. I. Abdel-Khalik, and D. L. Sadowski, "Gas–liquid two-phase flow in microchannels Part I: two-phase flow patterns," *Int. J. Multiph. Flow*, vol. 25, no. 3, pp. 377–394, Apr. 1999, doi: 10.1016/S0301-9322(98)00054-8.

[163] J. Kim, J. D. O'Neill, N. V. Dorrello, M. Bacchetta,

and G. Vunjak-Novakovic, “Targeted delivery of liquid microvolumes into the lung,” *Proc. Natl. Acad. Sci.*, vol. 112, no. 37, pp. 11530–11535, 2015, doi: 10.1073/pnas.1512613112.

[164] H. Fujioka and J. B. Grotberg, “The steady propagation of a surfactant-laden liquid plug in a two-dimensional channel,” *Phys. Fluids*, vol. 17, no. 8, pp. 1–17, 2005, doi: 10.1063/1.1948907.

[165] K. J. Cassidy, N. Gavriely, and J. B. Grotberg, “Liquid Plug Flow in Straight and Bifurcating Tubes,” *J. Biomech. Eng.*, vol. 123, no. 6, p. 580, 2002, doi: 10.1115/1.1406949.

[166] J. C. Magniez, M. Baudoin, C. Liu, and F. Zoueshtiagh, “Dynamics of liquid plugs in prewetted capillary tubes: From acceleration and rupture to deceleration and airway obstruction,” *Soft Matter*, vol. 12, no. 42, pp. 8710–8717, 2016, doi: 10.1039/c6sm01463a.

[167] H. Y. Chen and C. Hilty, “Implementation and Characterization of Flow Injection in Dissolution Dynamic Nuclear Polarization NMR Spectroscopy,” *ChemPhysChem*, vol. 16, no. 12, pp. 2646–2652, Aug. 2015, doi: 10.1002/cphc.201500292.

[168] H. Y. Chen and C. Hilty, “Hyperpolarized Hadamard spectroscopy using flow NMR,” *Anal. Chem.*, vol. 85, no. 15, pp. 7385–7390, Aug. 2013, doi: 10.1021/ac401293n.

[169] J. E. Austin and J. R. Palfrey, “Mixing of Miscible but Dissimilar Liquids in Serial Flow in a Pipeline,” *Proc. Inst. Mech. Eng.*, vol. 178, no. 1, pp. 377–389, Jun. 1963, doi: 10.1177/002034836317800160.

[170] L. Zhao, J. Derksen, and R. Gupta, “Simulations of axial mixing of liquids in a long horizontal pipe for industrial applications,” *Energy and Fuels*, vol. 24, no. 11, pp. 5844–5850, 2010, doi: 10.1021/ef100846r.

[171] A. R. Patrachari and A. H. Johannes, “A conceptual framework to model interfacial contamination in multiproduct petroleum pipelines,” *Int. J. Heat Mass Transf.*, vol. 55, no. 17–18, pp. 4613–4620, 2012, doi: 10.1016/j.ijheatmasstransfer.2012.04.017.

[172] G. He, M. Lin, B. Wang, Y. Liang, and Q. Huang, “Experimental and numerical research on the axial and radial concentration distribution feature of miscible fluid interfacial mixing process in products pipeline for industrial applications,” *Int. J. Heat Mass Transf.*, vol. 127, pp. 728–745, 2018, doi: 10.1016/j.ijheatmasstransfer.2018.08.080.

[173] E. Chiavazza, E. Kubala, C. V. Gringeri, S. Düwel, M. Durst, R. F. Schulte, and M. I. Menzel, “Earth’s magnetic field enabled scalar coupling relaxation of 13C nuclei bound to fast-relaxing quadrupolar 14N in amide groups,” *J. Magn. Reson.*, vol. 227, pp. 35–38, 2013, doi: 10.1016/j.jmr.2012.11.016.

[174] G. D. Reed, C. Von Morze, R. Bok, B. L. Koelsch, M. Van Criekinge, K. J. Smith, H. Shang, P. E. Z. Larson, J. Kurhanewicz, and D. B. Vigneron, “High resolution 13C MRI with hyperpolarized urea: In vivo T 2 mapping and 15N labeling effects,” *IEEE Trans. Med. Imaging*, vol. 33, no. 2, pp. 362–371, 2014, doi: 10.1109/TMI.2013.2285120.

[175] H. Shang, T. Skloss, C. von Morze, L. Carvajal, M. Van Criekinge, E. Milshteyn, P. E. Z. Larson, R. E. Hurd, and D. B. Vigneron, “Handheld electromagnet carrier for transfer of hyperpolarized carbon-13 samples,” *Magn. Reson. Med.*, vol. 75, no. 2, pp. 917–922, Feb. 2016, doi: 10.1002/mrm.25657.

[176] P. Berthault, C. Boutin, C. Martineau-Corcos, and G. Carret, “Use of dissolved hyperpolarized species in NMR: practical considerations,” *Prog. Nucl. Magn. Reson. Spectrosc.*, vol. 118–119, pp. 74–90, 2020, doi: 10.1016/j.pnmrs.2020.03.002.

[177] A. S. Kiryutin, B. A. Rodin, A. V. Yurkovskaya, K. L. Ivanov, D. Kurzbach, S. Jannin, D. Guarin, D. Abergel, and G. Bodenhausen, “Transport of hyperpolarized samples in dissolution-DNP experiments,” *Phys. Chem. Chem. Phys.*, vol. 21, no. 25, pp. 13696–13705, 2019, doi: 10.1039/c9cp02600b.

[178] A. Abragam and A. Abragam, *The principles of nuclear magnetism*, no. 32. Oxford university press, 1961.

[179] J. Kowalewski and L. Mäler, *Nuclear Spin Relaxation in Liquids: Theory, Experiments and Applications*. 2006.

[180] J. Cavanagh, W. J. Fairbrother, A. G. Palmer III, M. Rance, and N. J. Skelton, *Protein NMR Spectroscopy: Principles and Practice*. 1995.

[181] M. H. Levitt, *Spin Dynamics: Basics of Nuclear Magnetic Resonance*. 2001.

[182] P. J. Hore, *Nuclear Magnetic Resonance*. 1995.

[183] P. J. Hore, J. A. Jones, and S. Wimperis, *The Toolkit: How Pulse Sequences Work*. 2015.

[184] N. Bloembergen, “On the interaction of nuclear spins in a crystalline lattice,” *Physica*, vol. XV, no. 3–4, pp. 176–219, 1949, doi: 10.1142/9789812795809_0005.

[185] C. Ramanathan, “Dynamic Nuclear Polarization and Spin Diffusion in Nonconducting Solids,” *Appl. Magn. Reson.*, vol. 34, pp. 409–421, 2008, doi: 10.1007/s00723-008-0123-7.

[186] A. J. Pell, G. Pintacuda, and C. P. Grey, “Paramagnetic NMR in solution and the solid state,” *Prog. Nucl. Magn. Reson. Spectrosc.*, vol. 111, pp. 1–271, 2019, doi: 10.1016/j.pnmrs.2018.05.001.

[187] Y. Hovav, A. Feintuch, and S. Vega, “Theoretical aspects of dynamic nuclear polarization in the solid state - Spin temperature and thermal mixing,” *Phys. Chem. Chem. Phys.*, vol. 15, no. 1, pp. 188–203, 2013, doi: 10.1039/c2cp42897k.

[188] A. Karabanov, G. Kwiatkowski, and W. Köckenberger, “Spin dynamic simulations of solid effect DNP: The role of the relaxation superoperator,” *Mol. Phys.*, vol. 112, no. 14, pp. 1838–1854, 2014, doi: 10.1080/00268976.2014.884287.

[189] D. Wiśniewski, A. Karabanov, I. Lesanovsky, and W. Köckenberger, “Solid effect DNP polarization dynamics in a system of many spins,” *J. Magn. Reson.*, vol. 264, pp. 30–38, 2016, doi: 10.1016/j.jmr.2016.01.016.

[190] G. R. Khutsishvili, “Spin diffusion,” *Sov. Phys. Uspekhi*, vol. 8, no. 6, pp. 743–769, 1966.

[191] R. L. R. R. L. R. R. L. Vold and R. L. R. R. L. R. R. L. Vold, “Nuclear magnetic relaxation in coupled spin systems,” *Prog. Nucl. Magn. Reson. Spectrosc.*, vol. 12, no. 2, pp. 79–133, 1978, doi: https://doi.org/10.1016/0079-6565(78)80004-1.

[192] L. G. Werbelow and D. M. Grant, “Carbon-13 relaxation in multispin systems of the type AXn,” *J. Chem. Phys.*, vol. 63, no. 1, pp. 544–556, 1975, doi: 10.1063/1.431085.

[193] G. E. Pake, “Nuclear Resonance Absorption in Hydrated Crystals: Fine Structure of the Proton Line,” *J. Chem. Phys.*, vol. 16, no. 4, pp. 327–336, 1948.
[194] Z. H. Endre, B. E. Chapman, and P. W. Kuchel, “Intra-erythrocyte microviscosity and diffusion of specifically labelled [glycyl-alpha-13C]glutathione by using 13C n.m.r,” *Biochem. J.*, vol. 216, no. 3, pp. 655–660, Dec. 1983, doi: 10.1042/bj2160655.
[195] B. Erriah and S. J. Elliott, “Experimental evidence for the role of paramagnetic oxygen concentration on the decay of long-lived nuclear spin order,” *RSC Adv.*, vol. 9, no. 40, pp. 23418–23424, 2019, doi: 10.1039/C9RA03748A.
[196] K. W. Lipsø, S. Bowen, O. Rybalko, and J. H. Ardenkjær-Larsen, “Large dose hyperpolarized water with dissolution-DNP at high magnetic field,” *J. Magn. Reson.*, vol. 274, pp. 65–72, 2017, doi: 10.1016/j.jmr.2016.11.008.
[197] D. Shishmarev, P. W. Kuchel, G. Pagès, A. J. Wright, R. L. Hesketh, F. Kreis, and K. M. Brindle, “Glyoxalase activity in human erythrocytes and mouse lymphoma, liver and brain probed with hyperpolarized 13C-methylglyoxal,” *Commun. Biol.*, vol. 1, no. 1, p. 232, 2018, doi: 10.1038/s42003-018-0241-1.
[198] D. Kruk, R. Meier, and E. A. Rössler, “Nuclear magnetic resonance relaxometry as a method of measuring translational diffusion coefficients in liquids,” *Phys. Rev. E - Stat. Nonlinear, Soft Matter Phys.*, vol. 85, no. 2, pp. 1–5, 2012, doi: 10.1103/PhysRevE.85.020201.
[199] B. Borah and R. G. Bryant, “NMR relaxation dispersion in an aqueous nitroxide system,” *J. Chem. Phys.*, vol. 75, no. 7, pp. 3297–3300, 1981, doi: 10.1063/1.442480.
[200] D. Baudouin, H. A. Van Kalkeren, A. Bornet, B. Vuichoud, L. Veyre, M. Cavaillès, M. Schwarzwälder, W.-C. C. Liao, D. Gajan, G. Bodenhausen, L. Emsley, A. Lesage, S. Jannin, C. Copéret, and C. Thieuleux, “Cubic three-dimensional hybrid silica solids for nuclear hyperpolarization,” *Chem. Sci.*, vol. 7, no. 11, pp. 6846–6850, Oct. 2016, doi: 10.1039/c6sc02055k.
[201] R. Nepravishta, B. Yu, and J. Iwahara, “Hydrogen-exchange kinetics studied through analysis of self-decoupling of nuclear magnetic resonance,” *J. Magn. Reson.*, vol. 312, p. 106687, 2020, doi: 10.1016/j.jmr.2020.106687.
[202] P. Bernatowicz, D. Kubica, M. Ociepa, A. Wodyński, and A. Gryff-Keller, “Scalar relaxation of the second kind. A potential source of information on the dynamics of molecular movements. 4. Molecules with collinear C-H and C-Br bonds,” *J. Phys. Chem. A*, vol. 118, no. 23, pp. 4063–4070, 2014, doi: 10.1021/jp5037298.
[203] J. N. Dumez, P. Håkansson, S. Mamone, B. Meier, G. Stevanato, J. T. Hill-Cousins, S. S. Roy, R. C. D. Brown, G. Pileio, and M. H. Levitt, “Theory of long-lived nuclear spin states in methyl groups and quantum-rotor induced polarisation,” *J. Chem. Phys.*, vol. 142, no. 4, 2015, doi: 10.1063/1.4906273.
[204] T. E. Burke and S. I. Chan, “Nuclear spin relaxation in the presence of internal rotation II. Nuclear-spin-internal rotational coupling in benzotrifluoride and hexafluorobutyne-2,” *J. Magn. Reson.*, vol. 2, no. 2, pp. 120–140, 1970, doi: 10.1016/0022-2364(70)90063-6.
[205] G. B. Matson, “Methyl NMR relaxation: The effects of spin rotation and chemical shift anisotropy mechanisms,” *J. Chem. Phys.*, vol. 67, no. 11, pp. 5152–5161, 1977, doi: 10.1063/1.434744.
[206] T. E. Bull, “Extended diffusion of a symmetric top molecule with internal rotation,” *J. Chem. Phys.*, vol. 65, no. 11, pp. 4802–4815, 1976, doi: 10.1063/1.432951.
[207] A. S. Dubin and S. I. Chan, “Nuclear-Spin—Internal-Rotation Coupling,” *J. Chem. Phys.*, vol. 46, no. 11, pp. 4533–4535, 1967, doi: 10.1063/1.1840583.
[208] B. F. Melton, V. L. Pollak, T. W. Mayes, and B. L. Willis, “Condition for Sudden Passage in the Earth’s-Field NMR Technique,” *J. Magn. Reson. Ser. A*, vol. 117, no. 2, pp. 164–170, 1995, doi: 10.1006/jmra.1995.0732.
[209] M. Carravetta, O. G. Johannessen, and M. H. Levitt, “Beyond the T1 Limit: Singlet Nuclear Spin States in Low Magnetic Fields,” *Phys. Rev. Lett.*, vol. 92, no. 15, p. 153003, Apr. 2004, doi: 10.1103/PhysRevLett.92.153003.
[210] J. W. Blanchard and D. Budker, “Zero-to ultralow-field NMR,” *eMagRes*, vol. 5, no. 3, pp. 1395–1410, 2016, doi: 10.1002/9780470034590.emrstm1369.
[211] C. R. Bowers and D. P. Weitekamp, “Parahydrogen and Synthesis Allow Dramatically Enhanced Nuclear Alignment,” *J. Am. Chem. Soc.*, vol. 109, no. 18, pp. 5541–5542, 1987, doi: 10.1021/ja00252a049.
[212] K. Miesel, K. L. Ivanov, A. V. Yurkovskaya, and H. M. Vieth, “Coherence transfer during field-cycling NMR experiments,” *Chem. Phys. Lett.*, vol. 425, no. 1–3, pp. 71–76, 2006, doi: 10.1016/j.cplett.2006.05.025.
[213] J. Eills, J. W. Blanchard, T. Wu, C. Bengs, J. Hollenbach, D. Budker, and M. H. Levitt, “Polarization transfer via field sweeping in parahydrogen-enhanced nuclear magnetic resonance,” *J. Chem. Phys.*, vol. 150, no. 17, p. 174202, 2019, doi: 10.1063/1.5089486.
[214] H. Zeng, Y. Lee, and C. Hilty, “Quantitative rate determination by dynamic nuclear polarization enhanced NMR of a diels-alder reaction,” *Anal. Chem.*, vol. 82, no. 21, pp. 8897–8902, 2010, doi: 10.1021/ac101670n.
[215] Y. Lee, G. S. Heo, H. F. Zeng, K. L. Wooley, and C. Hilty, “Detection of living anionic species in polymerization reactions using hyperpolarized NMR,” *J. Am. Chem. Soc.*, vol. 135, no. 12, pp. 4636–4639, 2013, doi: 10.1021/ja4001008.
[216] C. H. Chen, W. C. Shih, and C. Hilty, “In situ determination of tacticity, deactivation, and kinetics in [rac -(C2H4(1-Indenyl)2)ZrMe][B(C6F5)4] and [Cp2ZrMe][B(C6F5)4]-Catalyzed Polymerization of 1-Hexene Using 13C hyperpolarized nmr,” *J. Am. Chem. Soc.*, vol. 137, no. 21, pp. 6965–6971, 2015, doi: 10.1021/jacs.5b04479.
[217] M. J. Moure, Y. Zhuo, G. J. Boons, and J. H. Prestegard, “Perdeuterated and 13C-enriched myo-inositol for DNP assisted monitoring of enzymatic phosphorylation by inositol-3-kinase,” *Chem. Commun.*, vol. 53, no. 92, pp. 12398–12401, 2017, doi: 10.1039/c7cc07023c.
[218] S. Bowen and C. Hilty, “Time-resolved dynamic

nuclear polarization enhanced NMR spectroscopy," *Angew. Chemie - Int. Ed.*, vol. 47, no. 28, pp. 5235–5237, 2008, doi: 10.1002/anie.200801492.

[219] Y. Lee, H. Zeng, S. Ruedisser, A. D. Gossert, and C. Hilty, "Nuclear magnetic resonance of hyperpolarized fluorine for characterization of protein-ligand interactions," *J. Am. Chem. Soc.*, vol. 134, no. 42, pp. 17448–17451, 2012, doi: 10.1021/ja308437h.

[220] Y. Kim and C. Hilty, *Applications of Dissolution-DNP for NMR Screening*, 1st ed., vol. 615. Elsevier Inc., 2019.

[221] Y. Kim and C. Hilty, "Affinity screening using competitive binding with fluorine-19 hyperpolarized ligands," *Angew. Chemie - Int. Ed.*, vol. 54, no. 16, pp. 4941–4944, 2015, doi: 10.1002/anie.201411424.

[222] P. R. Jensen, M. Karlsson, M. H. Lerche, and S. Meier, "Real-Time DNP** NMR Observations of Acetic Acid Uptake, Intracellular Acidification, and of Consequences for Glycolysis and Alcoholic Fermentation in Yeast," *Chem. - A Eur. J.*, vol. 19, no. 40, pp. 13288–13293, 2013, doi: 10.1002/chem.201302429.

[223] H. Zeng, S. Bowen, and C. Hilty, "Sequentially acquired two-dimensional NMR spectra from hyperpolarized sample," *J. Magn. Reson.*, vol. 199, no. 2, pp. 159–165, Aug. 2009, doi: 10.1016/j.jmr.2009.04.011.

[224] P. Giraudeau and L. Frydman, "Ultrafast 2D NMR: An emerging tool in analytical spectroscopy," *Annu. Rev. Anal. Chem.*, vol. 7, pp. 129–161, 2014, doi: 10.1146/annurev-anchem-071213-020208.

[225] L. Frydman, T. Scherf, and A. Lupulescu, "The acquisition of multidimensional NMR spectra within a single scan," *Proc. Natl. Acad. Sci. U. S. A.*, vol. 99, no. 25, pp. 15858–15862, 2002, doi: 10.1073/pnas.252644399.

[226] J. Dumez, "Spatial encoding and spatial selection methods in high-resolution NMR spectroscopy," *Prog. Nucl. Magn. Reson. Spectrosc.*, 2018, doi: 10.1016/j.pnmrs.2018.08.001.

[227] L. Frydman and D. Blazina, "Ultrafast two-dimensional nuclear magnetic resonance spectroscopy of hyperpolarized solutions," *Nat. Phys.*, vol. 3, no. 6, pp. 415–419, Jun. 2007, doi: 10.1038/nphys597.

[228] M. Mishkovsky and L. Frydman, "Progress in hyperpolarized ultrafast 2D NMR spectroscopy," *ChemPhysChem*, vol. 9, no. 16, pp. 2340–2348, 2008, doi: 10.1002/cphc.200800461.

[229] P. Giraudeau, Y. Shrot, and L. Frydman, "Multiple ultrafast, broadband 2D NMR spectra of hyperpolarized natural products," *J. Am. Chem. Soc.*, vol. 131, no. 39, pp. 13902–13903, Oct. 2009, doi: 10.1021/ja905096f.

[230] G. Zhang, S. Ahola, M. H. Lerche, V. V. Telkki, and C. Hilty, "Identification of Intracellular and Extracellular Metabolites in Cancer Cells Using 13C Hyperpolarized Ultrafast Laplace NMR," *Anal. Chem.*, vol. 90, no. 18, pp. 11131–11137, 2018, doi: 10.1021/acs.analchem.8b03096.

[231] S. Ahola, V. V. Zhivonitko, O. Mankinen, G. Zhang, A. M. Kantola, H. Y. Chen, C. Hilty, I. V. Koptyug, and V. V. Telkki, "Ultrafast multidimensional Laplace NMR for a rapid and sensitive chemical analysis," *Nat. Commun.*, vol. 6, pp. 1–7, 2015, doi: 10.1038/ncomms9363.

[232] L. Guduff, D. Kurzbach, C. van Heijenoort, D. Abergel, and J. N. Dumez, "Single-Scan 13C Diffusion-Ordered NMR Spectroscopy of DNP-Hyperpolarised Substrates," *Chem. - A Eur. J.*, vol. 23, no. 66, pp. 16722–16727, Nov. 2017, doi: 10.1002/chem.201703300.

[233] R. Panek, J. Granwehr, J. Leggett, and W. Köckenberger, "Slice-selective single scan proton COSY with dynamic nuclear polarisation," *Phys. Chem. Chem. Phys.*, vol. 12, no. 22, p. 5771, May 2010, doi: 10.1039/c002710n.

[234] P. Schanda and B. Brutscher, "Very fast two-dimensional NMR spectroscopy for real-time investigation of dynamic events in proteins on the time scale of seconds," *J. Am. Chem. Soc.*, vol. 127, no. 22, pp. 8014–8015, 2005, doi: 10.1021/ja051306e.

[235] D. Kurzbach, E. Canet, A. G. Flamm, A. Jhajharia, E. M. M. Weber, R. Konrat, and G. Bodenhausen, "Investigation of Intrinsically Disordered Proteins through Exchange with Hyperpolarized Water," *Angew. Chemie - Int. Ed.*, vol. 56, no. 1, pp. 389–392, 2017, doi: 10.1002/anie.201608903.

[236] Y. Wang, J. Kim, and C. Hilty, "Determination of protein-ligand binding modes using fast multi-dimensional NMR with hyperpolarization," *Chem. Sci.*, vol. 11, no. 23, pp. 5935–5943, 2020, doi: 10.1039/d0sc00266f.

[237] P. Kadeřávek, F. Ferrage, G. Bodenhausen, and D. Kurzbach, "High-Resolution NMR of Folded Proteins in Hyperpolarized Physiological Solvents," *Chem. - A Eur. J.*, vol. 24, no. 51, pp. 13418–13423, 2018, doi: 10.1002/chem.201802885.

[238] S. J. Elliott, B. Meier, B. Vuichoud, G. Stevanato, L. J. Brown, J. Alonso-Valdesueiro, L. Emsley, S. Jannin, and M. H. Levitt, "Hyperpolarized long-lived nuclear spin states in monodeuterated methyl groups," *Phys. Chem. Chem. Phys.*, vol. 20, no. 15, pp. 9755–9759, 2018, doi: 10.1039/C8CP00253C.

[239] A. Bornet, S. Jannin, J. A. Konter, P. Hautle, B. Van Den Brandt, and G. Bodenhausen, "Ultra high-resolution NMR: Sustained induction decays of long-lived coherences," *J. Am. Chem. Soc.*, vol. 133, no. 39, pp. 15644–15649, 2011, doi: 10.1021/ja2052792.

[240] A. Bornet, S. Jannin, and G. Bodenhausen, "Three-field NMR to preserve hyperpolarized proton magnetization as long-lived states in moderate magnetic fields," *Chem. Phys. Lett.*, vol. 512, no. 4–6, pp. 151–154, 2011, doi: 10.1016/j.cplett.2011.07.015.

[241] P. R. Vasos, A. Comment, R. Sarkar, P. Ahuja, S. Jannin, J.-P. Ansermet, J. A. Konter, P. Hautle, B. van den Brandt, and G. Bodenhausen, "Long-lived states to sustain hyperpolarized magnetization," *Proc. Natl. Acad. Sci.*, vol. 106, no. 44, pp. 18469–18473, 2009, doi: 10.1073/pnas.0908123106.

[242] R. Buratto, A. Bornet, J. Milani, D. Mammoli, B. Vuichoud, N. Salvi, M. Singh, A. Laguerre, S. Passemard, S. Gerber-Lemaire, S. Jannin, and G. Bodenhausen, "Drug screening boosted by hyperpolarized long-lived states in NMR," *ChemMedChem*, vol. 9, no. 11, pp. 2509–2515, 2014, doi: 10.1002/cmdc.201402214.

[243] K. Golman, J. H. Ardenkjaer-Larsen, J. S. Petersson, S. Mansson, and I. Leunbach, "Molecular imaging

with endogenous substances," *Proc. Natl. Acad. Sci.*, vol. 100, no. 18, pp. 10435–10439, Sep. 2003, doi: 10.1073/pnas.1733836100.

[244] K. Golman, R. in 't Zandt, and M. Thaning, "Real-time metabolic imaging," *Proc. Natl. Acad. Sci.*, vol. 103, no. 30, pp. 11270–11275, Jul. 2006, doi: 10.1073/pnas.0601319103.

[245] K. Golman, R. I. t. Zandt, M. Lerche, R. Pehrson, and J. H. Ardenkjaer-Larsen, "Metabolic imaging by hyperpolarized 13C magnetic resonance imaging for in vivo tumor diagnosis," *Cancer Res.*, vol. 66, no. 22, pp. 10855–10860, 2006, doi: 10.1158/0008-5472.CAN-06-2564.

[246] S. J. Nelson, J. Kurhanewicz, D. B. Vigneron, P. E. Z. Z. Larson, A. L. Harzstark, M. Ferrone, M. van Criekinge, J. W. Chang, R. Bok, I. Park, G. Reed, L. Carvajal, E. J. Small, P. Munster, V. K. Weinberg, J. H. Ardenkjaer-Larsen, A. P. Chen, R. E. Hurd, L. I. Odegardstuen, F. J. Robb, J. Tropp, and J. A. Murray, "Metabolic imaging of patients with prostate cancer using hyperpolarized [1-13C]pyruvate," *Sci. Transl. Med.*, vol. 5, no. 198, p. 198ra108, 2013, doi: 10.1126/scitranslmed.3006070.

[247] H. Gutte, A. E. Hansen, H. H. Johannesen, A. E. Clemmensen, J. H. Ardenkjær-Larsen, C. H. Nielsen, and A. Kjær, "The use of dynamic nuclear polarization (13)C-pyruvate MRS in cancer.," *Am. J. Nucl. Med. Mol. Imaging*, vol. 5, no. 5, pp. 548–60, 2015, [Online]. Available: http://www.ncbi.nlm.nih.gov/pubmed/26550544%0Ahttp://www.pubmedcentral.nih.gov/articlerender.fcgi?artid=PMC4620180.

[248] F. A. Gallagher, M. I. Kettunen, S. E. Day, D. E. Hu, J. H. Ardenkjær-Larsen, R. In 'T Zandt, P. R. Jensen, M. Karlsson, K. Golman, M. H. Lerche, and K. M. Brindle, "Magnetic resonance imaging of pH in vivo using hyperpolarized 13C-labelled bicarbonate," *Nature*, vol. 453, no. 7197, pp. 940–943, 2008, doi: 10.1038/nature07017.

[249] J. H. Ardenkjaer-Larsen, C. Laustsen, S. Bowen, and R. Rizi, "Hyperpolarized H2O MR angiography," *Magn. Reson. Med.*, vol. 71, no. 1, pp. 50–56, 2014, doi: 10.1002/mrm.25033.

[250] K. W. Lipsø, E. S. S. Hansen, R. S. Tougaard, C. Laustsen, and J. H. Ardenkjær-Larsen, "Dynamic coronary MR angiography in a pig model with hyperpolarized water," *Magn. Reson. Med.*, vol. 80, no. 3, pp. 1165–1169, 2018, doi: 10.1002/mrm.27088.

[251] K. Wigh Lipsø, E. S. S. Hansen, R. S. Tougaard, C. Laustsen, and J. H. Ardenkjær-Larsen, "Renal MR angiography and perfusion in the pig using hyperpolarized water," *Magn. Reson. Med.*, vol. 78, no. 3, pp. 1131–1135, 2017, doi: 10.1002/mrm.26478.